The Propagation of

Ultra High Energy Cosmic Rays

Andrew Martin Taylor

Linacre College

A thesis submitted in candidature for the degree of

Doctor of Philosophy

at the

University of Oxford

Michaelmas Term 2006

Declaration

I declare that no part of this thesis has been accepted, or is currently being submitted, for any degree or diploma or certificate or any other qualification in this University or elsewhere. This thesis is the result of my own work unless otherwise stated.

All the research was carried out in collaboration with my supervisor, Subir Sarkar and colleague Dan Hooper.

The material in Chapter 2 has been published in *The Astroparticle Physics Journal* (D. Hooper, A. Taylor, and S. Sarkar, Astropart. Phys. **23** (2005) 11).

The material in Chapter 3 has been accepted to be published in *The Astroparticle Physics Journal*

The material in Chapter 5 is presently in preparation for submition to a journal.

The Propagation of Ultra High Energy Cosmic Rays

Andrew Martin Taylor
Linacre College

Submitted for the Degree of Doctor of Philosophy
Michaelmas Term 2006

Abstract

This thesis presents theoretical work on the propagation of ultra high energy cosmic rays, from their source to Earth. The different energy loss processes, resulting from cosmic ray interactions with the radiation fields, are addressed. The subsequent uncertainties in the energy loss rates and the effect produced on the arriving cosmic ray spectrum are highlighted.

The question of the composition of ultra high energy cosmic rays remains unresolved, with the range of possibilities leading to quite different results in both the secondary fluxes of particles produced through cosmic ray energy loss interactions en route, and the arriving cosmic ray spectra at Earth. A large range of nuclear species are considered in this work, spanning the range of physically motivated nuclear types ejected from the cosmic ray source.

The treatment of cosmic ray propagation is usually handled through Monte Carlo simulations due to the stochastic nature of some of the particle physics processes relevant. In this work, an analytic treatment for cosmic ray nuclei propagation is developed. The development of this method providing a deeper understanding of the main components relevant to cosmic ray nuclei propagation, and through its application, a clear insight into the constributing particle physics aspects of the Monte Carlo simulation.

A flux of secondary neutrinos, produced as a consequence of cosmic ray energy loss through pion production during propagation, is also expected to be observed at Earth. This spectrum, however, is dependent on several loosely constrained factors such as the radiation field in the infrared region and cosmic ray composition. The range of possible neutrino fluxes obtainable with such uncertainties are discussed in this work.

High energy cosmic ray interactions with the radiation fields present within the source may

also occur, leading to cosmic ray energy loss before the cosmic ray has even managed to escape. The secondary spectra produced are investigated through the consideration of three candidate sources. A relationship between the degree of photo-disintegration in the source region and the neutrino flux produced through $p\ \gamma$ interactions is found.

Acknowledgements

First of all, I would like to thank my supervisors Subir Sarkar and Joe Silk for their enthusiasm, ideas, and guidance over the past three years.

I would also like to express my gratitude to everyone who has helped me in my training and research for this thesis, particularly Daniel Hooper for enlightening me in the art of fortran programming and his willingness to discuss arguments in a mathematical framework. I would further like to thank the Oxford Astrophysics department for its continual supply of varied and interesting speakers.

Resources

This research made use of fortran programming, and the development of several Monte Carlo simulations, due to the nature of the pion production interactions of high energy cosmic rays and the optional cascade routes available to the photodisintegration of high energy cosmic ray nuclei.

I am greatful to PPARC for their support during my visit to Stanford's SLAC summer institute in 2004, and to Oxford Astrophysics for enabling me to attend both a TeV particle astrophysics conference at Fermilab, Chicago, in 2005, and a cosmic ray summer school at Puebla, Mexico, in 2006. This doctorate was funded by a studentship from the Particle Physics and Astronomy Research Council.

Contents

List of Figures

List of Tables

Chapter 1

Introduction

1.1 Cosmic Ray Spectrum and Features

Cosmic rays (CRs) are energetic particles of extraterrestrial origin. In this thesis, to prevent confusion, I will refer to high energy hadrons as CRs and high energy electrons as a high energy electrons.

CRs have been detected on Earth with energies from 10^9 to 10^{20} eV over the last 70 years. Up to 10^{13} eV, their composition has been measured directly using heavy isotope spectrometers (53), and is observed to approximately follow the composition of the local interstellar medium. For a large part of the energy range, the CR spectrum is found to fit a polynomial description of the form,

$$dN/dE \propto E^{-\alpha}, \tag{1.1}$$

with α, the spectral index, taking a value of roughly 2.7. A departure from this fit at low energies ($\sim 10^9$ eV), though, is due to the CRs diffusing towards the Earth from interstellar space through the solar wind. The observed lower energy cutoff in the spectrum is latitude dependent, with this cutoff being found at lower energies for observers at higher latitudes.

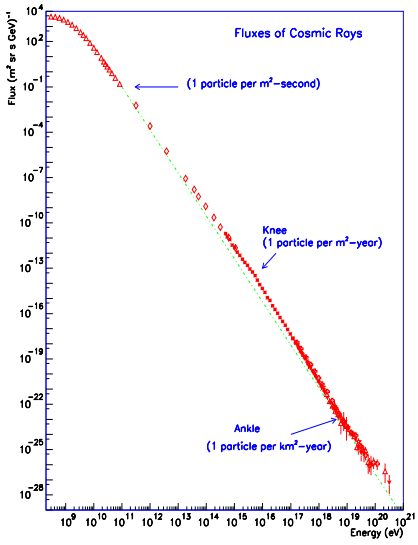

Figure 1.1: The energy spectrum of CRs arriving at Earth, (66)

As pointed out in Fig. 1.1, showing the CR energy spectrum, features in this simple power law spectrum are seen at the high energy end. At around 10^{15} eV, the slope of the spectrum changes significantly from a spectral index of 2.7, to a spectral index of 3.1, this feature, referred to as the "knee", is well observed by the KASCADE experiment (60) in Karlsruhe. Further on up the energy scale, a "second knee" in the spectrum is observed near 10^{17} eV (not shown in Fig. 1.1). These two features in the energy spectrum may be assigned to a maximum rigidity (E/Z) obtainable by supernovae remnants (SNRs), the objects thought to be responsible for CR acceleration up to energies $\sim 10^{17}$ eV.

At energies of around 10^{18} eV, the energy spectum has another sudden change in its spectral index, which returns to a value of 2.7, this feature is referred to as the "ankle". Such an increase in the spectral shape can only really be associated with new sources contributing to the energy spectrum, though others claim (58) that such a feature is caused by pair production of UHECR protons, for which they must assume that protons are a largely dominant (>85% (59)) component of UHECRs.

An argument for a changeover in the CR sources from Galactic to Extragalactic in the energy range $\sim 10^{18}$ eV, is found through a consideration of the Larmor radius of CRs in the Galaxy. This describes the orbit a CR particle would follow in a uniform magnetic field,

(neglecting diffusion effects of the CRs in the Galactic magnetic field) and is given by,

$$R_{\text{Larmor}} \approx \left(\frac{1}{Zec}\right)\left(\frac{E_{\text{CR}}}{\text{EeV}}\right)\left(\frac{\mu\text{G}}{B}\right)\text{kpc}, \tag{1.2}$$

where eZ is the charge of the particle, R_{Larmor} is the Larmor radius, E_{CR} is the CR energy, and B is the Galactic magnetic field. From equation (1.2) it is clear that CRs with energies $>10^{18}$ eV cannot be contained within the Galactic magnetic field.

The shape of the energy spectrum becomes less clear at energies above 10^{18} (4; 95), at which the flux drops below 1 particle km^{-2} yr^{-1}, and at which energy the sources of CRs are thought to change over from Galactic to Extragalactic in origin. The energy range of such a change over of CR origin is vitally important for the calculation of the total power output of CR sources. A lower value change-over requiring a larger power output of such sources, placing constraints on possible astrophysical objects that could act as CR sources.

1.2 Cosmic Ray Composition

The CR composition may be measured directly only in the low energy region ($<10^{13}$ eV), where the flux is sufficiently large to allow satellite and balloon spectroscopy is possible. At higher energies only indirect composition measurements are possible through an analysis of the shower profile and content, created when a CR causes a particle shower in the atmosphere. These are measured by both fluorescence detectors and ground array detectors, such as those used by the Auger experiment (96). Examples of particular shower information used to infer the CR composition are the elongation rate, and the electron and muon content of the shower.

The total number of both electrons, which predominantly are produced in the electromagnetic shower, and muons produced in the hadronic shower, is dependent on both the energy and composition of the particle that initiated the shower. For high energy CRs, an Iron nucleus of a given energy results in more muons and fewer electrons at ground than a proton of the same energy. Specifically, for the energy range considered by KASCADE ($10^{14.5}$ - 10^{17} eV), an Iron primary yields about 30% more muons and 50% fewer electrons than a proton of the same energy. This change in the number of electrons and muons in the shower may be understood by considering a simple Heitler model for air showers like that shown below in Fig. 1.2.

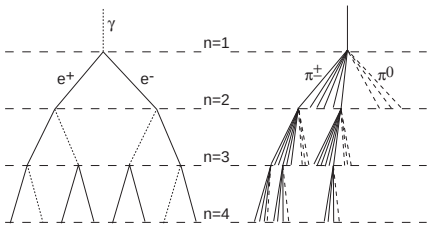

Figure 1.2: Simple Heitler model describing the development of the electronmagnetic and hadronic shower, (81)

For the electromagnetic cascade, the radiation length $X_0^{\rm air}$=36.66 g cm^{-2}, and the shower stops developing when the particles in the shower have an energy $E_{\rm crit}^{e\_{\rm air}}$=85 MeV, below which the particles in the shower have insufficient center of mass energy to produce further particles in the electromagnetic shower through pair production or bremsstrahlung. For the hadronic cascade, the interaction length for strongly interacting particles is λ_0=120 g cm^{-2}, and the shower stops developing when particles in the shower have an energy $E_{\rm crit}^{\pi\_{\rm air}}$=20 GeV, below which pion production ceases. Within the Heitler model, the hadronic shower develops as shown in Fig. 1.2, with the π^0 particles going on to decay to a pair of γs, which feed into an electromagnetic shower development. This occurs until the particles in the shower have an energy below $E_{\rm crit}$, at which point shower development ceases.

The increase in the muon number for an Iron nucleus primary, compared to a proton primary of the same energy, may be understood by the fact that the number of muons in the shower has an energy dependence of the form (67),

$$N_\mu(E) \propto E^\beta, \tag{1.3}$$

where β <1, as can be obtained through a consideration of the Heitler model for the hadronic cascade, (81) ($\beta \approx 0.9$). Employing the superposition model of the Iron nucleus here, the ratio of the number of muons in a shower generated by a nucleus of atomic mass A to the number of muons generated by a proton of the same energy is,

$$A\left(\frac{1}{A}\right)^\beta = A^{1-\beta}, \tag{1.4}$$

which predicts an increase of about ($A^{1-\beta}$-1)×100% more muons for an Iron nucleus shower to that of a proton shower of the same energy.

The number of electrons in a cascade has one added degree of complexity, since the maximum number of electrons in the shower is not the number observed at ground. This is because at the energies concerned the observer sits well below the peak of the distribution in the number of electrons, the position of the observer and the shape of the exponential dropoff must be considered. From the Gaisser-Hillas function (94),

$$N_e(X) = N_{e_{\max}} \left(\frac{X - X_1}{X_{\max} - X_1} \right)^{\frac{X_{\max} - X_1}{\lambda}} \exp\left(-\frac{X - X_{\max}}{\lambda} \right), \tag{1.5}$$

where X_1 is the depth of the first interaction, and λ is the decay constant of the exponential dropoff, with a typical value of ∼70 g cm^{-2}, (the position of the observer is described by X, where X reflects the total amount of matter between the top of the atmosphere and the observer).

The number of electrons in the shower is of the form,

$$N_e(E) \propto E^{\beta}, \tag{1.6}$$

where $\beta > 1$, as can be obtained from a consideration of the Heitler models for the hadronic and electromagnetic cascades, (81) ($\beta \approx 1.05$).

Following a similar argument to that for muons, the number of electrons in the shower decreases by about (1-$A^{1-\beta}$)×100% fewer electrons, for an Iron nucleus shower compared to a proton generated shower of the same energy.

For a given species of particle the elongation rate of the shower is the distance from the upper atmosphere (where CR showers are initiated) to where the particle number in the shower is maximum. This distance increases logarithmically with the energy of CR arriving at the atmosphere. The elongation rate is expected to be longer for a proton than a heavier nucleus of the same energy. This can be understood in terms of the superpostion model, in which a nucleus of mass number A can be considered as A separate nucleons each with a fraction $1/A$ the energy of the nucleus. From this model it is clear that the elongation rate, which only

increases with the logarithm of the energy, will be longer for a proton than an Iron nucleus of the same energy.

Composition measurements made in the ultra low energy CR region ($\sim 10^{10}$ eV) through spectroscopy methods reveal that the CR abundances are similar to those of the interstellar medium. One problem of such measurements is the effect of solar modulation on CRs arriving in the solar system, which is composition (A/Z) dependent. Solar modulation is thought to have an effect on the arriving composition up to energies of $\sim 10^{10}$ eV/nucleon. The fractions of the different major species arriving at Earth, during solar minimum, are given in table 1.1 below,

Table 1.1: The major CR element abundances arriving at Earth with 10^8 eV/nucleon and 5×10^{10} eV/nucleon (during solar minimum)- normalised to the abundance of H [1]

Element	Fraction (10^8 eV/nucleon)	Fraction (5×10^{10} eV/nucleon)
H	1.0	1.0
He	0.21	0.05
O	0.004	0.001
Fe	0.0003	0.0001

At slightly higher energies (10^{12} - 10^{13} eV/nucleon), the experiments RUNJOB and JACEE balloon experiments have measured the CR composition directly through spectroscopic techniques. The values from such measurements are shown below in table 1.2.

Table 1.2: The major CR element abundances arriving at Earth with 10^{13} eV/nucleon- normalised to the abundance of H [2]

Element	Fraction (10^{13} eV/nucleon)
H	1.0
He	0.05
O	0.005
Fe	0.0004

As mentioned in the previous section, at an energy of $\sim 10^{15}$ eV, the "knee" feature in the CR spectrum is observed. A possible interpretation of the "knee" is that it is due to a limiting maximum energy of low energy ($<10^{17}$ eV) CR sources. This interpretation is backed up by recent analysis made by the KASCADE group, (65). Through measurements of the numbers of electrons and muons in CR showers, dictated by the energy of the arriving CR and it's composition, some discernment is possible between the major species groups (H, He, C, Si, and Fe) in the CR spectrum, for the energy range $10^{14.5}$ - 10^{17} eV. The results obtained from this analysis, though, are dependent on the high energy hadronic model employed in the analysis as seen in Fig. 1.3 below. However, both analysis do indicate that successively heavier CR components dominate the spectrum in the transition region between the "knee" and the "second knee".

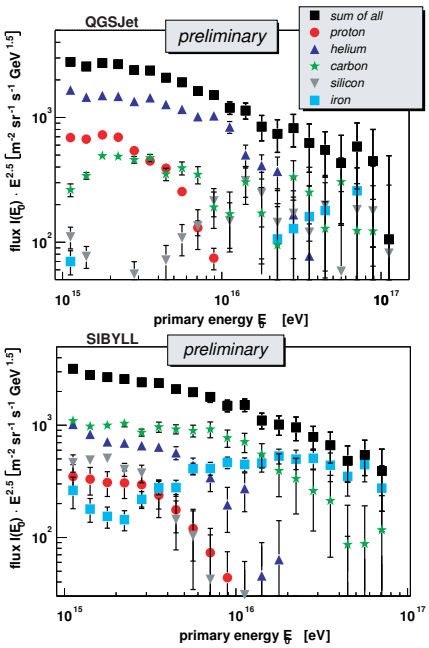

Figure 1.3: The change in the CR composition at the "knee" measured by KASCADE (65).

As seen in Fig. 1.3 above, observational evidence motivating a change of the dominant composition in this region is provided. At least one subfeature is seen between between the "knee" and the "second knee" in the data, possibly associated with a change to a dominance of Oxygen nuclei from Helium nuclei in the spectrum, occurring $\sim 12 \times 10^{15}$ eV. Such an explanation

leading to the expectation of another feature in the spectrum at $\sim 40 \times 10^{15}$ eV due to a change from a dominance of Oxygen to a dominance of Iron in the spectrum. However, as can also be seen in Fig. 1.3, the interpretation of subfeatures seen between the "knee" and the "second knee" in the KASCADE data is dependent on the hadronic interaction model used during the analysis, with the employment of both hadronic interaction models showing the changeover in composition from Helium to Carbon to Iron nuclei, though these transitions for the two models occur at different energies.

For higher energy CRs, the determination of the composition becomes more and more dependent on the hadronic model employed in the analysis, with results differing from experiment to experiment. The Fly's Eye, HiRes (HiRes referring to the high resolution Fly's Eye observatory), Yakutsk, and Auger experiments all have different CR energy range coverages, also making their comparison difficult.

The elongation rate data, $X_{\max}$, from the Fly's Eye experiment (71) suggests a gradual transition in the composition, from being dominated by heavy nuclei below $10^{18.5}$ eV (the position of the "ankle" feature), becoming lighter in compostion above this energy. Such an interpretation suggesting the "ankle" is associated with the change in composition of CRs, returning to a lighter spectrum above the "ankle". This analysis was carried out with a "QCD pomeron" hadronic model.

A similar interpretation is found from the analysis of the elongation rates of showers in the HiRes data (68), which suggests a qualitative trend of a transition from an Iron dominated component below the "ankle", to a proton dominated component above the "ankle", but with the transition occurring at $10^{17.6}$ eV. This analysis was carried out with the QGSJET hadronic model. An analysis of the $X_{\max}$ distribution in the HiRes data, using a two component (light and heavy) fit, leads to a proton component of between 60% (SIBYLL) and 80% (QGSJET) for the energy range 10^{18} - $10^{19.4}$ eV (70).Analysis of the Yakutsk data with the QGSJET hadronic model also reveals a lightening of the mass composition above $10^{18.5}$ eV (72).

Despite the general consensus between the fluorescence based measurements of the elongation rate of CRs, and from these (with the use of a hadronic interaction model) the inference of the composition, a large degree of uncertainty in these results exists due to the reliability of

the hadronic model applied.

A result of the dependency of the elongation rate, $X_{\max}$, on the initial interaction point, and the interaction lengths, is that its predicted value from simulations is model dependent. Several hadronic models currently exist, all of which are consistent with observations at the lower center of mass energies available to collider experiments, which predict different high energy running of the nucleon-air interaction cross section and elasticity value. Two of the main models presently employed to describe these interactions are SIBYLL and QGSJET, whose differing features, in broad terms, may be attributed to the different cross sections and elasticity values used in the high energy hadronic interaction simulations. Both models, as required, satisfy the data from hadronic interaction experiments at collider center of mass energies. However, it is in the extrapolation of these models to higher energies where differences start to emerge.

A comparison of the data sets mentioned, in the energy range $10^{18.5}$ - 10^{20} eV, is shown below in Fig. 1.4. Also seen in this plot is the variation between the predicted elongation lengths from DPMJET, SIBYLL, and QGSJET_11 hadronic interaction models.

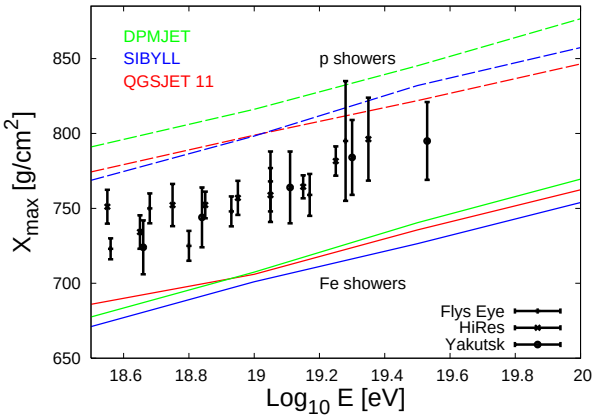

Figure 1.4: Average elongation lengths measured by Fly's Eye, HiRes, Yakutsk, and Auger

Analysis of the muon density in showers, however, shows little agreement with the idea of the CR spectrum becoming lighter above the ankle (73). This is particularly worrying since recent improvements of the QGSJET hadronic model (74) (the latest version being referred to as QGSJET_11), which includes non-linear effects, lead to a reduction of the number of muons in the shower, whilst making $X_{\max}$ predictions slightly larger, thus weakening the argument

for the dominant light composition at high energies observed in elongation rate measurements.

1.3 High Energy Cosmic Ray Sources and Propagation Effects

At the lower energies, below the "knee" ($\sim 10^{15}$ eV), the first order Fermi shock acceleration mechanism (see Appendix), taking place in SNRs, is thought to be a likely source of CRs up to $\sim Z \times 10^{15}$ eV, where Z is the charge of the nuclei being accelerated, at which a maximum energy limit is placed, through arguments on the maximum acceleration rate and the lifetime of the shock accelerating the particles (54).

Through observations of local supernovae remnants (SNRs) (ie. CasA, SN1006, RX J1713.7-3946,...), in radio, X-ray, and γ-ray (where possible), both the features of synchrotron emission and inverse compton scattering of photons are observed, indicating the presence of a Fermi shocked electron population in the region. Although clearly motivated by the observation of high energy electrons present in SNRs, signatures of high energy protons and ions present in SNRs are less clear. The main expected feature is the observation of photons created from π^0 decays, formed in the hadron-hadron collisions ($p + p \rightarrow p + p + \pi^0$) of high energy CRs with interstellar gas. The observation of γ-rays created through hadronic collisions remains unclear, with tentative evidence coming from observations of RX J1713.7-3946 with the HESS Cerenkov telescope (76).

The idea of SNRs accelerating CRs is to some extent supported by the observations mentioned in the previous section. The material expected to be present in the surrounding environment of the SNR, appears consistent with that observed in arriving CR composition data (77) (see previous section for CR composition data).

At higher energies, sources of CRs remain unknown, with possible candidates drawn up from the Hillas criteria (55). Acceleration mechanism aside, a simple dimensional argument of possible acceleration sites giving the maximum obtainable energy from the magnetic field and size of the site yields,

$$E^{\max} \sim 10^{18} Z \left(\frac{R}{\mathrm{kpc}}\right) \left(\frac{B}{\mu\mathrm{G}}\right) \mathrm{eV}, \tag{1.7}$$

where R is the radius of the accelerating region measured, B is the magnetic field in the

accelerating region, and Z is the charge of the particle being accelerated. From a slightly more complete consideration in which both the escape time of the particles being accelerated and their acceleration rate, under the assumption of Bohm diffusion, the previous result of equation (1.7) is modified to,

$$E^{\max} \sim 10^{18} Z\beta \left(\frac{R}{\mathrm{kpc}}\right)\left(\frac{B}{\mu\mathrm{G}}\right)\mathrm{eV}, \tag{1.8}$$

where β is the shock speed in units of c.

From this criteria, possible accelerators, able to achieve the particle energies observed at the high end of the spectrum $\sim 10^{20}$ eV, are: active Galactic nuclei (AGN) ($R_{kpc} \sim 10^{-5}$,$B_{\mu G} \sim 10^{7}$;gamma-ray bursts (GRBs) ($R_{kpc} \sim 10^{-7}$,$B_{\mu G} \sim 10^{9}$); and starburst regions ($R_{kpc} \sim 0.01$,$B_{\mu G} \sim 100$).

With the consideration of such objects as the source of UHECRs, assumptions as to the distribution of the CR sources, based on the distribution of such objects, may be made. Since these objects are expected to be distributed within structured regions in the Universe, they would be expected, naively, to have a homogenous distribution through space up to the epoch where structure formation turned on. Following the distribution of CR sources used by previous authors in the field (16), which describe the distribution of quasi-stellar objects (24) and star forming regions (23), and possibly that of AGN and GRBs (103), the distribution of CR sources used here will be,

$$\begin{aligned}
\frac{dN}{dV} &\propto (1+z)^3 \text{ for } z < 1.9 \\
&\propto (1+2.7)^3 \text{ for } 1.9 < z < 2.7 \\
&\propto (1+2.7)^3 \exp\left(-\frac{2.7-z}{2.7}\right) \text{ for } z > 2.7.
\end{aligned} \tag{1.9}$$

It should be noted here that, for the purpose of CR propagation simulations, for energies above 10^{19} eV, only sources up to a redshift of 0.5 contribute to the CR flux at Earth, this limit being set by pair production energy loss of CRs during propagation. However, for the calculation of the cosmogenic neutrino flux at Earth, produced through CR interactions during propagation, sources up to a redshift of $\sim$8 must be considered, due to neutrino energy loss, through interactions during propagation, being negligible.

The main theory for CR acceleration is the Fermi shock acceleration model (see Appendix), which produces an energy spectrum $\sim E^{-2}$, in rough agreement with the spectra of particles thought to have been Fermi accelerated. Evidence for the existence of regions in which the Fermi process is observed to occur have been found through satellite measurements of the energy distribution of ions in the bow shock of the Earth's magnetosphere, (56) and (57), and from γ-ray observations of SNRs within our Galaxy (89), whose spectral index reflects the accelerated electron population, and possibly proton population, present.

Radio and X-ray spectra observed from SNR observations show, indirectly, that such regions are responsible for the acceleration of electrons, giving them an energy spectrum of the form $E^{-2.1}$. Such signals come from synchrotron emission of the electrons, orbiting about the magnetic field lines present in the object. The high energy electrons present in SNR also contribute to the γ-ray signal from the objects, since CMB and starlight photons present in the region will upscatter off high energy electrons through the inverse-Compton effect, producing a γ-ray spectrum.

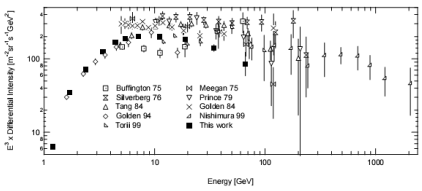

Figure 1.5: Measurements of the high energy electron spectrum by the HEAT satellite in the energy range 10^9 - 10^{11} eV (63)

The situation is similar for electrons. The high energy electron spectrum observed at Earth, shown above in Fig. 1.5, has been measured in the energy range 10^9-10^{11} eV (62; 63), is observed to have approximately an energy spectrum of the form $E^{-3.1}$. The difference in spectral index between the spectrum observed at source, and that at Earth, is due to the dominant energy loss mechanisms for electrons propagating through space: the inverse Compton scattering process and synchrotron energy loss. In these processes the electrons lose energy through either scattering from background photons and transferring their energy to them, or interacting with the Galactic magnetic field and losing their energy by synchrotron radiating it away. For high

energy electrons, the cooling time is shorter than the confinement time due to diffusion in Galactic magnetic fields, for which a simple relationship between the source spectral index and the observed spectral index is found.

The energy loss rate through inverse Compton or synchrotron energy loss, for an electron of energy E_e, goes as,

$$\begin{aligned} \frac{dE_e}{dt} &= \frac{4\sigma_T c}{3}\Gamma^2 U_\gamma \text{ (or } U_B) \\ &= \frac{4\sigma_T c}{3}\left(\frac{E_e}{m_e c^2}\right)^2 E_\gamma^2 n(E) \text{ (or } \frac{\mathrm{B}^2}{8\pi}), \end{aligned} \tag{1.10}$$

where σ_T is the Thompson cross-section, Γ is the Lorentz factor of the electron, and U_γ (or U_B) is the energy density of the radiation field (or magnetic field).

So, the energy loss time, $\tau = \left(\frac{1}{E}\frac{dE}{dt}\right)^{-1}$, goes as

$$\begin{aligned} \tau_e &= \frac{3(m_e c^2)^2}{4\sigma_T c E_e U_\gamma} \\ &\approx 3\times 10^5 \left(\frac{10^{12}\mathrm{eV}}{E_e}\right)\left(\frac{\mathrm{eV\ cm^{-3}}}{U_\gamma}\right)\mathrm{yrs}. \end{aligned} \tag{1.11}$$

For sufficiently high energies, a spectrum of the form $E^{-(\alpha+1)}$ is therefore observed, for a source spectrum of the form $\mathrm{E}^{-\alpha}$. This result reveals that observations of high energy electrons with an energy spectrum of the form $\mathrm{E}^{-3.1}$ at Earth, are consistent with observations of electrons at source having an energy specrum of the form $\mathrm{E}^{-2.1}$.

Due to such fast cooling times, and diffusion limited propagation, high energy (10^{11} eV) electrons are only able to propagate on distances up to kpc scales (their cooling times being $\sim 10^6$ years), limiting their possible sources to within Galactic distances.

As pointed out earlier in this Chapter, CRs are not constrained to propagate within the Galaxy above energies $\sim 10^{18}$ eV. For energies $<10^{18.4}$ eV, CRs predominantly lose energy due to cosmic expansion, above this energy pair production and pion production processes lead to a dramatic increase in the energy loss rates, as shown in Fig. 4.1. The propagation of CRs with energies below energies $\sim 10^{18.4}$ eV is therefore only really affected by the diffusive effects of magnetic fields en route.

Once created at source, the CRs must propagate through Galactic space (low energy CRs)

and Intergalactic space (high energy CRs) before their arrival at Earth. Even weak intergalactic magnetic fields (nG) may have a large effect on an UHECR's propagation, forcing it into a diffusive regime. At energies above above this diffusive regime, the CR's path may be deflected sufficiently, due to the presence of such fields, such that the arrival direction of the CR, when detected at Earth, does not correlate with the source's direction.

At energies below the "knee" (ie. $<10^{15}$ eV) the CR spectrum detected at earth has an energy spectrum of the form $E^{-2.7}$. The steepening of the spectrum after leaving the source, where it is thought to have the form $E^{-2.1}$, is explained by the CRs having to diffuse through the large magnetic fields (μG) present within the Galaxy, with such trapping said to have the energy dependence $E^{-0.6}$. This magnetic trapping energy dependence, for low energy ($<10^{11}$ eV) CRs, would possibly arise from CR excitation of Alven waves in the magnetic field, forcing the CRs to travel at the Alven velocity of such waves, $V_A=(U_B/\rho)^{\frac{1}{2}}$, where U_B is the energy density of the magnetic field and ρ is the density of the particles in the plasma (61). Magnetic trapping might also arise due to CRs scattering off of irregularities present in the magnetic field, though the energy dependence of such trapping is dependent on the power spectrum of such irregularities. This energy dependence, however, cannot continue to high energies (10^{19} eV), since the turning off of the diffusive process would lead to anisotropy in the arrival directions of the CRs, in contradiction with the observations. At higher energies it is possible that CR scattering off of magnetic fields, with a Kolmogorov irregularity spectrum,would lead to a less steep energy dependence of the form $E^{-0.3}$, resolving the problem of the isotropy in the spectrum at higher energies.

After the "second knee", the penultimate feature observed in the CR spectrum appears, the "ankle", at which the spectrum is observed to return to a spectrum of the form $E^{-2.7}$, the increase in the spectrum being associated with a dominance of extragalactic sources contributing to the spectrum. In this work, the propagation of these CRs, above the "ankle", are considered. Throughout it will be assumed that such CRs originate from a homogenous distribution of extragalactic sources.

1.4 The structure of this thesis

This thesis presents a study into the nature of ultra high energy cosmic rays (UHECRs).

In Chapter 2 the effect of the CR composition, intergalactic radiation fields, and photon nuclei interaction cross-sections, on the arriving CR spectra are studied.

In Chapter 3 an analytic treatment for the propagation of UHECR nuclei is developed, and employed to interpret some of the results of Chapter 2.

In Chapter 4 the secondary cosmogenic neutrino spectrum, produced through UHECR energy loss interactions during propagation from their source to Earth, and its dependence on the CR composition, is investigated.

In Chapter 5 CR energy loss within the CR source is considered for three example source regions, with neutrino fluxes from such sources being calculated.

My conclusions are presented in Chapter 6.

Appendix A gives a brief review of the basic ideas behind the Fermi shock acceleration mechanism.

Appendix B outlines the structure of the Monte Carlo calculation.

Chapter 2

Ultra High Energy Cosmic Ray Nuclei Propagation

As CR nuclei propagate through the dominant CMB and CIB radiation fields, they are expected to undergo photo-disintegration, to some degree. The amount of photo-disintegration undergone by such nuclei depending upon the amount of time they spend in the radiation fields (dictated by the spatial distribution of the UHECR sources and the strengths of the intergalactic magnetic fields), the cross-sections for photo-disintegration interactions, the strengths of the radiation fields that they propagate through, and the composition of the CRs leaving the accelerating region (source).

As mentioned in the introductory chapter, in this and subsequent chapters the distribution of the sources in space will be,

$$\begin{aligned} \frac{dN}{dV} &\propto (1+z)^3 \text{ for } z < 1.9 \\ &\propto (1+1.9)^3 \text{ for } 1.9 < z < 2.7 \\ &\propto (1+1.9)^3 \exp\left(\frac{(2.7-z)}{2.7}\right) \text{ for } z > 2.7. \end{aligned} \tag{2.1}$$

In previous work by other groups, good fits to the CR data have been found for different source distributions, along with a determination of the subsequent neutrino flux produced (41). An investigation into the effects of the source distribution shall not be considered here, only noting that such groups find equally good agreement with the UHECR data for the strong evolution of sources and energy spectrum used here, as well as with a much weaker evolution of sources

and a steeper injection spectrum (92).

For comparative calculations in this chapter, the energy spectrum used will be,

$$\frac{dN_p}{dE_p} \propto E_p^{-\alpha} \text{ for } E < (E_{\max} \times Z/Z_{\max}), \tag{2.2}$$

where α is a constant and $Z_{\max}$ is largest atomic number (proton number) considered.

2.1 Photo-Disintegration Cross-Sections

In previous studies, (27; 28; 10), the photo-disintegration cross-sections have been parameterised with the following forms,

$$\sigma_{A,i}(\epsilon) = \begin{cases} \xi_i \Sigma_{\rm d} W_i^{-1} e^{-2(\epsilon-\epsilon_{p,i})^2/\Delta_i^2} \Theta_+(\epsilon_{\rm thr}) \Theta_-(\epsilon_1), & \epsilon_{\rm thr} \le \epsilon \le \epsilon_1, \quad i = 1,2 \\ \zeta \Sigma_{\rm d} \Theta_+(\epsilon_{\max}) \Theta_-(\epsilon_1)/(\epsilon_{\max} - \epsilon_1), & \epsilon_1 < \epsilon \le \epsilon_{\max} \\ 0, & \epsilon > \epsilon_{\max} \end{cases} \tag{2.3}$$

where ξ_i, ζ, $\epsilon_{p,i}$ and Δ_i are parameters with values which were fit to limited nuclear physics data. Here, i is the total number of nucleons broken off of the nucleus in the interaction. $\Sigma_{\rm d}$ is given by

$$\Sigma_{\rm d} \equiv \int_0^\infty \sigma(\epsilon)\, d\epsilon = \frac{2\pi^2 e^2 \hbar}{m_p c} \frac{(A-Z)Z}{A} = 60 \frac{(A-Z)Z}{A} \text{mb-MeV}, \tag{2.4}$$

and the function W_i is given by

$$W_i = \Delta_i \sqrt{\frac{\pi}{8}} \left[\text{erf}\left(\frac{\epsilon_{\max} - \epsilon_{p,i}}{\Delta_i/\sqrt{2}} \right) + \text{erf}\left(\frac{\epsilon_{p,i} - \epsilon_1}{\Delta_i/\sqrt{2}} \right) \right]. \tag{2.5}$$

$\Theta_+(x)$ and $\Theta_-(x)$ are the Heaviside step functions. $\epsilon_1 = 30$ MeV, $\epsilon_{\max} = 150$ MeV, separating out the giant dipole resonance that dominates the cross-section below 30 MeV, leading to the loss of one of two nucleons, and multi-nucleon loss which dominates in the energy range 30-150 MeV.

$\epsilon_{\rm thr}$, the threshold energy for a given process, which varies with i, has values tabulated in Ref. (27). For most cases, $\epsilon_{\rm thr} \approx i \times 10$ MeV.

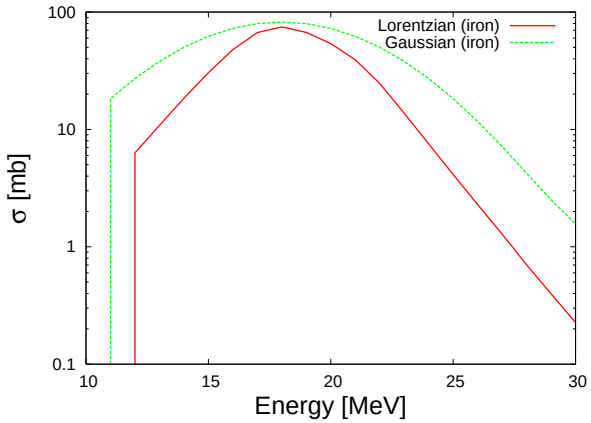

Figure 2.1: A comparison of the Gaussian and Lorenzian description of the gian-dipole resonance cross-section for the case of single nucleon emission from an iron nuclei

.

This parameterisation of the photo-disintegration cross-sections involves approximating the cross-sections with a Gaussian part to represent the giant dipole resonance and a constant part for the multi-nucleon loss processes. A further approximation of the model is that only a single mass number, A, is considered for each atomic number, Z, leaving the possibility that alternative important isotope channels are neglected.

So far in this discussion, a Gaussian type fit to the giant dipole resonance has been used. However, more recent developments in this area have shown that a more accurate description of the giant dipole resonance may be obtained with Lorentzian type fits instead (9), of the form,

$$\sigma_{A,Z,i_p,i_n}(\epsilon_\gamma) = \frac{\Gamma_{A,Z,i_p,i_n}(\epsilon_\gamma)\,\epsilon_\gamma^4}{(\epsilon_\gamma^2 - E^2_{A,Z,i_p,i_n})^2 + \Gamma^2_{A,Z,i_p,i_n}(\epsilon_\gamma)\,\epsilon_\gamma^2}, \tag{2.6}$$

where E_{A,Z,i_p,i_n} is the position of the giant dipole resonance and Γ_{A,Z,i_p,i_n} is the width of that resonance given by

$$\Gamma_{A,Z,i_p,i_n}(\epsilon_\gamma) = \Gamma_{A,Z,i_p,i_n}(E_{A,Z,i_p,i_n})\,\frac{\epsilon_\gamma^2}{E^2_{A,Z,i_p,i_n}}. \tag{2.7}$$

In particular, the Gaussian parameterizations were often found to overestimate the width of the giant dipole resonance, as is demonstrated in Fig. 2.1 above.

In this study, the Lorentzian parameterisation of the giant dipole resonance contribution to the cross-section will be used in conjunction with the a flat description of the multi-nucleon

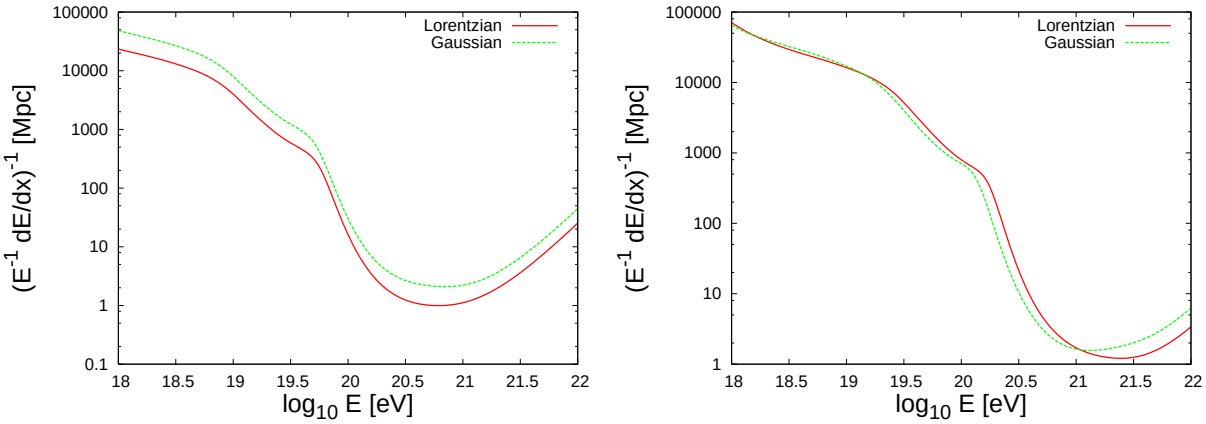

Figure 2.2: Energy loss lengths due to photo-disintegration for Oxygen (left) and Iron (right) nuclei for Gaussian (PSB) and Lorentzian cross section parameterizations. The CIB model of Malkan and Stecker has been used.

part of the cross-section. However, whereas a cross-over energy of 30 MeV was used for the Gaussian parameterisation, a higher, 50 MeV, cross-over energy will be used for the Lorentzian parameterisation.

Along with this change in the description of the cross-section, a web of alternative disintegration routes through (A,Z) isotope space will be implemented to prevent important alternative disintegration paths being neglected. Such data for the Lorenztian cross-sections for multi-isotope elements, with A >11, are found at (42).

To investigate the changes introduced by these two improvements in the description of the photo-disintegration cross sections, the energy loss lengths for Iron and Oxygen are compared above in Fig. 2.2 (obtained through the application of these cross sections to equation (4.5)),

As observed from the plots in Fig. 2.2, the energy loss lengths for Oxygen and Iron are changed very little with these improvements implemented. The effect of the change in the cross-section parameterisation on the arriving CR spectrum is shown explicitly in Fig. 2.3. For Iron nuclei injected at source, only a small difference in the CR spectrum, at the highest energies, is expected between the two parameterisations, with the "Gaussian" parameterisation leading to a harder cutoff due to the onset of photo-disintegration.

For further work in this chapter, the Lorentzian model cross-sections will be employed for nuclei with A between 11 and 56, with A <11 cross-sections being described by the Gaussian model cross-sections (due to the lack of data for the Lorentzian description of cross-sections for A <11).

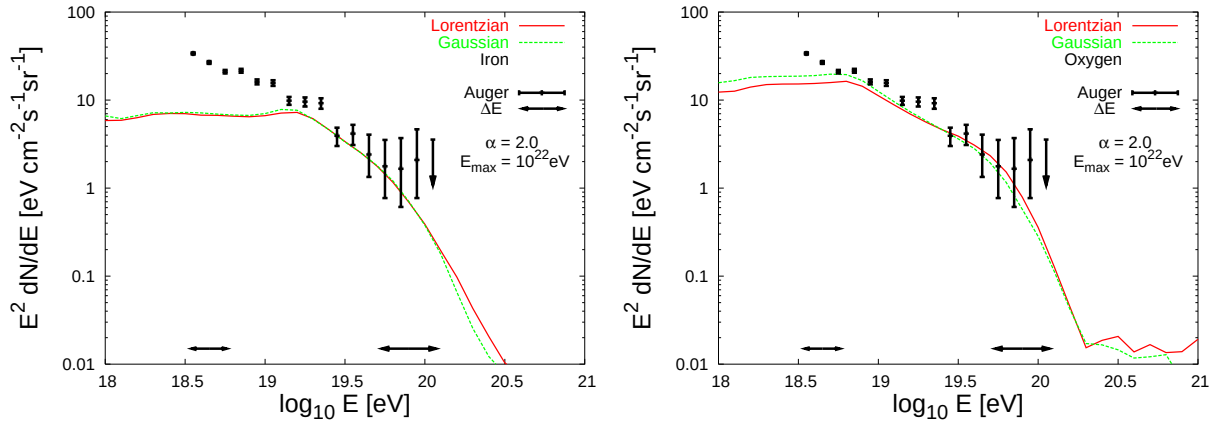

Figure 2.3: A comparison between the arrival spectrum of cosmic rays for Oxygen and Iron nuclei at source, obtained with a use of the Lorentzian type giant dipole resonance cross-sections (9), with that obtained using Gaussian parameterisation of (10)

2.2 Dominant Radiation Field Backgrounds

Since the two primary factors dictating the interaction rate of UHECRs with the radiation field are the target number density of the photons and the center of mass energy in the CR-γ system, the dominant radiation field relevant to CR nuclei propagation is apriori not obvious. From Fig. 2.4 showing the energy density in the CIB and CMB against energy of the photons, the number density of CIB photons is clearly much smaller than that in the CMB. However, due to the higher energy of the CIB photons compared to that of the CMB (a factor between 10-1000 higher), the threshold energy may be obtained by lower energy CRs interacting with the CIB than for CRs interacting with the CMB (the expression for the threshold energy for this process is given in equation (5.14)), thus compensating somewhat for the reduced target number. For the case of heavy nuclei photo-disintegration, the competition between the two radiation fields is most pronounced due to the reduced Lorentz factor of the CR heavy nucleo compared to that of lighter nuclei or protons of the same energy.

The assembly of matter into stars and galaxies and the subsequent evolution of such systems is accompanied by the release of energy from both the nuclear fusion inside stars and the release of energy by accreting objects. Cosmic expansion and the absorption of short wavelength radiation by dust and re-emission at longer wavelengths shifts a significant part of this radiant energy into infra-red background radiation, $\lambda \sim$ 1-1000 μm. A background of infra-red radiation is therefore an expected relic of structure formation processes (35).

The CIB radiation is expected to be extragalactic in origin and consequently isotropic on

large scales. The spectrum of this background depending on the luminosity and evolution of the sources, and distribution of dust from which it is scattered.

A degree of uncertainty in the background radiation field exists, a large cause of which is due to the difficulties in the removal of local contamination of zodiacal dust from the CIB detected. There is presently a great deal of CIB upper limits, lower limits and tentative detection. The most convincing evidence for the background coming from around 3.5μm and 100μm (where a window in local foregrounds is available).

This uncertainty present in the infra-red region (10^{-2}-1 eV), leads to uncertainty in the photo-disintegration rates of nuclei, since infra-red photons, to the Lorentz boosted CRs (with a Lorentz factor $\sim 10^8$-10^9), have an energy comparable to that of the giant dipole resonance at $\sim$10 MeV.

Direct measurement of the CIB has been performed by two satellites: the COsmic Background Explorer (COBE) and the InfraRed Telescope in Space (IRTS). DIRBE, an instrument aboard the COBE satellite (36), has provided measurements in the 1.25 to 240 μm range. FIRAS, another instrument aboard COBE, covered the range from 125μm to mm wavelengths. Also, the ISO satellite carried two instruments which were employed in the indirect measurement of the CIB, ISOCAM at 7 and 15 μm and ISOPHOT at 170 μm (37).

In addition to these measurements, instruments on telescopes such as the Hubble Space Telescope's (HST) wide field planetary camera, combined with spectrophotometry from the duPont telescope and the HST Faint Object Spectrograph, were used to measure the CIB at 0.3, 0.55 and 0.8 μm. Galaxy counts made using the HST Northern and Southern Deep Fields, between 0.36 and 2.2 μm, supplemented with shallower ground based observations, have also been used to obtain lower limits on the CIB (38; 39; 40). The results obtained, from each of the measurements by DIRBE, ISO, HST, and IRTS are displayed in Fig. 2.4.

The three models of the CIB employed here, are those of Malkan and Stecker (29; 30), Aharonian *et al.* (31; 32; 33), and Franceschini *et al.* (34), which collectively span the variation in CIB measurements, as shown below in Fig. 2.4.

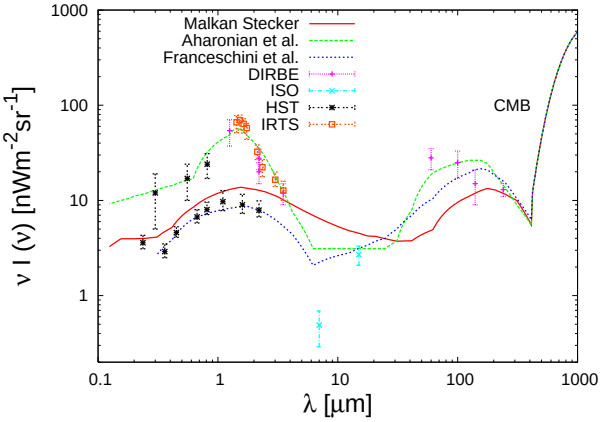

Figure 2.4: The dominant CMB and CIB radiation fields, showing the models of Malkan and Stecker, Aharonian and Franceschini

A measurement of the CIB intensity, however, does not provide any information on the history of the energy releases in the universe which lead to it, ie. the relative contribution of AGN and star-forming galaxies, and the history of star and element formation. In a dust free universe, the spectral luminosity density can in principle be simply derived from a knowledge of the spectrum of the emitting sources and the cosmic history of their energy release. In a dusty universe, the total intensity remains unchanged, but the energy released is redistributed over the spectrum.

For the calculations in this chapter, no evolution of the CIB with redshift is considered, apart from the increase in the energy of the CIB photons with increased redshift to take into account the effects of cosmic expansion. However, since the maximum redshift relevant for CR propagation is z=0.5, this effect is small.

The variation introduced in the photo-disintegration lengths by the range of CIB models considered, for Helium, Oxygen, and Iron nuclei, are shown below in Fig. 2.5. It is seen that the largest variation occurs at the lower end of the energy range shown, since the CMB, whose energy spectrum is very well measured, becomes the dominant photon target for the higher energy CRs. The transition to the CMB becoming dominant is recognised in the figure as the region where the photo-disintegration lengths of the different models converge (for example, the CMB becomes the dominant photon target for Iron nuclei CRs with energies $> 10^{20}$ eV).

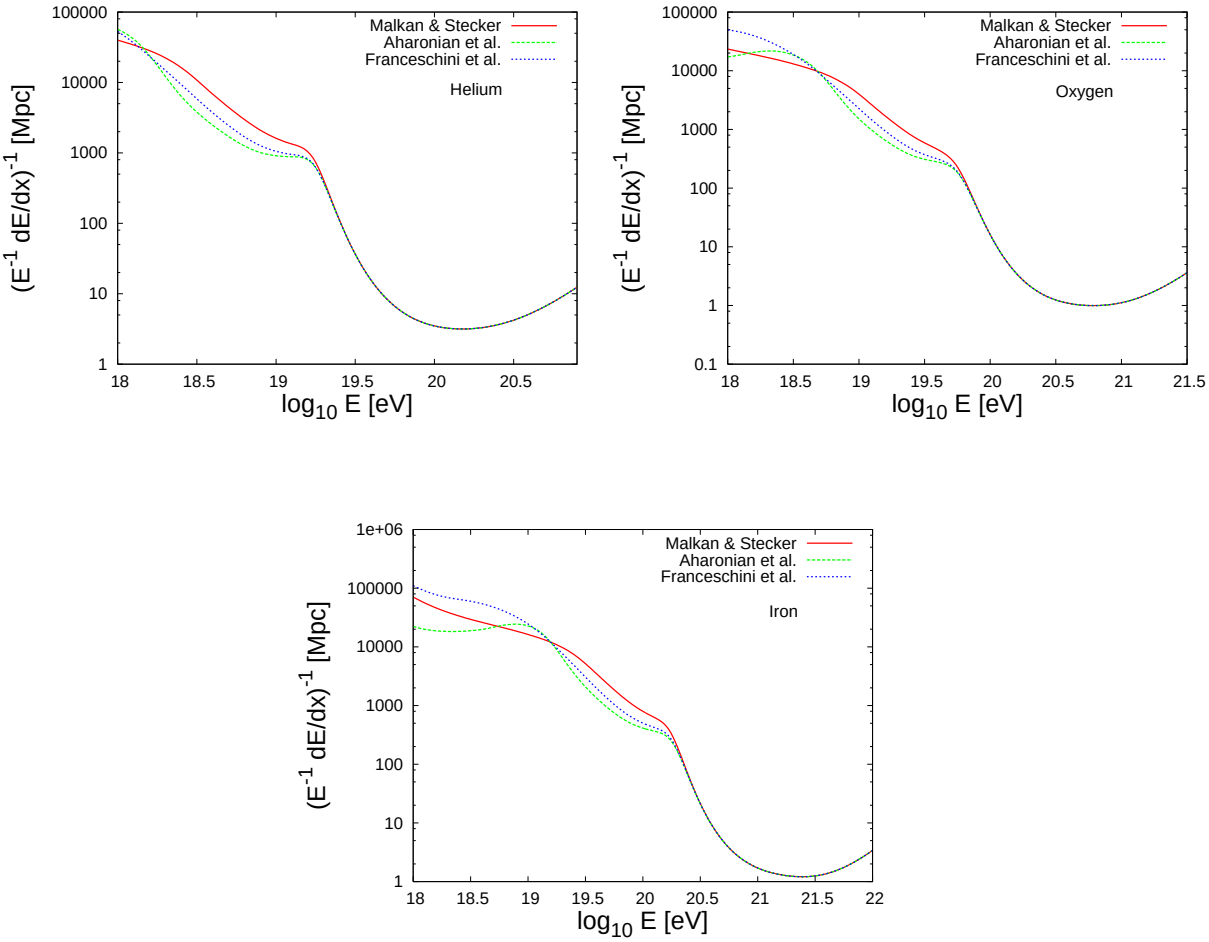

Figure 2.5: Energy loss lengths due to photo-disintegration for representative species of nuclei using three models of the CIB spectrum. The upper left, upper right and lower frames correspond to Helium, Oxygen and Iron, respectively. The Lorentzian model for photo-disintegration cross sections has been used.

To highlight the effect of the different photo-disintegration lengths for CR nuclei, the results for the propagation of Oxygen and Iron nuclei through these different radiation fields are shown in Fig. 2.6. Such results require of course assumptions about the distribution of CR sources, and the spectral energy distribution produced by each source. Here the source distribution was that motivated by the luminosity density of quasars given by the expression (2.1), and the energy distribution employed was that motived by Fermi shock acceleration (see Appendix), with a hard, charge dependent cutoff used, described by expression (2.2).

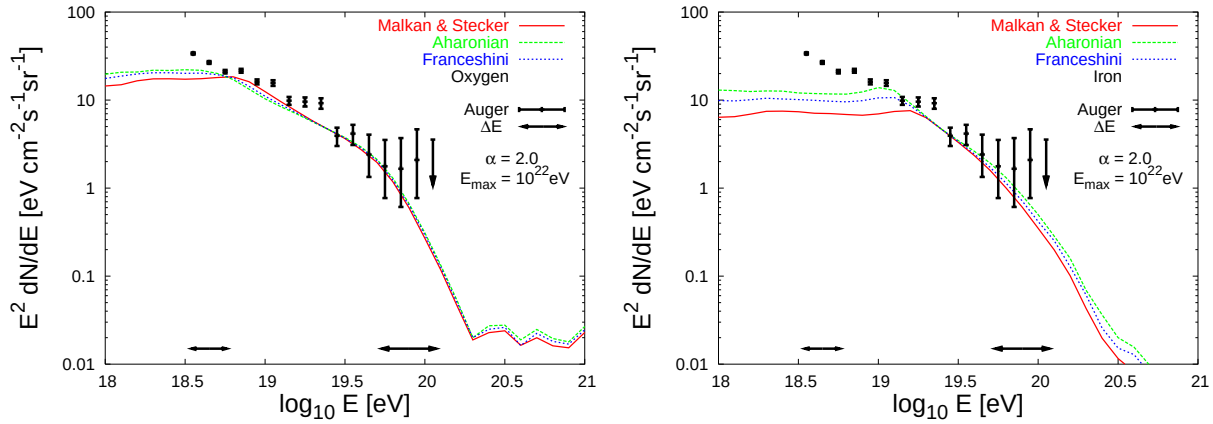

Figure 2.6: The arrival spectrum at Earth of cosmic rays, after propagating through the CMB and one of the CIB radiation fields from their source, for Oxygen nuclei primaries (left) and Iron nuclei primaries (right). The three different radiation fields considered are those shown in Fig. 2.4

As can be seen in Fig. 2.6, the differences predicted by the different CIB models exist on the few % level, in particular leading to a small variation in the energy at which photo-disintegration becomes significant. The differences introduced by the CIB models are most pronounced for Iron nuclei, since the energy at which the changeover to CMB photons becoming the dominant photon target, for propagating nuclei, is highest for Iron nuclei, as observed in Fig. 2.5.

Similarly to above, the different CIB models also allow uncertainty in the pion production lengths for protons to be highlighted, as seen in Fig. 2.7. As for the photo-disintegration lengths, the CIB is the important radiation background for the lower end of the energy range shown, though in the higher energy region the CMB becomes the dominant photon target.

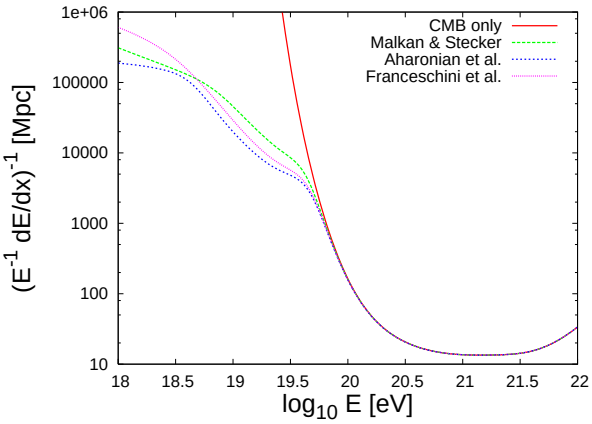

Figure 2.7: The energy loss lengths for ultra high energy protons interacting with the CMB and CIB, through $p + \gamma_{\rm CMB} \rightarrow p + \pi^0$, $p + \gamma_{\rm CMB} \rightarrow n + \pi^+$ and multi-pion production (Pion Production) interactions. The three CIB models we show here are shown in Fig. **??**.

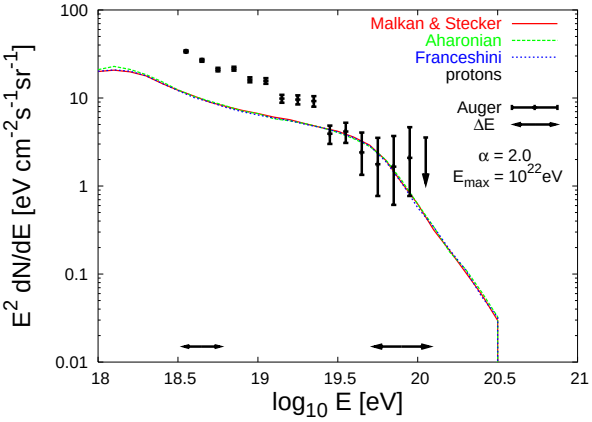

Figure 2.8: The arrival spectrum at Earth of cosmic rays, after propagating through the CMB and one of the CIB radiation fields from their source, for proton primaries. The three different radiation fields considered are those shown in Fig. 2.4

As seen in Fig. 2.8, very little variation in the arriving CR spectrum is observed for CR proton primaries. This is a consequence of the relatively large variation in the pion production rates being masked by the onset of pair production, which becomes the dominant energy loss process for protons below an energy $\sim 10^{19.6}$ eV. The signature of pair production, in the CR spectrum for proton primaries, makes itself present through a feature called "the dip", which is clearly seen in the spectra shown in Fig. 2.8 between the energies of $\sim 10^{18.2}$ - $10^{19.6}$ eV, as a gentle suppression in the spectrum. This feature is discussed in more detail in (48).

2.3 Effects of Weak Magnetics Fields

For protons or nuclei propagating through intergalactic space, deflection by magnetic fields may play an important role. The importance of these effects depending on the strength of the extragalactic magnetic field, which is subject to debate, with contrary conclusions found in (43; 44) and (45; 46).

A charged particle traveling through a uniform magnetic field undergoes angular deflection, for a particle traversing the coherence length of the magnetic field, $L_{\rm coh}$, this deflection will be of angle $\alpha{=}L_{\rm coh}/R_L$, where R_L is the Larmor radius of the particle ($R_L{=}mv/qB$, where m is the mass of the charged particle, v is it's velocity, q is it's charge, and B is the magnetic field strength). A particle traversing a total distance L, through a series of $L/L_{\rm coh}$ randomly orientated uniform magnetic fields each of length $L_{\rm coh}$, will suffer an overall deflection given by,

$$\theta(E,Z) \approx \left(\frac{L}{L_{\rm coh}}\right)^{0.5} \alpha \approx 0.8^\circ \left(\frac{10^{20}\,{\rm eV}}{E}\right) \left(\frac{L}{10\,{\rm Mpc}}\right)^{0.5} \left(\frac{L_{\rm coh}}{1\,{\rm Mpc}}\right)^{0.5} \left(\frac{B}{1\,{\rm nG}}\right) Z, \qquad (2.8)$$

where B is the representative magnitude of the magnetic fields, and E is the energy of the particle. Such deflections will result in an effective increase in the distance to a CR source. This allows an effective length $L_{\rm eff}$ to be defined, given by,

$$\frac{L_{\rm eff}}{L}(E,Z) \approx 1 + \frac{\theta^2}{2} \approx 1 + 0.065 \left(\frac{10^{20}\,{\rm eV}}{E}\right)^2 \left(\frac{L}{10\,{\rm Mpc}}\right) \left(\frac{L_{\rm coh}}{1\,{\rm Mpc}}\right) \left(\frac{B}{1\,{\rm nG}}\right)^2 \left(\frac{Z}{26}\right)^2. \qquad (2.9)$$

Thus for high energy ($>10^{20}$eV) protons and light nuclei, nG-scale magnetic fields result in $L_{\rm eff}/L$ of order unity. However, for heavy nuclei such as Iron nuclei, propagating through nG magnetic fields, the effective distance to a source 50 Mpc away is 30% larger. As this result scales with $1/E^2$, such (plausible strength) nG magnetic fields would have a dramatic effect on the propagation of lower energy nuclei.

The effects of $\sim$ nG magnetic fields, on the CR spectrum for Oxygen and Iron particles, are shown below in Fig. 2.9 for an $\alpha = 2.4$ spectral index (see 2.2).

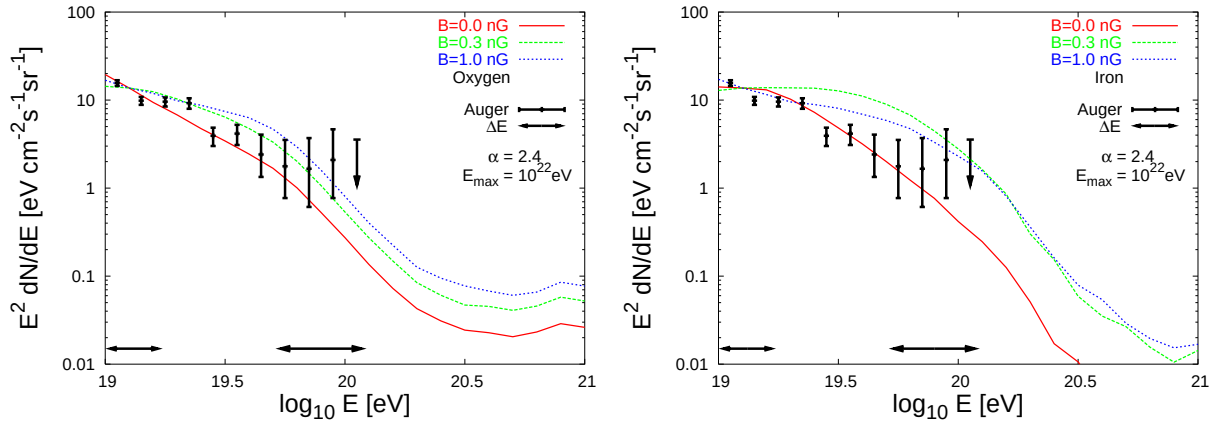

Figure 2.9: The effects of nanogauss scale extragalactic magnetic fields on the cosmic ray spectrum for Oxygen and Iron primaries with power-law spectral index $\alpha = 2.4$ and $E_{\max}$=10^{22} eV, assuming $L_{\rm coh} \sim 1$ Mpc. The Malkan & Stecker CIB model (17) and the Lorentzian model (9) for photo-disintegration cross sections have been used.

For Oxygen primaries, the effects are seen to be mostly small, only becoming significant for energies below a few times 10^{19} eV. The effects, however, are more prominant for Iron primaries. The general effect produced in the spectrum when magnetic fields are included in their propagation, is the flattening of the spectrum at the low energy end ($\sim 10^{19}$ eV). This is a consequence of the effective increase in the path length (or alternatively decrease in the energy loss length) for the lower energy particles considered, causing them to lose more energy and move further down the arriving CR spectrum.

The approximation used here, however, is only valid for weak magnetic fields (such that the energy of the particle's interaction with the field is much smaller than the energy of the particle). Oxygen nuclei with a primary energy of 5×10^{19} eV, traveling through nG-scale magnetic fields, may arrive from 300 Mpc (before significant photo-disintegration has occurred), the effective length for such a particle is $L_{\rm eff}/L \sim 1+0.7\times(B/{\rm nG})^2$, constraining this treatment to magnetic field strengths of less than $\sim$0.3 nG. On the other hand, an Iron nucleus with an energy of 5×10^{19} eV could have travelled 1000 Mpc before its arrival at Earth, so would consequently have been deflected by an angle of $\theta \sim= 130^\circ \times (L/100\,{\rm Mpc})^{0.5} \times ({\rm B/nG})$, such deflection angles lying outside the weak magnetic field regime. To properly take into account such strong deflections, a numerical simulation of diffusion, with a description of the magnetic field structure

in the local supercluster would be required. For this reason the behavior shown in the Iron spectrum, at the lower energies, in Fig. 2.9, are not robust, though the basic features displayed are indicative of the likely effect nG magnetic fields would have on heavy nuclei CR propagation in this energy range.

2.4 Composition of Ultra High Energy Cosmic Rays

In this section, the effect of the composition at source on the UHECR spectrum at Earth will be investigated for various types of nuclei injected. The photo-disintegration rates, which assume the Malkan & Stecker CIB model and the Lorentzian model giant dipole resonance cross-sections, for various nuclei are shown below in Fig. 2.10,

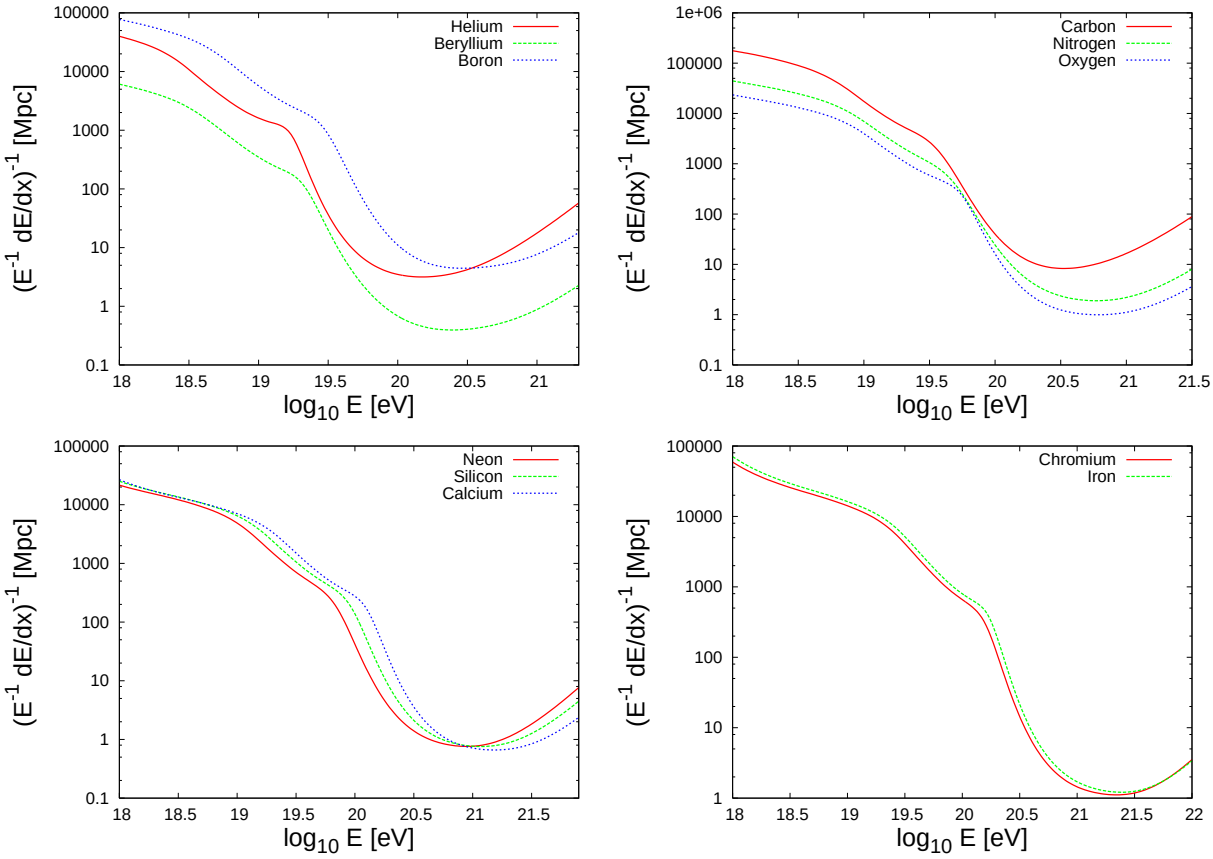

Figure 2.10: Energy loss lengths due to photo-disintegration for a range of intermediate mass and heavy nuclei. The Malkan & Stecker CIB model (17) and the Lorentzian model (9) for photo-disintegration cross-sections have been used.

As seen there are significant variations in the photo-disintegration rates for different nuclei, with Carbon nuclei being relatively resistant to photo-disintegration, with an energy loss length of ∼1000 Mpc at 3×10^{19} eV, and ∼50 Mpc at 10^{20} eV, whereas Beryllium nuclei being more fragile, with an energy loss length smaller than that for Carbon by about a factor of ∼10-100. As a rule, very heavy nuclei are found to be quite stable up to energies of 10^{20} eV.

As a particle injected as a particular species propagates however, it may undergo several photo-disintegration processes, cascading down through A and Z number. The secondary particles produced through disintegration, such as protons, neutrons, and alpha particles, go on to propagate, and contribute also to the arriving spectrum.

Shown below are the results from such propagation for the case of different species being injected at source. The different nuclei considered here were selected as they are observed to be particularly abundant in the arriving CR spectrum, at lower energies (10^8eV/nucleon) where the CR composition may be measured (47), through the employment of spectroscopic detectors onboard satellites (see Chapter 1 for a discussion of the CR composition).

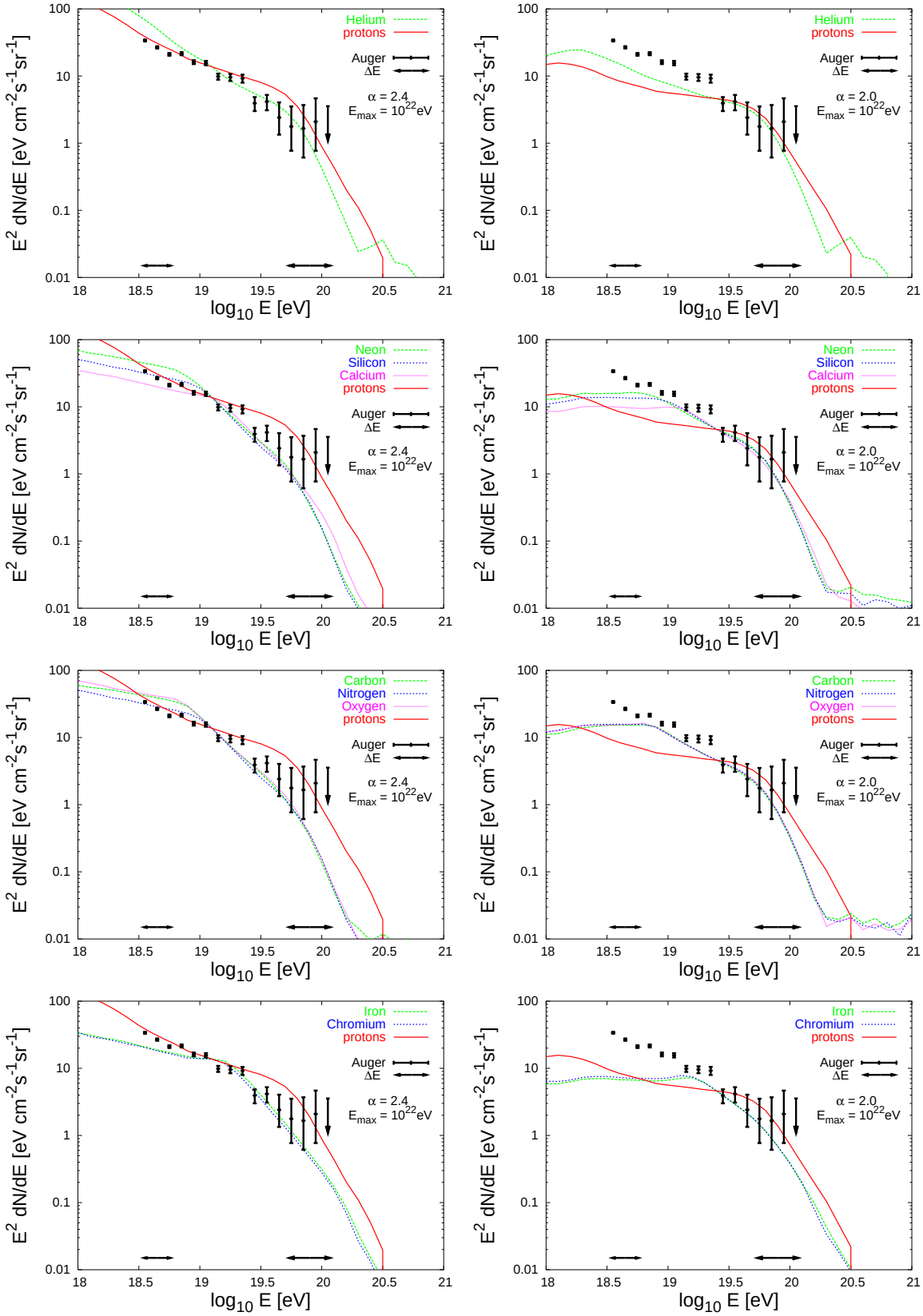

Figure 2.11: The spectrum of ultra high energy cosmic rays observed at Earth for a range of injected heavy nuclei with power-law spectral index $\alpha = 2.4$ or 2.0 and $E_{\max} = 10^{22}$ eV. The Malkan & Stecker CIB model (17) and the Lorentzian model (9) for photo-disintegration cross sections have been used. The effects of magnetic fields have not been included.

For the cases where intermediate or heavy nuclei are injected at the distant CR source, the nuclei gradually disintegrate into lighter nuclei and nucleons upon propagation through the interstellar radiation field. As a result, depending upon the propagation distance, the CR composition observed at Earth can be quite different from that injected at the source.

This is most clearly highlighted in Fig. 2.12, in which the average atomic mass in the spectrum arriving at Earth is plotted as a function of the arriving particle's energy.

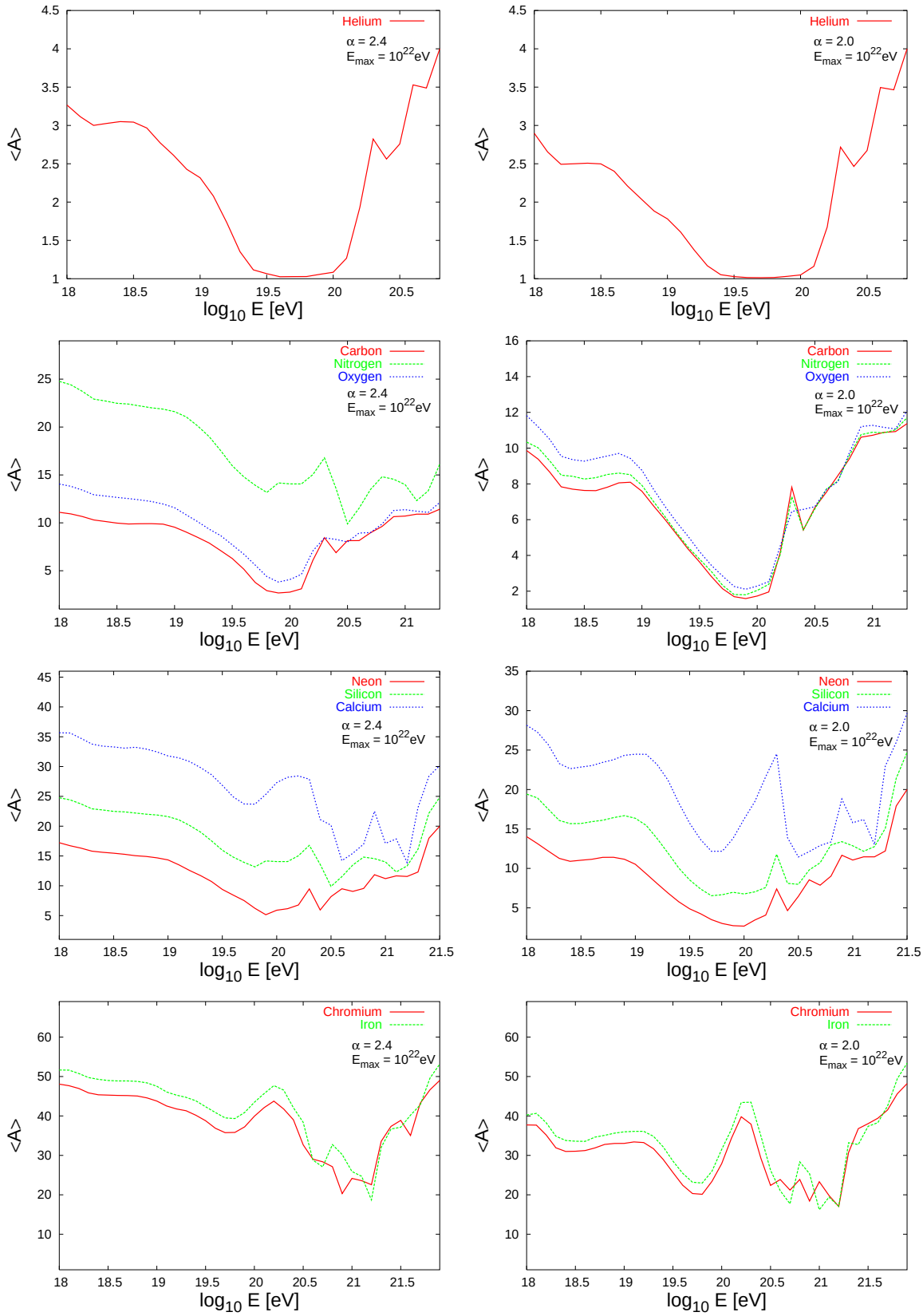

Figure 2.12: The mean atomic mass of cosmic rays arriving at Earth for a range of injected heavy nuclei with power-law spectral index $\alpha = 2.4$ or 2.0 and $E_{\max} = 10^{22}$ eV. The Malkan & Stecker CIB model (17) and the Lorentzian model (9) for photo-disintegration cross sections have been used. The effects of magnetic fields have not been included.

As can be seen in the Fig. 2.12, the composition arriving at Earth has a distinctive dependence on energy, particularly in the energy range 3×10^{19} - 10^{20} eV. For sources injecting intermediate mass nuclei, the mean mass number arriving exhibits a well defined minimum. This minimum, residing in the energy region between photo-disintegration becoming significant, and the upper limit of the injected energy spectrum. The energy at which the decrease in the arriving mean atomic mass is seen, marks the onset of total photo-disintegration. Countering this, the rise in the arriving mean atomic mass at high energies is purely a consequence of the upper bound on the energy spectrum injected at source, placing a limit on the subsequent energies of the protons producible through the disintegration of nuclei (each nucleon taking $1/A$ of the parent nuclei's energy). This minimum is seen to be less pronounced for the injection of heavy nuclei, which produce a distinctly heavier effective composition at Earth (though this result has some dependence on the spectral index of the energy injection spectrum, as seen in Fig. 2.12). These results for the mean atomic composition arriving at Earth for different composition at source being of particular importance for the elongation rate values measured, which provide the possibility for the determination of the arriving composition.

2.5 Summary

The change in the interaction rates through the application of Lorentzian type cross-sections over the Gaussian parameterisation was found to be small. The subsequent effect of this on the cosmic ray spectrum results suggesting that such improvements on the cross-section are presently of little benefit with regards to cosmic ray nuclei propagation (see Fig. 2.3). Similarly, the present uncertainty on the infra-red background radiation is found to have a negligible effect on cosmic ray proton propagation calculations, though the effect is perhaps relevant with regards cosmic ray nuclei propagation (see Fig. 2.6). Within the present uncertainty of the strengths of the extragalactic magentic fields, they are found to have the potential to play an important role in the shape of the arriving cosmic ray spectrum. The effect being most pronounced for the propagation of heavy nuclei through large extragalactic magnetic fields (see Fig. 2.9), for which the weak magnetic field approximation fails and diffusive transport must be considered. The CR composition at source is also found to have a significant effect on the

arriving CR spectral shape (see Fig. 2.11).

Chapter 3

An Analytic Treatment of Ultra High Energy Cosmic Ray Nuclei Propagation

In Chapter 2, cosmic ray nuclei propagation was considered through the application of a Monte Carlo technique. Where possible, these results have been tested and compared with the results of similar calculations carried out by other groups, all cases finding reasonable agreement. Through research into the dominant factors determining the photodisintegration rates for nuclei, an analytic treatment for UHECR nuclei propagation is developed. This new analytic treatment showing good agreement with the Monte Carlo results.

3.1 Assumptions in the Analytic Treatment

A full analytic treatment of the nuclear propagation would involve a consideration of all the possible decay routes. The differential equations set up through such consideration would be highly non-trivial to solve, and would be no simpler to implement than the Monte Carlo approach. For example, if the temporal distribution of the population of state q is described by f_q, and could be decayed into from higher states, $q+1$, $q+2$,..., and could decay into states $q-1$,$q-2$, ...the differential equation describing the number of particles in state q would be,

$$\frac{df_q}{dz} + \frac{f_q}{z_{q\rightarrow q-1}} + \frac{f_q}{z_{q\rightarrow q-2}} + ... = \frac{f_{q+1}}{z_{q+1\rightarrow q}} + \frac{f_{q+2}}{z_{q+2\rightarrow q}} + ..., \tag{3.1}$$

where $z_{q\to q-1}$ is the decay time of state q into state $q-1$.

However, following from the results of Chapter 2, in particular the agreement found between the Gaussian cross-section description with a single decay route and a Lorentzian cross-section description with a decay network, the differential equation may be simplified by a reduction in the number of states considered in the system.

The situation may be further simplified by the assumption that only single nucleon loss of nuclei need be considered. This simplification being motivated by more recent work from the author that developed the original Gaussian model (10; 27). In this revised work, only single and double nucleon loss processes are considered.

With these assumptions, the number of states considered in the system, and the possible transitions between them, are vastly reduced, simplifying the differential equation describing the number of particles in state q, given before by equation (3.1), as,

$$\frac{df_q}{dz} + \frac{f_q}{z_q} = \frac{f_{q+1}}{z_{q+1}}, \tag{3.2}$$

where a slight change of notation has been used here, since a particle in state $q+1$, may only decay into state q (what was written before as $z_{q\to q-1}$ will here be written as z_q).

3.2 Development of a Solution

The differential equation satisfied by f_q is,

$$\frac{df_q}{dz} + \frac{f_q}{z_q} = \frac{f_{q+1}}{z_{q+1}}. \tag{3.3}$$

This may be written as,

$$\exp\left(\frac{-z}{z_q}\right)\frac{d}{dz}\exp\left(\frac{z}{z_q}f_q\right) = \frac{f_{q+1}}{z_{q+1}}, \tag{3.4}$$

so that

$$f_q = \exp\left(\frac{-z}{z_q}\right)\int dz \exp\left(\frac{z}{z_q}\right)\frac{f_{q+1}}{z_{q+1}}, \tag{3.5}$$

with the initial conditions of the system being, at $z=0$, $f_n(0)\neq 0$ and $f_q(0)=0$ (for $q\neq n$).

Assume solution for q is,

$$\frac{f_q(z)}{f_n(0)} = \sum_{m=q}^{n} z_q z_m^{n-q-1} \exp\left(\frac{-z}{z_m}\right) \prod_{p=q}^{n} \frac{1}{z_m - z_p}, \tag{3.6}$$

where n is the initial state the particles are in. The following will be a proof by induction.

If true for q, then true for $q+1$,

$$\frac{f_{q+1}(z)}{f_n(0)} = \sum_{m=q+1}^{n} z_{q+1} z_m^{n-q-2} \exp\left(\frac{-z}{z_m}\right) \prod_{p=q+1}^{n} \frac{1}{z_m - z_p}, \tag{3.7}$$

which using (3.5) gives,

$$\begin{aligned}
\frac{f_q(z)}{f_n(0)} &= \exp\left(\frac{-z}{z_q}\right) \int dz \exp\left(\frac{z}{z_q}\right) \sum_{m=q+1}^{n} z_m^{n-q-2} \exp\left(\frac{-z}{z_m}\right) \prod_{p=q+1}^{n} \frac{1}{z_m - z_p} && (3.8)\\
&= \sum_{m=q+1}^{n} z_m^{n-q-2} \prod_{p=q+1}^{n} \frac{1}{z_m - z_p} \left[(\frac{1}{z_q} - \frac{1}{z_m}) \exp\left(\frac{-z}{z_m}\right)\right] - c \exp\left(\frac{-z}{z_q}\right) && (3.9)\\
&= \sum_{m=q+1}^{n} z_q z_m^{n-q-1} \prod_{p=q+1}^{n} \frac{1}{z_m - z_p} \left[(\frac{1}{z_m - z_q}) \exp\left(\frac{-z}{z_m}\right)\right] - c \exp\left(\frac{-z}{z_q}\right), && (3.10)
\end{aligned}$$

where c is such that $f_q(0) = 0$. For this to be the case,

$$c = \sum_{m=q+1}^{n} z_q z_m^{n-q-1} \prod_{p=q}^{n} \frac{1}{z_m - z_p}. \tag{3.11}$$

For (3.10) and (3.6) to be equivalent and c to be the next term in the series,

$$\sum_{m=q+1}^{n} z_q z_m^{n-q-1} \prod_{p=q}^{n} \frac{1}{z_m - z_p} = z_q z_q^{n-q-1} \prod_{p=q}^{n} \frac{1}{z_q - z_p} \tag{3.12}$$

This final expression may be more simply recognised as an expression of the Vandermond determinant with the final row repeated. This is demonstrated explicitly with an example. Let $n = 3$ and $q = 0$ for the expression (3.12), this gives,

$$\frac{w^2}{(w-x)(w-y)(w-z)} + \frac{x^2}{(x-w)(x-y)(x-z)} + \frac{y^2}{(y-w)(y-x)(y-z)} = -\frac{z^2}{(z-w)(z-x)(z-y)},$$

so

$$\frac{w^2}{(w-x)(w-y)(w-z)} + \frac{x^2}{(x-w)(x-y)(x-z)} + \frac{y^2}{(y-w)(y-x)(y-z)} + \frac{z^2}{(z-w)(z-x)(z-y)} = 0, \quad (3.13)$$

which may be expressed as the determinant of a matrix,

$$\begin{vmatrix} 1 & w & w^2 & w^2 \\ 1 & x & x^2 & x^2 \\ 1 & y & y^2 & y^2 \\ 1 & z & z^2 & z^2 \end{vmatrix} = 0. \quad (3.14)$$

Since,

$$\begin{vmatrix} 1 & w & w^2 \\ 1 & x & x^2 \\ 1 & y & y^2 \end{vmatrix} = \prod_{i=1}^{j}(x_i - x_j). \quad (3.15)$$

The expression (3.14), gives,

$$w^2(x-y)(y-z)(z-x) - x^2(w-y)(y-z)(z-w)) + y^2(w-x)(x-z)(z-w) - z^2(w-x)(x-y)(y-w) = 0,$$

dividing this throughout by $(x-y)(y-z)(z-x)(w-y)(w-z)(w-x)$ gives,

$$\frac{w^2}{(w-x)(w-y)(w-z)} + \frac{x^2}{(x-y)(x-z)(x-w))} + \frac{y^2}{(y-x)(y-z)(y-w)} + \frac{z^2}{(z-x)(z-y)(z-w)} = 0, \quad (3.16)$$

and shows (3.13) to be true. This verifies the general expression 3.12 for $n = 3$ and $q = 0$.

3.3 A Comparison of the Analytic Solution with the Monte Carlo Simulation

In the expression for the analytic solution given by (3.6), the spatial distribution of a species q, of energy $E_q(= \frac{A_q}{A_n}E_n)$ (this expression ignores pair production and redshift energy losses during the cascade) is given, where A_q is the atomic number of species q, and n is the state initially populated.

From now on, the energy of the initial state, E_n, will be referred to as E, and the time

elapsed since the system was set up will be z. The fraction of particles in state q, with mass number A_q and of energy $E_q(=\frac{A_q}{A_n}E)$, produced from a source of mass number A_n with energy E, after time z, is

$$\frac{f_q(z,E_q)}{f_n(0,E)} = \sum_{m=q}^{n} z_q(E_q) z_m(E_m)^{n-q-1} \exp\left(\frac{-z}{z_m(E_m)}\right) \prod_{p=q(\neq m)}^{n} \frac{1}{z_m(E_m) - z_p(E_p)}, \qquad (3.17)$$

where $\frac{f_q(z,E_q)}{f_n(0,E)}$ is the fraction of all the particles that are in that species, and $E_m \approx \frac{A_m}{A_n}E$, and similarly for E_p and E_q.

With a knowledge of the lifetimes of each state, z_q, which here are the photodisintegration times for each nuclear species and are energy dependent, the population of any given species after time z may be determined with expression (3.17). As mentioned previously, though pair production and redshift energy loss could also be included in the analytic treatment, it is simpler and equally valid to ignore such energy loss processes in the Monte Carlo simulation for a fair comparison of the two approaches.

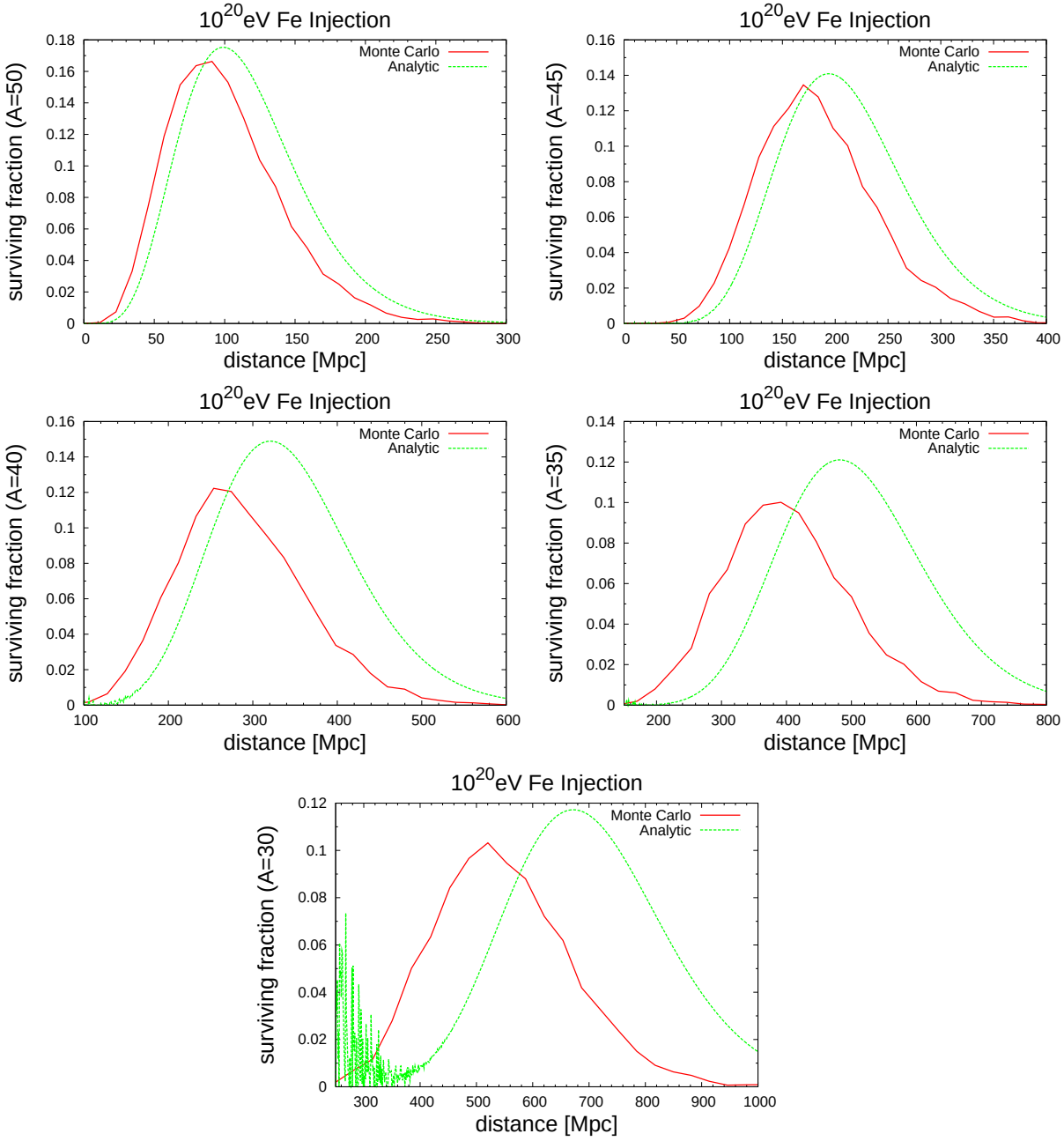

Figure 3.1: Comparison plots of the analytic and Monte Carlo results for the species A=50, 45, ...30. The fraction of all particles that are in that particular state, as a function of distance, having all been initially (z=0) injected as Iron particles with an energy of 10^{20}eV, are shown for the two treatments.

Fig. 3.1, which looks at the population of a particular species as a function of distance (converts to time through c, the speed of propagation of the particles) from the source, shows good agreement for the heavier nuclei and reasonable agreement for lighter nuclei. The increase

in disagreement with lighter nuclei (smaller A), observed in Fig. 3.1, is perhaps expected since particles descending down to a lighter species, in the Monte Carlo simulation, will sample more multi-nucleon loss channels as they descend, than particles that descend less far through (A,Z) space and arriving still as a relatively heavy species. Since the analytic approach deals only with single nucleon loss, the more multi-nucleon loss channels used during a particle's decay, within the Monte Carlo framework, the larger the difference expected between the two results. The sign of the discrepancy, with the analytic result peaking at larger distances than the Monte Carlo result, can be explained by the fact that the single nucleon propagation approach forces every state to be passed through, whereas the multi-nucleon loss approach allows states to be skipped over, allowing lighter species to be reached within a shorter distance from the source. A further feature in Fig. 3.1 to note are the large fluctuations seen in the final plot for A=30. These fluctuations are a result of numerical limitations for the summing of large numbers, whose sum is a value of order 1. Such features are have an increasing presence in the results of the analytic treatment, and become a limiting factor in the energy range that may be considered via this approach.

3.4 The Distribution of Secondary Particles

In this and subsequent sections, the variable z will be used to describe the distance travelled by the particle.

At each photodisintegration interaction a proton is also produced. The population of these protons will be described by f_1. The differential equation satisfied by f_1 is,

$$\frac{df_1(E)}{dz} = \frac{f_n(z, E_n)}{z_n(E_n)} + \frac{f_{n-1}(z, E_{n-1})}{z_{n-1}(E_{n-1})} + ... \frac{f_2(z, E_2)}{z_2(E_2)}, \tag{3.18}$$

where $E = E_n/n$.

All protons produced during a cascade, due to a primary particle of species n with energy E, have an energy $\frac{1}{A_n}E$. However, through interactions with ambient CMB and CIB photons, the energy distribution of these protons is altered during propagation, from their generation in the cascade, to Earth.

Integrating the expression (3.18) given above, over z, an expression for f_1 at distance z'

and energy E_1, is given by,

$$f_1(z', E_1) = \int_0^{z'} dz \sum_{m=2}^{n} \frac{f_m(z, E_m)}{z_m(E_m)}, \tag{3.19}$$

where $E_1 = \frac{1}{A_n}E$. From this expression it is clear that for sufficiently large z', each of the different species will contribute equally to the proton injection spectrum, providing n protons in total.

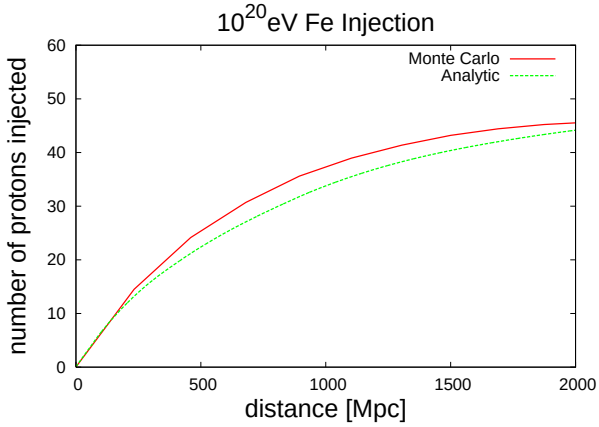

Figure 3.2: A comparison of the analytic and Monte Carlo results for protons. The number of introduced protons, as secondaries produced through photodisintegration, as a function of distance, are shown for the two treatments (to obtain this plot the cascade was developed between A=56 and A=10). For this plot, iron nuclei with an energy of 10^{20} eV were propagated from the source.

The comparison of the analytic and Monte Carlo methods shown in Fig. 3.2 for determining the number of protons produced through photodisintegration, as a function of the distance from the source, shows reasonable agreement, particularly for distances ∼100 Mpc or less. However, the growing disagreement between the two treatments is clearly observed, with the number of protons produced by the analytic method growing slower than the protons produced by the Monte Carlo method. This result agreeing with the previous explanation of the discrepancy between the two treatments, that nuclei of a given energy take longer to photodisintegrate in the analytic model, compared to the Monte Carlo model.

3.5 Application of The Analytic Result to a Specific Injection Spectrum and Spatial Distribution of Sources

From the result derived, given in (3.6), the spatial distribution of a species q, of energy $E_q(=\frac{A_q}{A_n}E)$ produced from a source of species n with energy E at distance z, is,

$$\frac{f_q(z,E_q)}{f_n(0,E)} = \sum_{m=q}^{n} z_q(E_q) z_m(E_m)^{n-q-1} \exp\left(\frac{-z}{z_m(E_m)}\right) \prod_{p=q}^{n} \frac{1}{z_m(E_m) - z_p(E_p)}, \tag{3.20}$$

where $E_m{=}\frac{A_m}{A_n}E$, and $E_p{=}\frac{A_p}{A_n}E$.

So, for a given energy E, the spatial distribution of all particles with this energy is the sum of these terms over all species, with different energy nuclei at source, E_n, for each different species,

$$f_{\rm all}(z,E) = \sum_{q=l}^{n} \frac{f_q(z,E_q)}{f_n(0,E_n)}, \tag{3.21}$$

where $E_q = \frac{A_n}{A_q}E$.

If the particles are injected over a range of distances z, from 0 to $z_{\rm max}$, with a distribution described by the normalised function $d(z)$, then the number of a particular species q, at an energy E, is,

$$N_q(E_q) = \int_0^{z_{\rm max}} dz \frac{f_q(z,E_q)}{f_n(0,E_n)} d(z), \tag{3.22}$$

where $E_q = \frac{A_n}{A_q}E$.

If particles are injected with an energy spectrum $(dN/dE) \propto E^{-\alpha}$, the total number of all particles at an energy E_q is,

$$N_{\rm tot}(E_q) = \sum_{q=l}^{n} \frac{dN}{dE} N_q(E_q) \tag{3.23}$$

$$= \sum_{q=l}^{n} (\frac{A_n}{A_q})^{1-\alpha} N_q(E), \tag{3.24}$$

where l is the lowest species considered in the cascade.

3.6 A Further Improvement on the Analytic Model

A consideration of a full solution to (3.1), which includes the decay of the state through multi nucleon loss, could be found through a network of differential equations, expressed as,

$$\frac{d}{dt}\underline{\mathrm{f}} = \Lambda\underline{\mathrm{f}}, \tag{3.25}$$

where $\underline{\mathrm{f}}$ is a vector of length n describing all n states of the system, and Λ, is an $n \times n$ matrix describing the transition rates between states, which may be expressed as,

$$\Lambda = \begin{pmatrix} -(\frac{1}{z_{n\to n-1}} + \frac{1}{z_{n\to n-2}} + ...) & 0 & 0 \\ \frac{1}{z_{n\to n-1}} & -(\frac{1}{z_{n-1\to n-2}} + \frac{1}{z_{n-1\to n-3}} + ...) & 0 \\ \frac{1}{z_{n\to n-2}} & \frac{1}{z_{n-1\to n-2}} & (\frac{1}{z_{n-2\to n-3}} + \frac{1}{z_{n-2\to n-4}} + ...) \end{pmatrix}, \tag{3.26}$$

(which notes that all states eventually decay, and that states may only be decayed into from higher states) where the notation $z_{n\to m}$ refers to the transition distance for state n going to state m. This may be solved by determining the eigenvalues of Λ, and expressing $\underline{\mathrm{f}}$ as a linear sum of the eigenvectors, with exponential time dependence, ie.

$$\underline{\mathrm{f}}(t) = \Sigma_{m=1}^{n} A_n \exp(\lambda_n t)\,\underline{\mathrm{f}}_n, \tag{3.27}$$

where λ_n are the eigenvalues, and $\underline{\mathrm{f}}_n$ are the eigenvectors, of the matrix Λ, and A_n are constants determined by the initial populations of the different states.

However, the determination of this solution is not simple, and reasonable agreement is already found with the consideration of only single nucleon loss.

Further improvement of the single nucleon loss approximation will be sought here through noting that the comparison between the analytic and Monte Carlo results in Fig. 3.1, reveals that the single nucleon states in the Monte Carlo simulation take longer to decay from the highest state into lower states, than equivalent states in the analytic model. This explanation also being consistent with the explanation given for the discrepancy seen in Fig. 3.2.

Instead, a new form of the decay times will be used, motivated by the decay length of states when multi-nucleon loss is considered. The single nucleon loss decay times will be replaced by

the reduced (effective) decay times from multi-nucleon loss, given by,

$$z_{eff} = \left(\frac{1}{z_1} + \frac{1}{z_2} + ... \right)^{-1}, \tag{3.28}$$

where z_n is the decay time for n-nucleon loss.

The results of this alteration to the analytic model are shown below in Fig. 3.3.

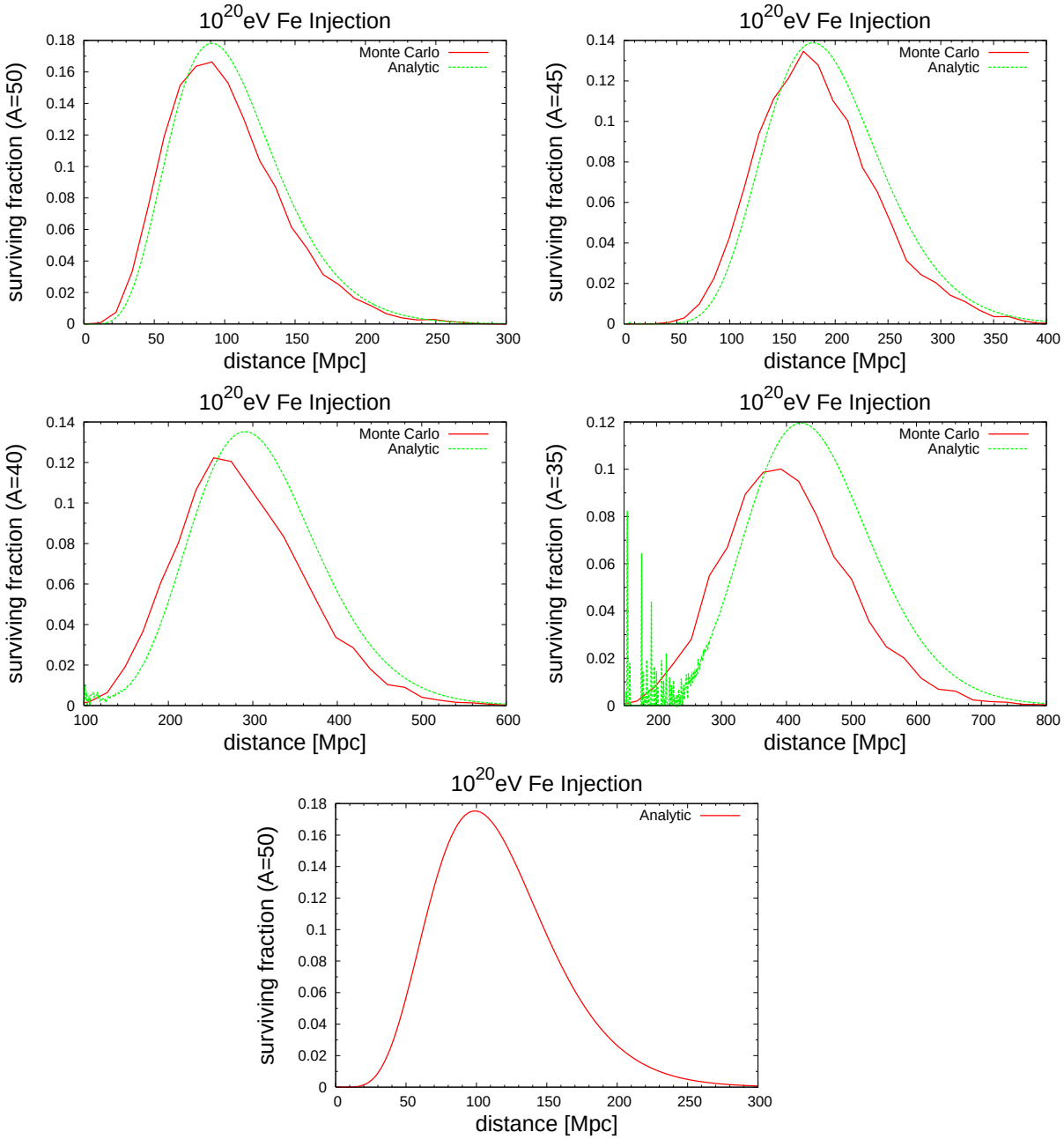

Figure 3.3: Comparison plots of the modified analytic and Monte Carlo results for the species A=50, 45, ...30. The fraction of all particles that are in that particular state, as a function of distance, having all been initially (z=0) injected as Iron particles with an energy of 10^{20} eV, are shown for the two treatments.

The agreement for the modified analytic treatment shown in Fig. 3.3 is clearly an improvement on that seen for the original analytic treatment seen in Fig. 3.1, with the peaks of the analytic and Monte Carlo distributions sitting at roughly the same distance. A decrease in

this agreement for lighter nuclei is once again observed, due to the analytic method, unlike the Monte Carlo method, ignoring the possibility of multi-nucleon loss. This improvement is also observed in the plot below showing the total number of secondaries, due to photodisintegration, produced as a function of distance propagated by the nuclei.

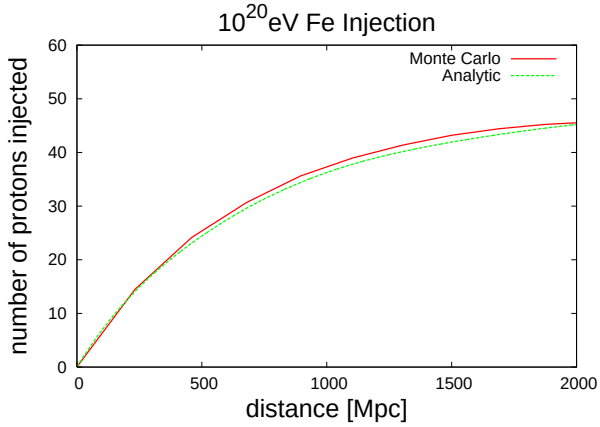

Figure 3.4: A comparison of the modified analytic and Monte Carlo results for protons. The number of introduced protons, as secondaries produced through photodisintegration, as a function of distance, are shown for the two treatments (to obtain this plot the cascade was developed between A=56 and A=10). For this plot, iron nuclei with an energy of 10^{20} eV were propagated from the source.

For the specific case of protons injected with E_{max} of $10^{20.25}$ eV (Fe injected with E_{max} of 10^{22} eV) propagating through the CMB radiation field, the dominant energy loss process is shown in Fig. 4.1. The changeover of the dominant energy loss mechanism, from pion production in the energy range $10^{19.6}$ - $10^{20.25}$ eV, to pair creation in the energy range $10^{18.2}$ - $10^{19.6}$ eV, and adiabatic energy loss due to the expansion of the Universe for energies below $10^{18.2}$ eV. These energy loss processes limit the distance over which CR protons may travel, and though not part of the analytic treatment, will be important consequence on the determination of the CR spectrum and average composition arriving at Earth.

3.7 Average Composition Arriving at Earth

In Chapter 2, the average composition of the CRs arriving at Earth, having left the source as a particular species and propagated through the CMB and CIB radiation fields, were shown in

Fig. 2.12 for different initial nuclei (Iron, Calcium, Silicon...Helium) and energy spectra (α=2, 2.4). Such plots may here be compared with equivalent plots produced by applying the analytic treatment instead.

The number of a given species with an energy E, at distance z from the source, is given by expression (3.22), allowing the total number of particles at energy E to be determined, consequently the average number of particles arriving at energy E, $\langle A \rangle$, is given by,

$$\langle A(E_q) \rangle = \frac{\sum_{q=1}^{n} A_q N_q(E_q)}{N_{tot}(E_q)}. \tag{3.29}$$

Applying this now to the specific situation of Iron nuclei being injected into the CR source distribution, and focussing purely on the particles that arrive with an energy of 10^{20} eV, the distribution of the different nuclei from a specific source, given by expression (3.20), are shown below in Fig. 3.5, and from such distribution functions the average composition arriving from a CR source distribution, with a particular energy spectrum for each source, may be determined.

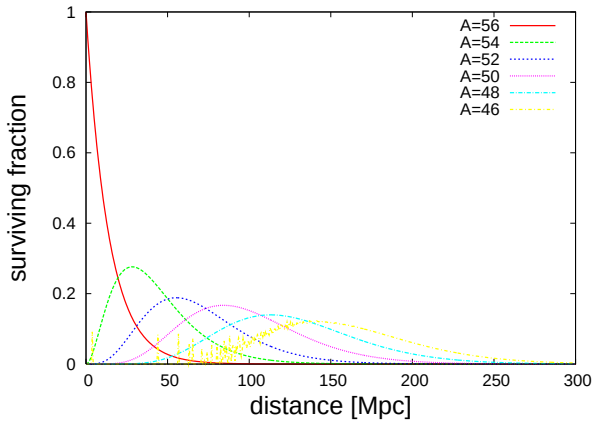

Figure 3.5: The surviving fractions of different nuclear species, each with an energy of 10^{20} eV, as a function of distance away from the source (z=0) where Iron nuclei are injected

Integrating these spatial distribution functions over the distance range the particles are able to propagate, the total number of each species arriving from a uniform distribution of sources is shown in the Table 3.1,

Table 3.1: The total number of particular species (A) arriving at Earth from a uniform distribution of sources and with an equal number of Iron nuclei injected into each logarithmic energy bin at each source

Species	$N_q(10^{20}$ eV)
A=56	14.2
A=54	13.8
A=52	11.9
A=50	12.7
A=48	10.5

these results are obtained from simple analytic expressions for the species considered by integrating (3.20) over distance,

$$N_q(E_q) = \sum_{m=q}^{n} z_q(E_q) z_m(E_m)^{n-q} \prod_{p=q}^{n} \frac{1}{z_m(E_m) - z_p(E_p)} \left[\exp\left(\frac{-z}{z_m(E_m)} \right) \right]_{zmax}^{0}. \qquad (3.30)$$

For all of the nuclei shown in Fig 3.5, the range of distances used, described by (2.1), contain the full spatial distribution functions, allowing (3.30) to be expressed as,

$$N_q(E_q) = \sum_{m=q}^{n} z_q(E_q) z_m(E_m)^{n-q} \prod_{p=q}^{n} \frac{1}{z_m(E_m) - z_p(E_p)}. \qquad (3.31)$$

For E_q to take the same value for all nuclei, the energy spectrum of the source must be taken into account, as noted in (3.24), giving,

$$N_q(E) = \sum_{m=q}^{n} \left(\frac{A_n}{A_q} \right)^{1-\alpha} z_q(E_q) z_m(E_m)^{n-q} \prod_{p=q}^{n} \frac{1}{z_m(E_m) - z_p(E_p)}. \qquad (3.32)$$

A consideration of the number of proton secondaries arriving at Earth, produced through photodisintegration processes, however, is a little more involved, with the need for the consideration of both the production of secondary protons through photodisintegration, and the subsequent pair creation and pion production energy loss processes of the protons through their interaction with the photon background.

The first of these, the determination of the number of protons produced through photodis-

integration, is given by (3.18). This expression allows a similar plot to that shown above in Fig. 3.4, though instead of the number of protons produced by the subsequent disintegration of 10^{20} eV Iron nuclei, here the number of protons at 10^{20} eV, produced by the disintegration of 56×10^{20} eV Iron nuclei (A_{56}), will be considered. A similar plot to Fig. 3.4 for this case is shown below in Fig. 3.6,

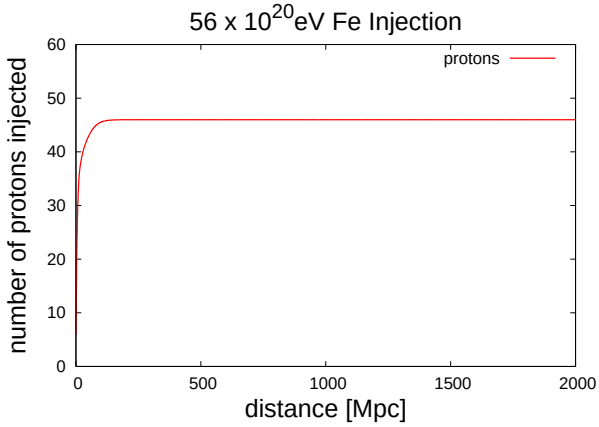

Figure 3.6: The number of 10^{20} eV protons produced through photodisintegration interactions of nuclei, as a function of distance, determined with the analytic method

As seen from Fig. 3.6, total photodisintegration of a 56×10^{20} eV injected Iron nuclei has occurred by the time it has propagated $\sim$100 Mpc. However, the pion energy loss lengths shown in Fig. 4.1, reveal that a limit of $z_{\rm pion}(10^{20}\ {\rm eV})\sim150$ Mpc is placed on the range of 10^{20} eV protons (a more accurate analysis actually limits the protons that can arrive with 10^{20} eV to <80 Mpc). This allows an estimation of $N_1(E_1)$ to be made,

$$N_1(E_1) = \int_0^{z_{pion}(E_1)} dz' f_1(z', E_1). \tag{3.33}$$

As for the nuclei case, for E_1 to take the same value as the nuclei above, E, the energy spectrum of the source must be accounted for, giving,

$$N_1(E) = \left(\frac{A_n}{1}\right)^{1-\alpha} \int_0^{z_{pion}(E_1)} dz' f_1(z', E_1) \tag{3.34}$$

$$= \left(\frac{A_n}{1}\right)^{1-\alpha} \int_0^{z_{pion}(E_1)} dz' \int_0^{z'} dz \sum_{m=2}^{n} \frac{f_m(z, E_m)}{z_m(E_m)}. \tag{3.35}$$

Applying this result, also, to the specific case of Iron nuclei being injected with 56×10^{20} eV, such that the protons produced have 10^{20} eV, and combining it with the previous results for the number of 10^{20} eV nuclei produced, a table of the number of all the species arriving at Earth with an energy of 10^{20} eV is obtained.

Table 3.2: The total number of particular species (A) arriving at Earth from a uniform distribution of Iron nuclei sources with particles at each source injected according to an energy spectral index α

Species	$N_q(10^{20}$ eV), α=1	$N_q(10^{20}$ eV), α=2
A=56	14.2	14.2
A=54	13.8	13.3
A=52	11.9	11.0
A=50	12.7	11.3
A=48	10.5	9.0
A=1	4400.0	78.6

It should be mentioned here that a charge dependent energy limit, as used in Chapter 2, was used in this calculation, such that nuclei with different charges are accelerated up to different energies. This limits the maximum proton energy in the system to be less than $10^{20.25}$ eV.

With these results, the value for the mean composition of 10^{20} eV CRs arriving at Earth from a uniform distribution of sources, each with an energy spectral index of α=2, shown in Fig. 2.12 of the previous chapter, may be more fully understood. The arriving CRs being essentially composed of a nuclei and proton component, with approximately 5 times more protons than Iron nuclei being expected in the arriving spectrum of 10^{20} eV CRs.

Through a similar application, determining the number of each species arriving at Earth with the analytic treatment, over the whole energy range considered, both the arriving CR spectrum, and average composition were obtained, as shown in Fig. 3.7 below. Numerical limitations on the analytic treatment, due to the large exponentials involved, limit the result obtainable with it here to energies below $10^{20.2}$ eV. Good agreement between the analytic and Monte Carlo methods over this energy range is found. To obtain these result, both the

energy loss due to pair creation and adiabatic expansion of the Universe were included in the calculation.

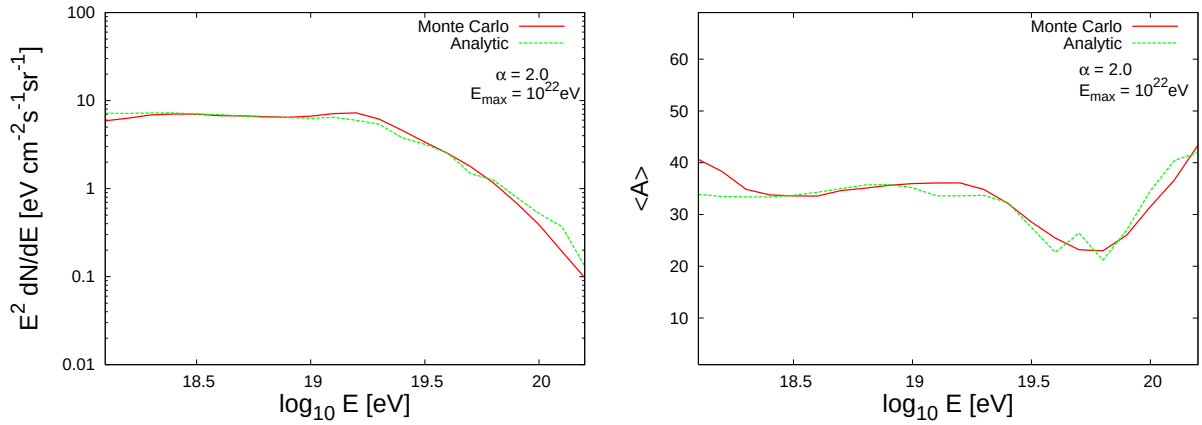

Figure 3.7: A comparison between the analytic values obtained for the cosmic ray spectrum and arriving composition, compared with the Monte Carlo results of Chapter 2.

3.8 Summary

The solution to a simplified form of the coupled differential equations relating the populations of the nuclear states, which only considers single nucleon loss, was found. The results produced by this solution are shown to give reasonable agreement with Monte Carlo simulation results (see Fig. 3.1 and Fig. 3.2). Through a further consideration of the general solution to the full set of coupled differential equations for the system, an improvement on the first analytic result was obtained. The results produced by it are shown to give better agreement with the Monte Carlo results (see Fig. 3.3 and Fig. 3.4). Through its application to Iron nuclei propagation, the solution was used in to determine the cosmic ray spectrum arriving from a uniform distribution of sources, each with an energy spectrum of α=2, along with the average composition of this flux, and the results compared with those of the previous Chapter (see Fig. 3.7).

Chapter 4

High Energy Neutrino Production due to CR Propagation

Ultra-high energy neutrinos are produced as a result of energy loss interactions of UHECRs with matter and radiation fields. In the following section the energy loss interactions of CRs as they propagate, from their source to Earth, will be considered.

As ultra-high energy ($> 10^{18}$ eV) CRs propagate, they lose energy through interactions with background photons. As discussed in Chapter 2, the background photon fields consist predominantly of the cosmic microwave background (CMB) and the cosmic infra-red background (CIB), each having an energy density of $\sim$1 eV cm^{-3}. These two dominant backgrounds are shown in Fig. 2.4, where the uncertainty in the CIB and its implications for the propagation of CRs are discussed.

4.1 Cosmic Ray Proton Interactions

On propagating from the source, two important energy loss processes of CR protons exist. The first of these being pair production in which the proton interacts with one of the background photons producing electron-positron pairs,

$$p \ + \ \gamma \ \rightarrow \ p \ + \ e^{+} \ + \ e^{-}. \tag{4.1}$$

The cross-section for this process is described by σ_T (the Thompson cross-section). The

energy loss rate for this process, is given by (6),

$$\frac{dE}{dx} = \frac{3}{8\pi}\alpha\sigma_T Z^2 (m_e c^2)^2 \int_2^\infty \frac{n(\epsilon)}{\epsilon^2} \int_2^\epsilon E dk \int_1^{k-1} dE A(k,E), \tag{4.2}$$

where α is the electromagnetic fine structure constant, $n(\epsilon)$ is the differential photon number density in the observer's frame, ϵ is the photons energy in this frame, and $A(k,E)$ is a dimensionless function. The energy loss rate increases rapidly until 10^{19} eV, at which point it reaches its maximum. For the energy range under consideration here, 10^{19} - 10^{22} eV, this energy loss process may be treated as continuous, since in the center of mass frame the proton typically has an energy $\sim 10^{10}$-10^{13} eV, the loss of $\sim$1 MeV per interaction has little effect on the proton's energy.

The second energy loss process relevant for CR protons is pion production, in which the proton interacts with a background photon producing a pion,

$$p \ + \ \gamma \ \rightarrow \ p/n \ + \ \pi^0/\pi^+. \tag{4.3}$$

Since this process is described by the strong interaction, it's cross-section is difficult to calculate, though is known over a large energy range through measurements (5). Such measurements of the total cross-section, $\sigma_{p\gamma}$, include both the contribution to the cross-section from single and multi-pion production. As mentioned in other work, (25; 26), the total proton photon scattering cross-section may be divided into two energy regions, a lower energy single pion production region, and a higher energy multiple pion production region. In this work, this simple treatment of multiple pion production will also be employed.

The required photon threshold energy for pion production, in the center of mass frame (which lies close to the proton rest frame), is

$$\begin{aligned} E_\gamma^{th} &= \frac{1}{2}\left(m_p + m_\pi - \frac{m_p^2}{(m_p + m_\pi)}\right) \\ &\sim 130 \text{ MeV}, \end{aligned} \tag{4.4}$$

where m_p is the proton mass, and m_π is the pion mass. The CR proton must have a Lorentz factor of $\sim 10^{11}$ in order that a $\sim 10^{-3}$ eV CMB photon, which provide the dominant photon

target for the UHECR protons, has sufficient energy to initialise the process. Thus, this interaction only becomes important for protons with energies above $\sim 10^{20}$ eV. At these energies the energy loss rate increases dramatically, leading to what is now referred to as the GZK cutoff (7; 8), referring to the supression in the arriving spectrum at energies around $10^{19.6}$ eV, due to the turning on of pion production energy loss, which leads to a dramatic decrease in the proton's energy. Again, for the energy range under consideration here (10^{18} - 10^{22} eV), in the center of mass frame, the proton typically has an energy of 10^{9}-10^{12} eV. However, since the loss of $\sim$140 MeV per interaction here does have a significant effect on the proton's energy, the process must be treated stochastically.

With the measured cross-section for this process, the interaction length, L, may be determined using the relation (25),

$$L = 2\gamma^2\hbar^3\pi^2c^3\left[\int_{E'_{th}/2\gamma}^{\infty}\frac{n(E)}{E^2}\int_{E'_{th}}^{2\gamma E}dE'E'\sigma(E')\right]^{-1}, \tag{4.5}$$

where E'_{th} is the threshold energy for pion production in the proton's rest frame, and γ and $n(E)$ are the Lorentz factor of the proton and the differential photon number density, in the observer's frame.

The interaction lengths for these different high energy proton energy loss processes are shown in Fig. 4.1 below.

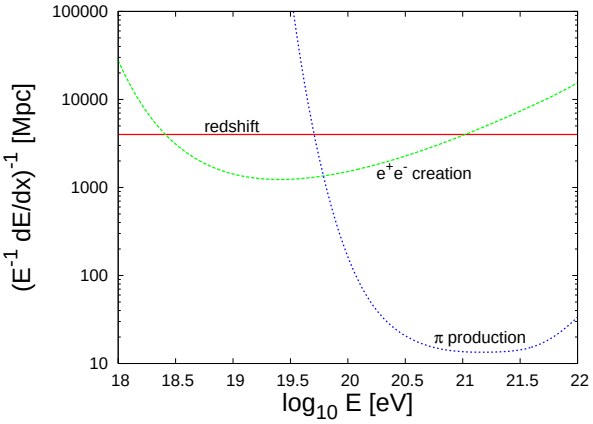

Figure 4.1: The interaction lengths for a high energy proton propagating through the CMB radiation field. Pair creation (4.1), pion production (4.3), and energy loss through cosmological expansion are all shown

4.2 Cosmic Ray Nuclei Interactions

For ultra high energy nuclei, the dominant energy loss process is photo-disintegration, in which the nuclei interacts with a background photon causing it to fragment into a lighter nuclei and fragmentary particles,

$$N(A,Z) \ + \ \gamma \ \rightarrow \ N'(A',Z') \ + \ m\alpha \ + \ ((Z-Z')-2m)p \ + \ (A-A'-(Z-Z')-2m)n. \quad (4.6)$$

As for pion production, the cross-sections for this process must be measured as the interaction is described in terms of strong and electromagnetic processes. The actual cross-sections have only been measured for a handful of nuclear species (9). However the cross-sections for all the important isotopes under consideration here were parameterised with a Gaussian plus a constant fit in (10). The "Gaussian" fit cross-sections used here are were found to give a sufficiently accurate description for photo-disintegration in Chapter 2.

4.3 Cosmogenic Neutrino Production

For the case where the UHECRs are protons, the main source of neutrinos during propagation is through the decay charged pion generated in photo-pion production interactions, and the subsequent decay of the pion,

$$\pi^+ \ \rightarrow \ \mu^+ \ + \nu_\mu \ \rightarrow \ e^+ \ + \ \nu_e \ + \ \bar{\nu}_\mu \ + \ \nu_\mu, \quad (4.7)$$

since the neutrino in pion decay takes ∼5% of the proton's energy, this process produces neutrinos with energies just below 10^{18} eV. Accompanying charged pion production is the neutron generation process (shown in interaction (4.3)). The free neutrons produced, with a free lifetime dictated by the weak interaction, decay with a mean lifetime of ∼886 s (11) through the process

$$n \ \rightarrow \ p \ + \ e^- \ + \ \bar{\nu}_e. \quad (4.8)$$

Since the neutrinos produced here only take 0.01% of the neutron's energy, this process leads to the production of $\sim 10^{15}$ eV neutrinos. Free neutrons are also produced in photo-disintegration reactions shown in (4.6). As a result of the fact that the neutron takes a fraction $\frac{1}{A}$ of the parent

nuclei's energy (where A is the atomic mass number), for the present study which considers the energy range of 10^{19} - 10^{22} eV cosmic rays, the neutrinos produced from photo-dissociated neutrons have energies $\sim 10^{14}$ - 10^{15} eV.

To calculate the cosmogenic neutrino flux, the distribution in population of the particles involved, both energetically and spatially, must be chosen. In order to allow a comparison of these result with previous similar calculations (12; 13; 14), the usual popular parameterised distributions have been used (15). The first of these, the energy distribution of the CRs at source, is motivated by the results of Fermi shock acceleration (22),

$$\frac{dN}{dE} \propto E^{-2} \exp\left(\frac{-E}{10^{21.5}\text{ eV}}\right). \tag{4.9}$$

The spatial distribution of the CR sources assumed will be that given by the expression (2.1).

With these energetic and spatial distributions for the CR sources, along with the CR interaction processes highlighted in (4.1) and (4.3), and the subsequent neutrino generating processes show in (4.7) and (4.8), the anticipated cosmogenic neutrino flux produced from ultra-high energy CR proton propagation have been calculated. Due to the stochastic nature of the pion production interactions, a Monte Carlo simulation of the process was used.

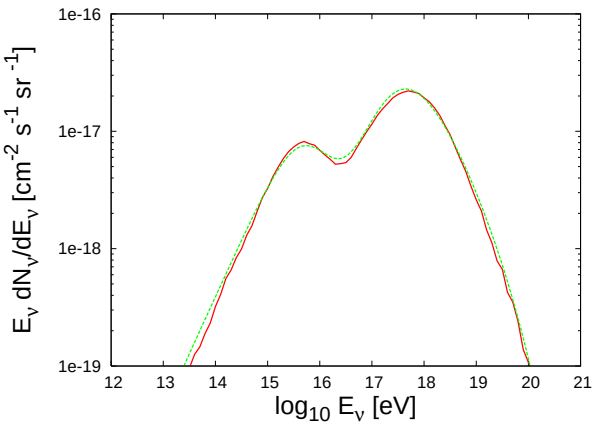

Figure 4.2: The cosmogenic neutrino flux produced due to ultra high energy cosmic ray proton propagation. The solid curve shows the Monte Carlo result and the dotted curve shows a previous result (16) for comparison.

The result shown in Fig. 4.2, finds reasonable agreement with previous calculations of the

anticipated cosmogenic neutrino spectrum, for ultra-high energy CR protons. The two peaks in the neutrino spectrum occurring at the anticipated energies of 10^{15} eV and 10^{18} eV, and in the approximate ratio 1:3, as expected for the single and triple neutrino production processes (4.8) and (4.7).

The equivalent cosmogentic neutrino flux for high energy heavy nuclei CRs has also been calculated in a similar manner to that for CR protons, except with the further inclusion of the photo-disintegration process described by (4.6).

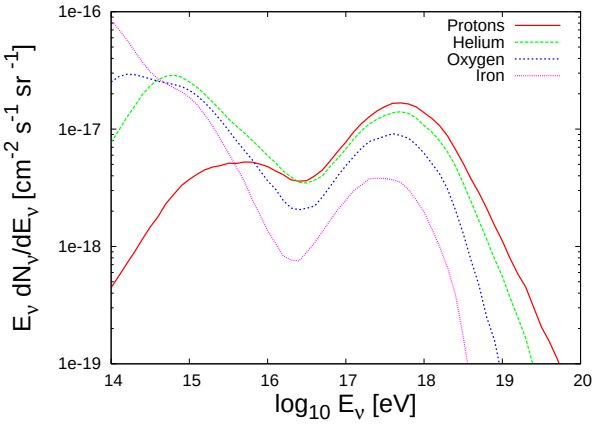

Figure 4.3: The cosmogenic neutrino flux produced due to ultra-high heavy nuclei CR propagation- ^{4}He, ^{16}O, and ^{56}Fe, for comparison the result for protons from a previous calculation (16) is also shown.

The results for the cosmogenic neutrino flux produced by ultra-high energy heavy nuclei propagation are shown in Fig. 4.3. As for the case of the cosmogenic neutrino flux produced by high energy protons, high energy heavy nuclei are also seen to lead to the production of two peaks in their subsequent neutrino flux. However, for heavy nuclei an extra contribution to the neutrino flux exists from fragmentary neutrons produced as a byproduct of the photo-disintegration process. The lower energy neutron peak may be significantly larger than in the ultra-high energy proton case as a result of this.

However, following the results of Chapter 2, the amount of photo-disintegration undergone by a heavy nucleus, as it propagates through space, is dependent on the CIB. As seen in Fig. 2.4, a large amount of uncertainty is currently present in our knowledge of the CIB, resulting in subsequent uncertainty in the photo-disintegration rate of the heavy nuclei as they propagate

and the arrival spectrum expected at Earth. This dependence of the arrival CR spectrum on the CIB is discussed in Chapter 2, for the current calculation the CIB proposed in (17) is used.

Since the fragmentary protons and neutrons carry approximately the same Lorentz factor as the parent nuclei, their energy is smaller than the parent nuclei by a factor of the parent nuclei mass number, A. This leads to considerably fewer pions being produced through CR nuclei propagation and consequently significantly fewer pion generated neutrinos existing in the the higher energy peak.

4.4 Cosmogenic Neutrino Fluxes

The cosmogenic neutrino fluxes, produced through the propagation of protons, Helium, Oxygen, and Iron nuclei are all shown above in Fig. 4.3. The neutrino fluxes in this section were normalised by matching the arriving CR spectrum at an energy of $10^{19.5}$ eV with a value between the two spectra observed by the two experiments with the largest exposure in this energy range, AGASA and HiRes [1].

As anticipated, the higher energy pion generated cosmogenic neutrino flux peak, observed in Fig. 4.3, is seen to decrease as the atomic number of the heavy nuclei species is increased, due to the reduced population of high energy protons able to undergo the pion generating interaction described by (4.3). Also observed in this figure is the expected increase in the lower energy neutron generated cosmogenic neutrino flux peak, a result of the increased number of neutrons produced through fragmentation interactions described by (4.6).

These results are expected to be considerably different if either the energy distribution of the CRs, or the spatial distribution of their sources, are different from those assumed here, given by (4.9) and (2.1). More specifically, a dominant cosmologically local source would be expected to reduce the overall cosmogenic neutrino flux, since interaction distances of >Mpc are required for both photo-disintegration and pion generation to occur.

The sensitivity of the cosmogenic neutrino flux to the energy distribution is a little more complicated. Firstly, the steepness of the CR energy spectrum would clearly result in a smaller population of CR protons above the threshold energy for pion production, and subsequently

[1] The Auger experiment now also has an exposure comparable to that of these two experiments

fewer pion production interactions occurring as the CRs propagated from source to Earth. Since the normalisation energy of the cosmogenic neutrino flux, sits just below the threshold energy for pion generation ($\sim 10^{19.6}$ eV), the flux value used for normalisation is mostly insensitive to the the population of protons above threshold, resulting in this first effect leading to an overall decrease in the pion generated cosmogenic neutrino peak. This result is clearly highlighted in Fig. 4.4, which demonstrates the decrease in pion generated neutrinos as a result of steepening the spectral index (from $\alpha = 2.0$ to $\alpha = 2.4$).

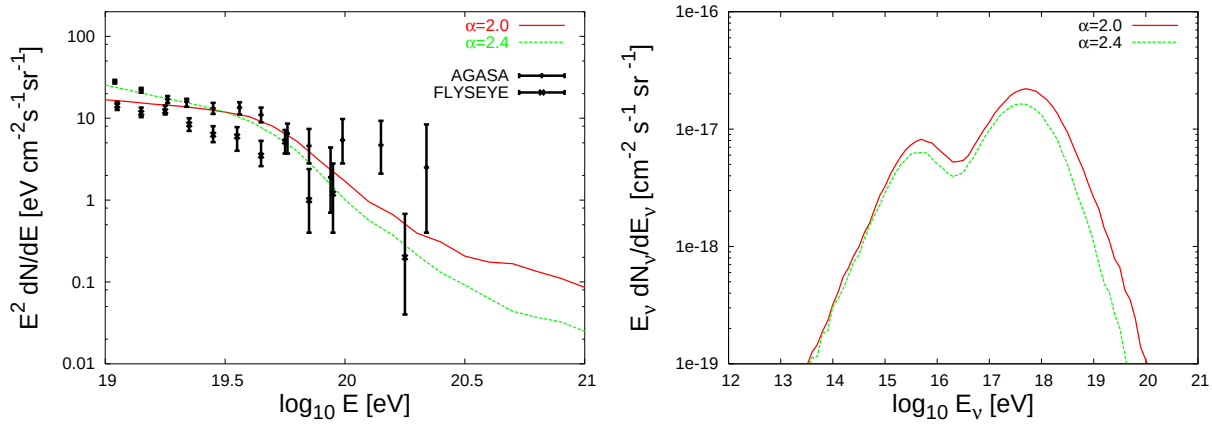

Figure 4.4: The ultra high energy proton and neutrino spectrum arriving at Earth due to ultra-high energy proton propagation, for energy spectral indices of 2.0 and 2.4

Secondly, a steeper heavy nuclei CR spectrum would also reduce the population of heavy nuclei with energies above the threshold energy for photo-disintegration ($\sim 10^{19.3}$ eV for Iron, though this threshold energy is lower for lighter nuclei) leading to fewer neutrons being produced from photo-disintegration. However, since the cosmogenic neutrino flux normalisation depends upon the heavy nuclei CR flux at energies well above the threshold energy for photo-disintegration to occur, the decrease in the neutron population due to a steeper spectrum is compensated by the decrease in heavy nuclei CRs at the normalisation energy, removed from this energy through photo-disintegration interactions. This results in the lower energy neutron generated cosmogenic neutrino flux peak remaining predominantly unchanged in value.

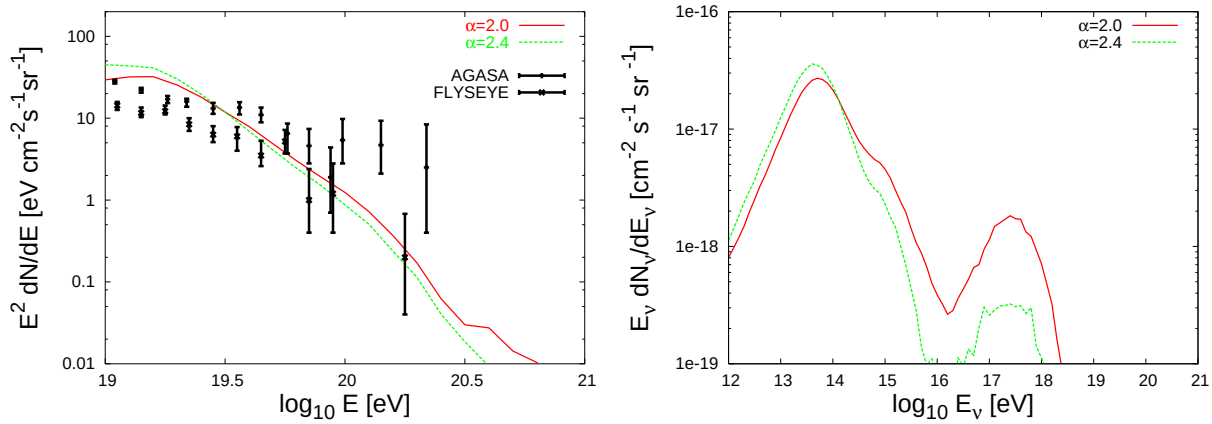

Figure 4.5: The ultra high energy cosmic ray spectrum and cosmogenic neutrino flux arriving at Earth due to Iron nuclei propagation, for spectral indices of 2.0 and 2.4

A similar lack of change in the neutron generated neutrino peak is observed when the cutoff energy chosen for the CR spectrum is altered, the origin of this invariance being the same as the neutron peak's invariance to a change of spectral index previously described. As shown in equation (4.9), an exponential cutoff has been used at the high end of the CR spectrum, with a cutoff energy of $10^{21.5}$ eV. However, increasing this cutoff energy by an order of magnitude to $10^{22.5}$ eV, is found to boost the flux of the pion generated peak by a factor of 3. This, once again, results from an increase in the CR proton population above the threshold energy for pion production, with the CR spectrum, at the normalisation energy, remaining unchanged. In Fig. 4.6, shown below, this increase in the pion generated neutrino peak, due to the higher energy cutoff, is observed.

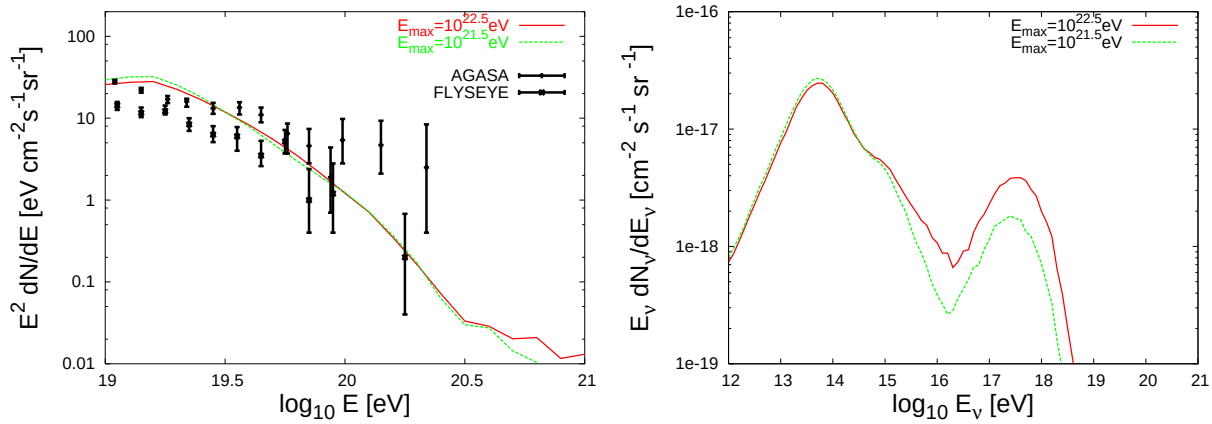

Figure 4.6: The ultra high energy cosmic ray spectrum and cosmogenic neutrino flux produced by the propagation of Iron nuclei with a particular cutoff energy- the cutoff values of $10^{21.5}$ eV and $10^{22.5}$ eV have been used here

4.5 Future Neutrino Telescope Observations

With the first generation of kilometer scale neutrino telescopes, such as IceCube/AMANDA (100), presently either under construction or built, it seems likely that the first observations of ultra-high energy neutrinos will be soon forthcoming. The IceCube experiment, presently under construction at the South Pole, will be capable of observing muon neutrinos indirectly by observing the light produced by high energy (10^{11} - 10^{18} eV) muons as they pass through the detector. IceCube is also sensitive to shower events produced in the detector.

High energy muons are generated in charged current interactions between the muon neutrino and a quark in the ice,

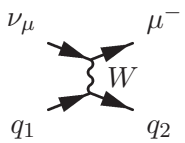

Since the muon has a $\sim \mu$s lifetime, the muons produced in the ice will predominantly leave the detector, producing only Cherenkov light as they do so, such events are here referred to as muon events.

High energy electrons and tauons, whose creation has an associated hadronic shower and

which go on to produce an electromagnetic shower observable in the detector [2], are also produced through similar charged current interactions to that depicted in the Feynman diagram 4.5, as well as in neutral current interactions like that represented by the Feynman diagram below,

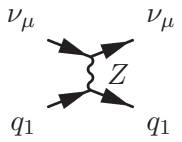

Since all of these events produce a shower in the detector, they are referred to here collectively as shower events.

Both the muon and shower rates expected for the IceCube experiment are shown in Table 4.1. A detection rate of about 1 ultra-high energy neutrino per year is calculated to be expected from CR proton interactions with background radiation fields, in the case of proton primaries with an $\alpha = 2.0$ injection spectrum, and an isotropic distribution of sources. This makes it unrealistic to expect IceCube (or Auger, which has a similar detection rate) to measure the cosmogenic neutrino flux in detail, though only a small number are required for detection due to the low levels of background expected in the ultra-high energy range.

The Auger experiment, though designed to observe ultra-high energy ($>10^{18.5}$ eV) CRs, is also anticipated to to have some sensitivity to the ultra-high energy neutrino flux, with signature events identified through the observation of "deeply penetrating, quasi-horizontal showers" (19) and Earth-skimming, upwards going showers, produced by tau-neutrinos (18).

[2]The tau neutrinos has two possible signature events referred to as either a "double bang" or "lolly pop" event (21)

Table 4.1: The number of cosmogenic neutrinos to be detected per year by the full IceCube array

Primary	Shower (E^{thr}= 1PeV)	Muon (E_{μ}^{thr} = 1PeV)
Protons (A=1)	0.57	0.72
Helium (A=4)	0.42	0.50
Oxygen (A=16)	0.19	0.23
Iron (A=56)	0.036	0.042

From the Table it is also clear that should a significant fraction of the UHECRs be heavy nuclei, the expected cosmogenic neutrino flux rates for IceCube are greatly reduced, making its detection barely possible, leading to new detection techniques being required. Such an improvement may well call upon the detection of the radio signals that accompany the electromagnetic shower (78; 20).

4.6 Summary

The cosmogenic neutrino flux produced by the propagation of ultra high energy cosmic ray protons through the CMB radiation field is determined through the application of a Monte Carlo simulation, with the results shown to give good agreement with those obtained by previous authors (see Fig. 4.2). This flux's dependence on the ultra high energy cosmic ray composition is determined through obtaining equivalent fluxes for a range of cosmic ray species (see Fig. 4.3). The higher energy peak of the flux, produced by the decay of pions produced through photo-meson production interactions, is shown to decrease by an order of magnitude over the range of cosmic ray composition considered. The dependence of cosmogenic neutrino flux upon the ultra high energy cosmic ray spectral index for the cases of proton and nuclei cosmic rays is highlighted (see Fig. 4.4 and Fig. 4.5). A significant decrease in the higher energy (pion generated) peak is found to be expected over a reasonable range of the spectral index, α, though the lower energy (neutron generated) peak is fairly invariant over the range. Similarly, the dependence of the higher energy peak on the position of the energy cutoff of is addressed (see Fig. 4.6). The origin of both effects on the height of the pion generated peak lying in the size

of the proton population above the pion production threshold energy at distances sufficiently far away from Earth to undergo pion production interactions (see Fig. 4.1).

Chapter 5

Cosmic Ray Energy Loss in the Source

Cosmic ray energy loss is also expected to occur within the CR source, in the region where CR acceleration is occurring. Such energy loss processes could be due to either CR interactions with the surrounding mass in the region, through hadron hadron interactions, or through interactions with the radiation field in the region. In this chapter only the second of these energy loss processes will be considered, this being a reasonable assumption since the cross section for proton proton collisions, σ_{pp}, and the cross section for proton photon collisions, $\sigma_{p\gamma}$ are $\sim 4\times10^{-28}\mathrm{cm}^{-2}$ and $\sim 5\times10^{-28}\mathrm{cm}^{-2}$, and the target photon density, n_γ in these regions are expected to be much larger than the target proton density, n_p.

In this Chapter, three possible sources of UHECR will be considered: active galactic nuclei (AGN); gamma ray bursts (GRBs); starburst regions. The total luminosity from such regions being comparable to that required for UHECR sources ($\sim 10^{45}$, 10^{51}, and 10^{46} erg s^{-1} respectively), which require a power output of 10^{44} erg Mpc^{-3} yr^{-1} (101) to sustain the CR population above 10^{19} eV (assuming the UHECR flux observed at Earth presently to be typical).

For the sources considered here, the luminosity and accelerating region size are approximately $\lesssim$1 pion production length for CR protons with energies $<10^{16}$ eV interacting with photons within them.These sources are therefore nearly always "optically thin" to protons leaving the source. Hidden neutrino sources, that are "optically thick" to CR protons, mentioned

in (15), produce much larger neutrino fluxes than those expected under the assumption that only a small fraction of the CR's energy is lost within the source. In this work predominantly "optically thin" neutrino sources will be considered. The reader should note that both the AGN and GRB models considered involve relativistic kinematics, for which primed quantities in this Chapter will denote the value as measured in the source's rest frame.

The optical depth, $\tau_{\gamma\gamma}$, defined by (52),

$$\tau_{\gamma\gamma} = R'/l_{e^+e^-}(E'_\gamma), \tag{5.1}$$

where R' is the size of the source in its rest frame (for the GRB and AGN models this can be significantly different to the observers frame), and $l_{e^+e^-}(E'_\gamma)$ is the pair creation length for a photon of energy E'_γ in the source), and the fraction of the proton energy deposited in the source f_π, defined by,

$$f_\pi = R'/l_\pi^{att.}(E'_p), \tag{5.2}$$

where $l_\pi^{att.}(E'_p)$ is the attenuation length for a proton of energy E'_p in the source due to pion production. The optical depth, $\tau_{\gamma\gamma}$, and f_π are clearly related through the respective interaction lengths with the radiation field in the source.

5.1 AGN as UHECR Sources

The radiation field chosen here will be motivated by observations of the photon energy spectrum of BL Lac objects. Such objects are thought to be the direct observation, along the beam axis, of an AGN, ie. an observation along the jet, as shown in Fig. 5.1.

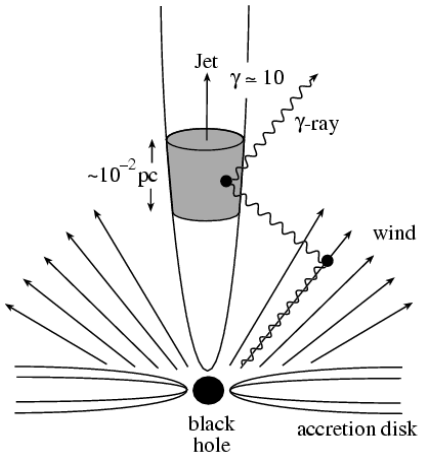

Figure 5.1: A diagram highlighting the AGN kinematics, (80)

In the AGN model used here, the CR acceleration process is assumed to occur within a relativistic blob of plasma moving along the jet, with a Lorentz factor of $\sim 10^{1.5}$, with the flaring process assumed to occur for $\Delta t \approx 10^4$ s in the lab frame. The plasma, in its rest frame, is considered spherical with radius $c\Delta t'$ ($=\Gamma c \Delta t$).

A constraint on the Lorentz factor, Γ, of the relativistic blob comes from the requirement that the blob be optically thin to the γ-rays passing through it ($\tau_{\gamma\gamma} < 1$). The pair creation length $l_{\gamma\gamma}(E_\gamma)$ is given by (52),

$$l_{\gamma\gamma}(E'_\gamma) = \frac{16}{\sigma_T} \frac{(m_e c^2)^2}{U'_\gamma E'_\gamma}, \tag{5.3}$$

where m_e is the mass of the electron and U'_γ is the radiation field's energy density in the blob's frame of reference. Since this distance is shortest for the highest energy photon produced by the source, and the typical photon seen in the radiation field has energy E_{γ_peak}, the threshold for pair creation for the highest energy photon is,

$$4E'_\gamma E'_{\gamma\_peak} = (m_e c^2)^2. \tag{5.4}$$

Boosting back to the laboratory frame, this leads to the constraint on Γ of,

$$\Gamma^2 > \frac{4E_\gamma E_{\gamma\_peak}}{(m_e c^2)^2}. \tag{5.5}$$

For the flaring AGN model considered below, with Γ=$10^{1.5}$, the condition for the photon energies involved to be below that required for pair creation is easily satisfied (for E_γ=10^{13} eV, Γ >0.5). A Lorentz factor of the order $10^{1.5}$ is also motivated by observations of relativistic blobs of plasma present in AGN jets.

The shape of the spectra for this type of blazar is well described by a lower energy synchrotron self-Compton peak, and a higher energy inverse Compton peak. However, since the energy loss of CRs in the energy range 10^{16} - 10^{20} eV, with Lorentz factors 10^7 - 10^{11}, only the lower energy photons (10^{-6} - 10^2 eV) in the synchrotron peak are relevant here, since these, to the proton, are Lorentz boosted to the MeV and GeV energies required for pion production and photo-disintegration (it should also be noted that the inverse Compton photon target is significantly smaller than the synchrotron population).

Motivated by the energy spectra of BL Lacs such as PKS 0528+134 (49), the spectrum used here approximately fits a broken power law of the form,

$$\begin{aligned} \frac{dN_\gamma}{dE_\gamma} &\propto E_\gamma^{\frac{1}{2}} \text{ for } E_\gamma < 10^{-3} \text{ eV} \\ &\propto E_\gamma^{-2.3} \text{ for } E_\gamma > 1\ 10^{-3} \text{ eV}. \end{aligned} \tag{5.6}$$

The radiation field present in the particle acceleration region of the AGN, described above in (5.6), is shown below in Fig. 5.2 expressed as $E_\gamma dN_\gamma/dE_\gamma$ (or $E\ n(E)$ using the notation of Chapter 2),

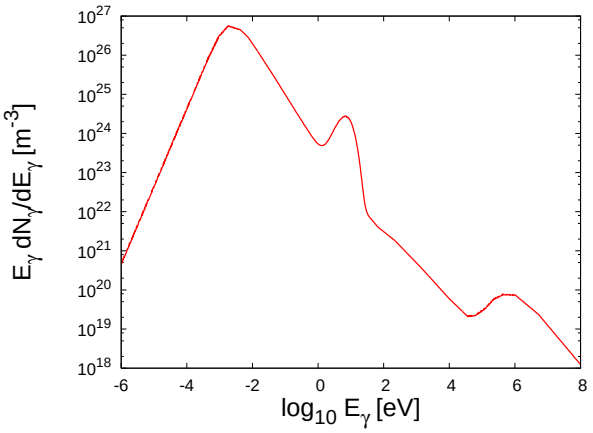

Figure 5.2: The photon spectrum, in the acceleration region of the AGN, assumed in this work

Such a radiation field exhibits a triple peaked structure, though only the lower two peaks are of relevance here. The lowest energy peak originates from synchrotron radiation produced by a population of high energy electrons with an energy spectrum $dN_e/dE_e \propto E_e^{-1.6}$ in the presence of a magnetic field. Below the spectral break at $\sim 10^{-3}$ eV, the source is optically thick to the synchrotron radiated photons, being subsequently reabsorbed by other electrons in the region and changing the emitted photon energy spectrum from the source. Above the spectral break, the source is optically thin and synchrotron emitted photons escape the source without being reabsorbed, with their spectral index remembering the spectral index of the emitting electron population. The second peak's origin is the emission of a 20 000 K blackbody, radiated by the accretion disk. The normalisation of these peaks is described by the typical parameterisation for the partition of the Eddington luminosity, $L_{\rm Edd}$, going into these two components, with 10% radiated as blackbody and 1% going into synchrotron emission.

From a consideration of the luminosity, L_γ, and duration of flare, Δt, a fiducial value for the energy density, U_γ, injected into a spherical blob of radius $c\Delta t$ is,

$$\begin{aligned} U_\gamma &= \frac{L_\gamma \Delta t}{\frac{4\pi}{3}(c\Delta t)^3} \\ &\approx 6 \times 10^{24} \left(\frac{L}{10^{45}\ \mathrm{erg\ s^{-1}}}\right)\left(\frac{\Delta t}{10^4\ \mathrm{s}}\right)^2\ \mathrm{eV\ m^{-3}}. \end{aligned} \tag{5.7}$$

However, through a consideration of the relativistic setup, this is changed somewhat,

$$\begin{aligned} U'_\gamma &= \frac{L'_\gamma \Delta t'}{\frac{4}{3}(c\Delta t')^3} \\ &= \frac{L_\gamma \Delta t}{\frac{4}{3}\Gamma(c\Gamma\Delta t)^3} \text{ since } L'_\gamma \Delta t' = L_\gamma \Delta t/\Gamma \\ &= \frac{1}{\Gamma^4} U_\gamma. \end{aligned} \tag{5.8}$$

Thus, the fact that the blob is relativistic leads to a dilution of the energy density within it.

The fraction of CR energy expected to be lost within the acceleration region, f_π, through pion production is, $f_\pi(E'_p) \approx \frac{R'}{l_\pi^{att.}(E'_p)}$, where $l_\pi^{att.}(E'_p)$ is the attenuation length of the proton with energy E'_p, through its interaction with the radiation field. The attenuation length is

given by,

$$l_{\pi}^{att.}(E'_p) = \frac{E'_{\gamma\_peak}}{K_p(E'_p)U'_{\gamma}\sigma_{\Delta}} \tag{5.9}$$

$$= \frac{\Gamma^4 E'_{\gamma\_peak}}{K_p(E'_p)U_{\gamma}\sigma_{\Delta}}, \tag{5.10}$$

where $K_p(E'_p)$ describes the inelasticity of the collision and σ_{Δ} is the Δ resonance cross section, giving,

$$f_{\pi}(E'_p) \approx \frac{c\Delta t'}{l_{\pi}^{att.}(E'_p)} \tag{5.11}$$

$$= \left(\frac{3K_p(E'_p)}{4\pi\Gamma^3}\right)\left(\frac{L_{\gamma}\Delta t}{E'_{\gamma\_peak}}\right)\left(\frac{\sigma_{\Delta}}{(c\Delta t)^2}\right). \tag{5.12}$$

For protons interacting with photons of energy E'_{γ_peak} through the Δ resonance (for which $K_p \approx 0.2$), f_{π} is maximum, with value,

$$f_{\pi}^{\max} \approx \left(\frac{3\times 0.2}{4\pi\Gamma^2}\right)\left(\frac{L_{\gamma}\Delta t}{E_{\gamma\_peak}}\right)\left(\frac{\sigma_{\Delta}}{(c\Delta t)^2}\right)$$

$$= 553\left(\frac{10^{1.5}}{\Gamma}\right)^2\left(\frac{L_{\gamma}}{10^{45}\ \mathrm{erg\ s^{-1}}}\right)\left(3\times\frac{10^{-3}\ \mathrm{eV}}{E_{\gamma\_peak}}\right)\left(\frac{10^4\ \mathrm{s}}{\Delta t}\right). \tag{5.13}$$

Since, a proton of energy E'_p interacting with a photon of energy E'_{γ}, through the delta resonance,

$$E'_p = \frac{(m_{\Delta}c^2)^2 - (m_p c^2)^2}{4E'_{\gamma}}, \tag{5.14}$$

(where m_{Δ} is the mass of the Δ resonance (1232 MeV), and m_p is the mass of the proton), the AGN source therefore is thick to $p\,\gamma$ interactions for 10^{22} eV protons (E_p) interacting with 3×10^{-3} eV photons (E_{γ}). From Fig. 5.7, the radiation field is seen to become thick to such interactions at an energy of 10^{20} eV.

5.2 GRBs as Ultra High Energy Cosmic Ray Sources

In many ways this source has similarities to the emitted blob of plasma considered in the AGN model. A change of geometry and scales, however, needs to be made. In the fireball's comoving frame, a spherical shock expands relativistically in all directions, with a Lorentz factor Γ. In a rest frame moving with Lorentz factor Γ towards the observer, the shock has thickness R/Γ, where R is the initial size of the compact object before the fireball phase. In the observers frame, the shock is further compressed into a thin shell of thickness R/Γ^2 (see (91) for a derivation of these relationships).

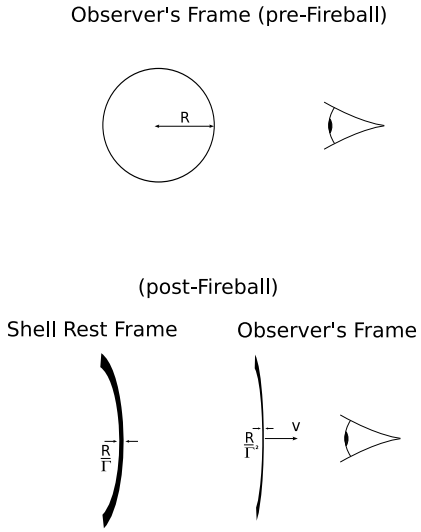

Figure 5.3: A diagram highlighting the GRB Kinematics

For the GRB model employed here, the size of the accelerating region R is set by the duration of the ms structures observed in the arriving spectra from GRBs (93), observed in the lab frame.

As for the AGN scenario, a constraint on the GRB Lorentz factor, Γ, of the expanding fireball may be obtained through the requirement that the GRB also be optically thin to the observed γ-rays passing through it. From the relation of (5.5), it is required that $\Gamma > 20$ (with $E_{\gamma\_peak}=10^6$ eV and $E_\gamma=10^8$ eV) for the photons in the region to have energies below the threshold for pair creation (though a large amount of uncertainty for the range of E_γ for GRBs

presently exists, and it seems feasible for photons with energies $E_\gamma > 10^{11}$ eV, able to pair produce, to exist in the accelerating region). From observations, (51), a Lorentz factor $\sim 10^{2.5}$ is found to be typical for GRBs.

The radiation field for the GRB assumed here, is that chosen by previous authors who have carried out similar analysis (51; 52), ie. a broken power law spectrum of the form,

$$\begin{aligned} \frac{dN_\gamma}{dE_\gamma} &\propto E_\gamma^{-1} \text{ for } E_\gamma < 1 \text{ MeV} \\ &\propto E_\gamma^{-2} \text{ for } E_\gamma > 1 \text{ MeV}. \end{aligned} \tag{5.15}$$

This model being noted to fit well the γ-ray data observed in the BATSE catalogue (82).

Such a radiation field present in the GRB acceleration region, described above in (5.15), is shown below in Fig. 5.4 expressed as $E\ dN/dE$,

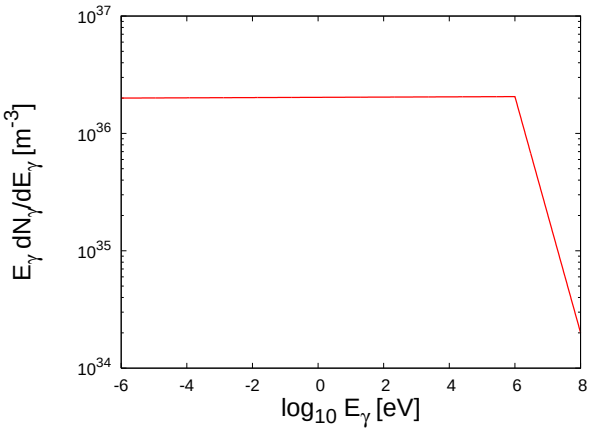

Figure 5.4: The photon energy spectrum in GRB accelerating region

The origin of such a radiation field is still a matter of debate, with some authors considering it being due to synchrotron emission of shocked electrons within the expanding fireball. A discussion on the origin of the GRB's energy spectrum is given in (83).

The fiducial value for the energy density, U'_γ, of a shell of luminosity, L'_γ, radius R', and

thickness R'/Γ is,

$$U'_\gamma = \frac{L'_\gamma \Delta t'}{\frac{4\pi}{\Gamma} R'^3} \tag{5.16}$$

$$= \frac{L_\gamma \Delta t}{\Gamma^6 4\pi (c\Delta t)^3} \text{ since } R'/\Gamma^2 = c\Delta t \tag{5.17}$$

$$= 2 \times 10^{27} \left(\frac{10^{2.5}}{\Gamma}\right)^6 \left(\frac{L_\gamma}{10^{51} \text{ erg s}^{-1}}\right) \left(\frac{10^{-3} \text{ s}}{\Delta t}\right)^2 \text{ eV m}^{-3}. \tag{5.18}$$

With the use of equations (5.9) and (5.2), the fraction of energy deposited in the GRB by a CR of energy E'_p is,

$$f_\pi(E'_p) \approx \left(\frac{K_p(E'_p)}{4\pi\Gamma^5}\right) \left(\frac{L_\gamma \Delta t}{E'_{\gamma\_peak}}\right) \left(\frac{\sigma_\Delta}{(c\Delta t)^2}\right), \tag{5.19}$$

which for protons interacting with the peak of the photon spectrum through the Δ resonance gives,

$$f_\pi^{\max} \approx \left(\frac{0.2}{4\pi\Gamma^4}\right) \left(\frac{L_\gamma \Delta t}{E_{\gamma\_peak}}\right) \left(\frac{\sigma_\Delta}{(c\Delta t)^2}\right) \tag{5.20}$$

$$= 0.55 \left(\frac{10^{2.5}}{\Gamma}\right)^4 \left(\frac{L_\gamma}{10^{51} \text{ erg s}^{-1}}\right) \left(\frac{1 \text{ MeV}}{E_{\gamma\_peak}}\right) \left(\frac{10^{-3} \text{ s}}{\Delta t}\right). \tag{5.21}$$

This result highlights that, under the assumptions made here, GRBs are expected to be thin to $p\,\gamma$ interactions, with a proton at most undergoing 1 pion production interaction before leaving the source region. Using equation (5.14), the source is thickest to protons with energies above $1.4{\times}10^{16}$eV (E_p).

5.3 Starburst Galaxies as Ultra High Energy Cosmic Ray Sources

The radiation field chosen here is motivated by observations of the nuclei of local ultra luminous infra-red Galaxies, NGC 6240 and Arp 220 (84), as well as the nuclei of the starburst Galaxy NGC253. The Galactic center region (roughly the central 100 pc) of the Starburst Galaxy consisting of a predominant population, $N_{\rm OB}$, of hot (40 000 K) O type stars and a smaller population of cooler (4 000 K) red supergiant stars (86), providing the region with optical and UV ($\sim$10 eV) starlight. In total, a population of 27 000 stars is chosen for the region, as

used in previous studies (87). As discussed in (85), dust in the region, reprocesses a portion of the produced starlight, leading to the region also being bathed in IR ($\sim 10^{-2}$ eV) radiation. In order for the proportion of reprocessed radiation to match the observed SEDs from such regions, as shown Fig. 5 of (85), $\sim$90% of the starlight emitted must be re-radiated in the IR energy range. The model employed here constitutes to an elementary single component model, in which a clumpy dust shell surrounding the starburst region sits in thermal equilibrium with the starlight radiation, heated to a tempertature of 30 K. Though more complicated multi-component models, with differing opacities for each component would give a better agreement with the observed SEDs of starburst Galaxies, the model used here sufficiently explains the SEDs to justify its use, with higher order corrections to the model being of little bearing on the results obtained here.

The energy spectrum of the radiation within the starburst region is,

$$n(E_\gamma) = n^\star(E_\gamma) + n^{IR}(E_\gamma), \tag{5.22}$$

(note $n(E_\gamma)$=dN_γ/dE_γ). $n^\star(E_\gamma)$ and $n^{IR}(E_\gamma)$ given by,

$$n^\star(E_\gamma) = \frac{9}{4} \left[\frac{n^{\rm BE}_{T_{\rm OB}}(E_\gamma)\ N_{\rm OB}\, R^2_{\rm OB} + n^{\rm BE}_{T_{\rm SG}}(E_\gamma)\ N_{\rm SG}\ R^2_{\rm SG}}{R^2} \right] , \tag{5.23}$$

and

$$n^{IR}(E_\gamma) = 0.9 n^{\rm BE}_{T_{\rm IR}}, \tag{5.24}$$

$R_{\rm OB}$ being the radius of OB type stars, $R_{\rm SG}$ the radius of red supergiants, and R the radius of the starburst region ($\sim$100 pc). $n^{\rm BE}_T(E_\gamma)$ is the number density energy distribution for particles described by Bose-Einstein statistics, given by

$$n^{\rm BE}_T(E_\gamma) = (E_\gamma/\pi)^2 \left[e^{E_\gamma/kT} - 1 \right]^{-1} , \tag{5.25}$$

The attenuation length for a CR proton within the starburst radiation field is given by,

$$l^{att.}_\pi(E_p) = \frac{1}{K_p(E_p) n(E_\gamma) \sigma_\Delta}. \tag{5.26}$$

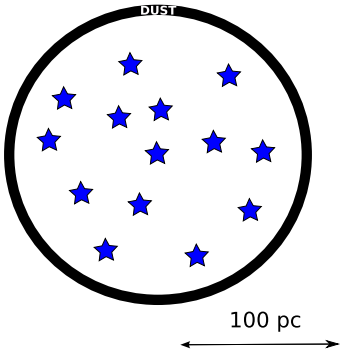

Figure 5.5: A Diagram Depicting a Starburst Region

Despite the starburst region only being ∼100 pc in size, CRs take longer than the 300 yrs or so that might be expected for relativistic particles since the particles will interact with the strong, 0.1 mG, magnetic fields in the region (88), their propagation is diffusion limited. The diffusion time out of such a region, with a Kolmogorov type power spectrum of the magnetic field energy density on different scales, such that the diffusion coefficient, D, has an energy dependence of the form, $D \propto E^{-\frac{1}{3}}$, is described by,

$$\tau_{Diff.} = 400\ Z \left(\frac{E}{5 \times 10^{15}\text{eV}} \right)^{-1/3} \text{yrs}, \tag{5.27}$$

where E is the energy of the diffusing particle with charge Z.

Using equations (5.26 and 5.27), the fraction of energy deposited in the starburst region through CR pion production interactions with the radiation field is,

$$f_\pi(E_p) \quad = \quad c\tau_{Diff.}(E_p) K_p(E_p) E_\gamma n(E_\gamma) \sigma_\Delta, \tag{5.28}$$

which for the assumption that protons interact through the Δ resonance gives,

$$f_\pi^{\max} \approx 4 \times 10^{-4}. \tag{5.29}$$

The radiation field present in the nuclei of the starburst region described above, is shown in Fig. 5.6.

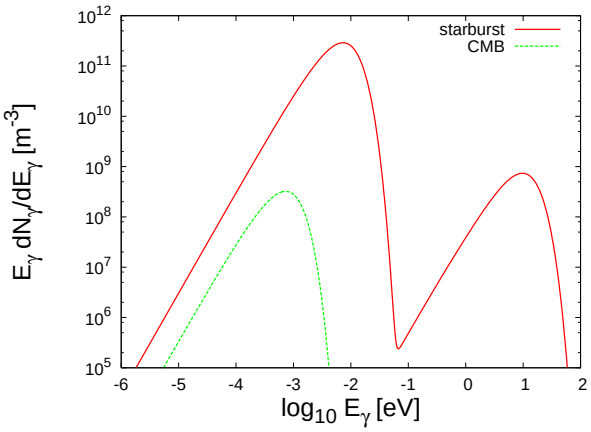

Figure 5.6: The photon energy spectrum in the starburst accelerating region

5.4 Interactions Within Ultra High Energy Cosmic Ray Source Models

With the source size ($c\Delta t'$), the interactions rates of CR protons and nuclei with the radiation field described by Fig.s 5.2,5.4, and 5.6, leading to energy loss through pion production for CR protons, and photo-disintegration for CR nuclei, propagating through such a radiation field, found through the application of equation (4.5), are given below in Fig. 5.7,

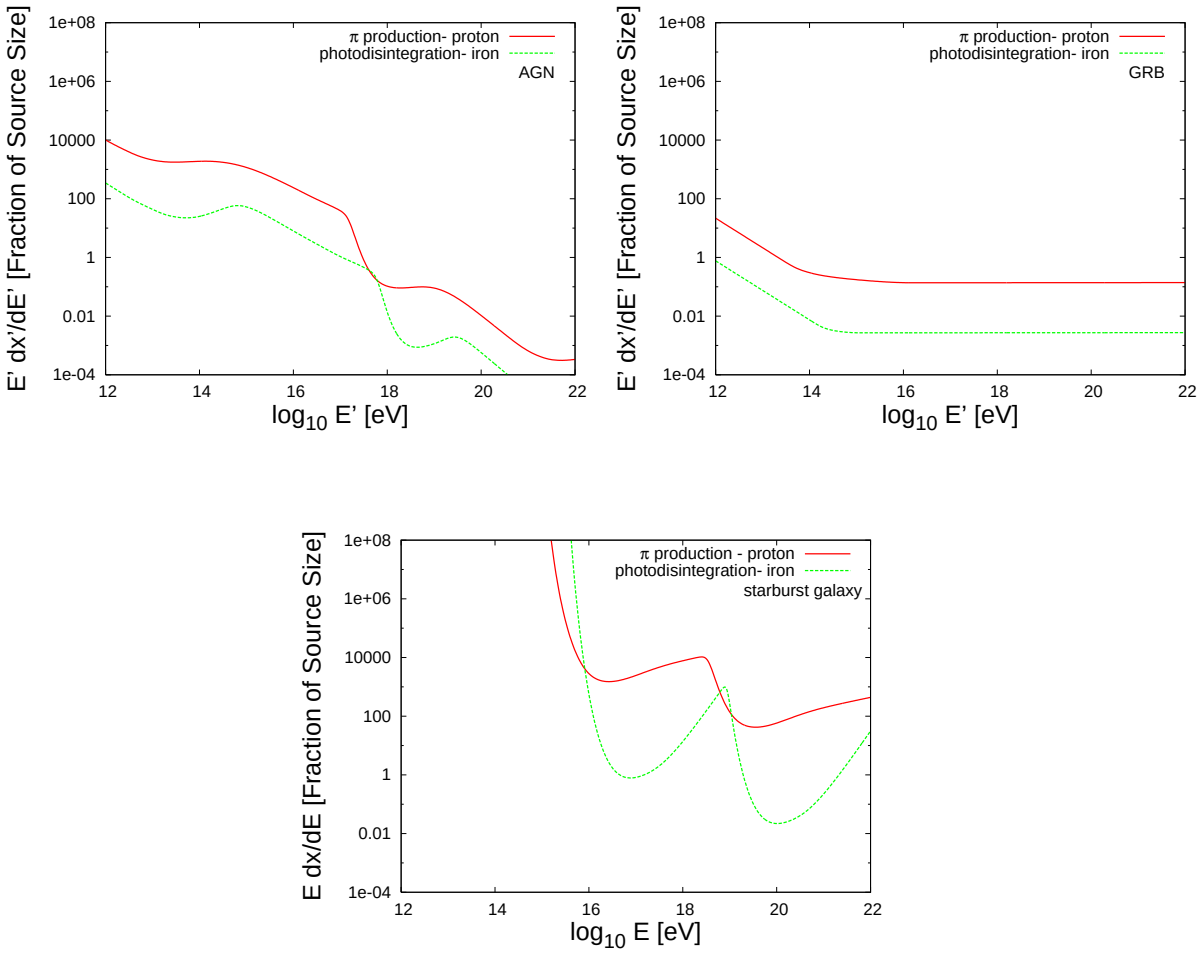

Figure 5.7: Pion production and photo-disintegration lengths for protons and nuclei propagating through the radiation fields present in the acceleration region of AGN, GRBs, and starburst regions

For nuclei propagating through such a radiation field, the degree of photo-disintegration experienced will vary with the energy of the nuclei, due to the energy dependence of the interaction rates shown above in Fig. 5.7. For AGN, it is seen that nuclei with energies greater than approximately $10^{18.5}$ eV (in the lab frame) are expected to interact at least once with the radiation field before departing the source region. The results for AGN and GRBs both ignore the effect that magnetic fields in the source region will have on increasing the containment time of the CR within them. Though such effects will undoubtedly play a role in increasing the number of interactions a CR has before leaving the source region, the work here will only consider containment time effects for the starburst regions where magnetic field strengths are sufficiently well known. For the GRB and AGN results, however, it should be noted that such

a containment time affect would be expected to increase with Z, the charge of the CR nuclei, and for lower energy CRs more easily deflected by such fields.

The number of dissociated nucleons produced is shown below in Fig 5.8, showing that total dissociation of a nuclei, accelerated by the emitted plasma in the AGN jet, would occur for energies $>10^{19}$ eV.

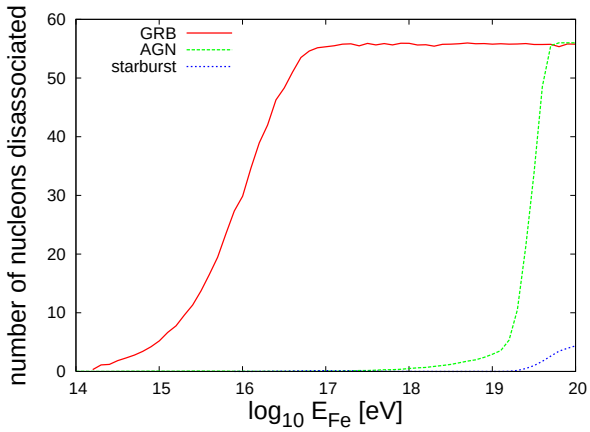

Figure 5.8: Degree of dissociation, of an Iron nuclei, before departing the source region for the three cases considered of AGN, GRBs, and starburst galaxies as high energy cosmic ray sources

The protons produced through photo-disintegration interactions of nuclei, may go on to produce neutrinos through pion production interactions, whilst still within the source region. The subsequent neutrino spectrum produced for the AGN and GRBs are given below. However, since starburst regions are so thin to even photo-disintegration interactions, no appreciable neutrino flux is produced from these sources.

The normalisation of the flux follows the argument that these objects are the sources of CRs with energies above 10^{19}eV. From measurements of the CR flux with these energies, $E_{CR}^2 dN_{CR}/dE_{CR}$=20 eV cm^{-2} s^{-1} sr^{-1} (corresponding to a power output of the sources of, $E_{CR}^2 d\dot{N}_{CR}/dE_{CR}\Big|_{10^{19}\ \mathrm{eV}}$=$10^{44}$erg Mpc^{-3} yr^{-1}, (101)). An estimation of the neutrino flux for the different sources is (80),

For AGN,

$$E_\nu^2 \frac{dN_\nu}{dE_\nu}\bigg|_{5\times10^{20}\ \mathrm{eV}} = (1-\exp(-f_\pi^{\max}))\, t_H\ E_{CR}^2 \frac{d\dot{N}_{CR}}{dE_{CR}}\bigg|_{1.0\times10^{22}\ \mathrm{eV}} \tag{5.30}$$

$$\approx 20\ \mathrm{eV\ cm^{-2}\ s^{-1}\ sr^{-1}}, \tag{5.31}$$

where t_H is the Hubble time (since neutrinos can propagate cosmological distances).

For GRBs, which we assume produce CRs with energies above 10^{16} eV for this calculation, (noting that the power output of the CR source is only logarithmically sensitive to the lower energy cutoff),

$$E_\nu^2 \frac{dN_\nu}{dE_\nu}\bigg|_{7\times10^{14}\ \mathrm{eV}} = (1-\exp(-f_\pi^{\max}))\, t_H\ E_{CR}^2 \frac{d\dot{N}_{CR}}{dE_{CR}}\bigg|_{1.4\times10^{16}\ \mathrm{eV}} \tag{5.32}$$

$$= 8\ \mathrm{eV\ cm^{-2}\ s^{-1}\ sr^{-1}}. \tag{5.33}$$

These values agree with the actual values for the neutrino fluxes obtained, which are shown below in Fig. 5.9. The decrease in neutrino spectrum produced by GRBs for $E_\nu > 10^{16}$ eV is a result of the pions generated synchrotron radiating in the large magnetic fields present before decaying. The energy dependence of this process, given in equation (1.10) (though here for pions rather than electrons), resulting in the energy loss time being,

$$\tau'_\pi = \frac{3(m_\pi c^2)^2}{4\sigma_T (m_e c^2)^2 c E_\pi U'_B}. \tag{5.34}$$

Since the energy loss time has a $1/E_\pi$ dependence and the pion lifetime depends on E_π, a $1/E_\pi^2$ cutoff in the neutrino spectrum is produced.

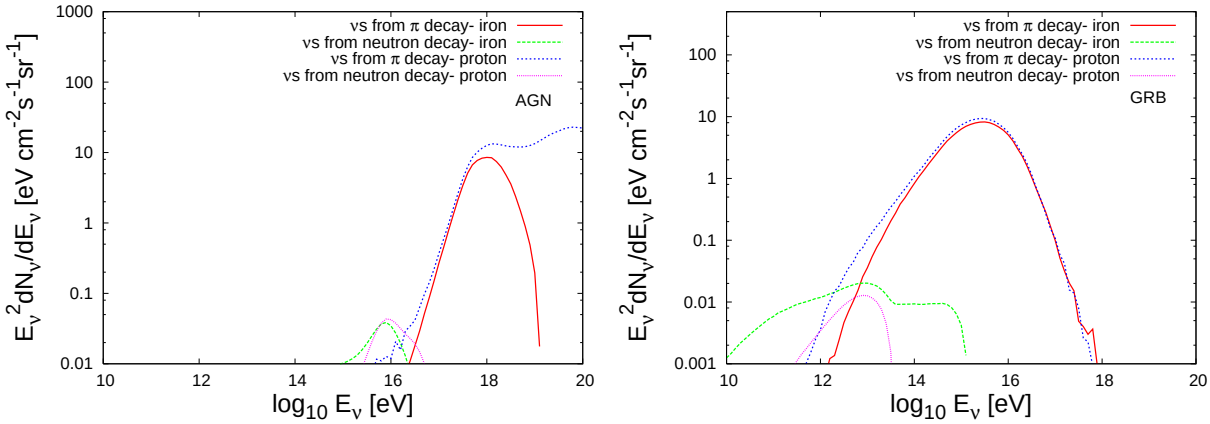

Figure 5.9: Neutrino fluxes produced by cosmic ray interactions in AGN and GRB sources

The cosmological neutrino fluxes produced by both the AGN and GRB sources shown in Fig. 5.9, both peak with values close to the Waxman-Bahcall upper bound (15), a result of the large $f_\pi^{\max}$ values for the regions. However, as their detection by neutrino telescopes depends on the flux of neutrinos, the detection rate for AGN is smaller than for GRBs, by the ratio of the energies at which they peak.

5.5 Justification for Ignoring Nuclei Pion Production

Pion production through an interaction of photons with the protons within nuclei directly may also occur (90), though has been ignored throughout this work. To justify neglecting such processes their interaction rates are shown below in Fig. 5.10. As can be seen from this figure, such pion production mechanisms are, for nearly all energy ranges, within the source models considered, highly subdominant.

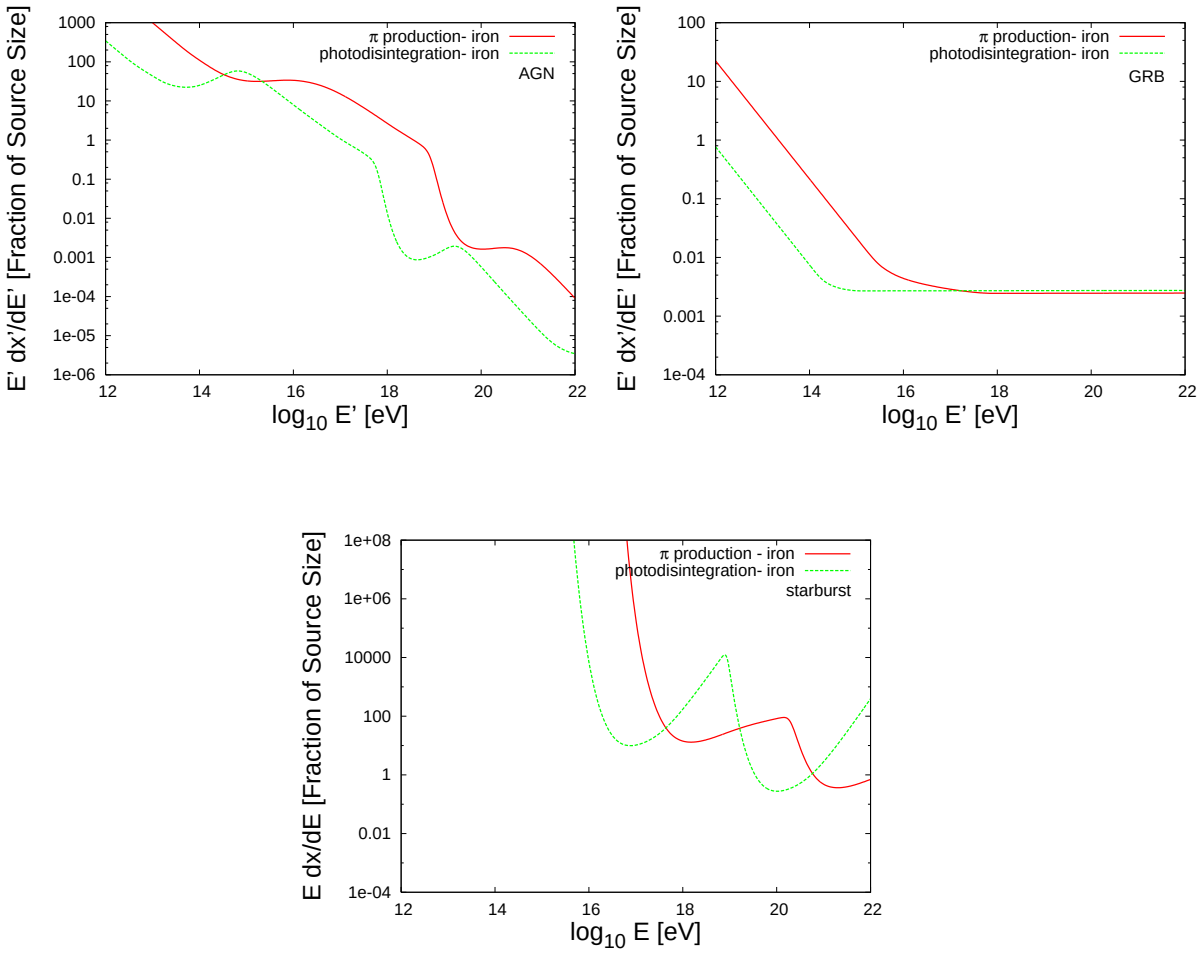

Figure 5.10: A comparison of the pion production and photo-disintegration interaction rates for Iron nuclei with the radiation field within AGN, GRBs, and starburst galaxies.

The GRB plot in Fig. 5.10, however, does indicate that pion production from nuclei and photo-disintegration rates do compete for nuclei energies (in the plasma frame) $>10^{17}$ eV. However, in this region only 1% of pions produced will decay before losing a significant amount of their energy to synchrotron radiation, allowing such processes to be safely neglected. It will also be noted that in starburst galaxies, the two processes compete around energies of 10^{21} eV. However, as can be seen from a consideration of the Hillas criterion, starburst galaxies are not expected to be producers of such high energy nuclei, so once again the competition between the rates may be safely neglected.

5.6 Relative Rates of Pion Production and Photo-disintegration

Since, for the example radiation fields considered so far for AGN, GRBs, and starburst Galaxies, it has been found to be the case that sources of high neutrino flux, also lead to near total photo-disintegration of nuclei, perhaps a suitable question to ask is are all sources in which pion production occurs also likely to lead to total photo-disintegration?

To answer this question, the calculation of the pion production and photo-disintegration rates, given by equations (4.5) (though with different cross sections and threshold energies for the processes), need to be considered.

From the plot comparing the cross sections for the pion production and photo-disintegration processes below in Fig. 5.11, it seems likely that the photo-disintegration process will occur more frequently than the pion production process, for protons and Iron nuclei being exposed to uniform radiation field, $E_\gamma dN_\gamma/dE_\gamma = constant$, though the width of the resonances must also be taken into account.

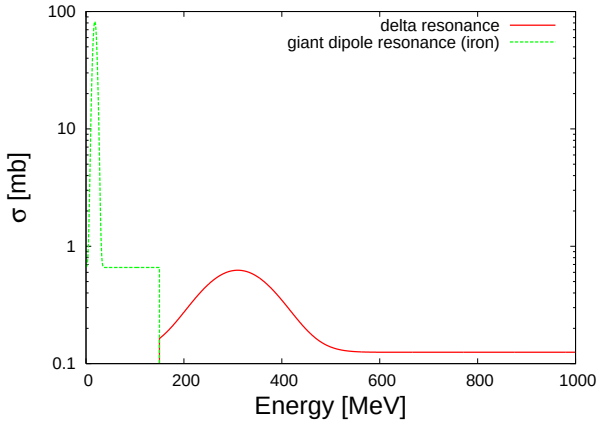

Figure 5.11: The cross sections for the interaction of an Iron nucleus with a photon ($N(A_{56}, Z_{26}) + \gamma$) and a proton with a photon ($p + \gamma$).

$$R = \frac{1}{2\Gamma^2} \int_{E_{th}/2\Gamma}^{\infty} \frac{n(E)}{E^2} dE \int_{E_{th}}^{2\Gamma E} E' \sigma(E') dE'. \tag{5.35}$$

For photo-disintegration-

$$R_{A,\gamma}(\Gamma) = \frac{1}{2\Gamma^2}\int_{E_{th}/2\Gamma}^{\infty}\frac{n(E)}{E^2}dE\int_{E_{th}}^{2\Gamma E}E'\sigma(E')dE'. \tag{5.36}$$

Approximating $\sigma(E')$ by $\sigma_{A,\gamma}$ over the range $E_{A,\gamma}\pm\Delta_{A,\gamma}$.

$$\begin{aligned} R_{A,\gamma}(\Gamma) &= \frac{\sigma_{A,\gamma}}{2\Gamma^2}\int_{\frac{E_{A,\gamma}-\Delta_{A,\gamma}}{2\Gamma}}^{\frac{E_{A,\gamma}+\Delta_{A,\gamma}}{2\Gamma}}\frac{n(E)}{E^2}dE\int_{E_{th}}^{2\Gamma E}E'dE' & (5.37)\\ &= \frac{\sigma_{A,\gamma}}{4\Gamma^2}\int_{\frac{E_{A,\gamma}-\Delta_{A,\gamma}}{2\Gamma}}^{\frac{E_{A,\gamma}+\Delta_{A,\gamma}}{2\Gamma}}n(E)\frac{4\Gamma^2E^2-E_{th}^2}{E^2}dE, & (5.38)\end{aligned}$$

(assuming $E_{th}\ll E_{A,\gamma}-\Delta_{A,\gamma}$)

$$R_{A,\gamma}(\Gamma) = \sigma_{A,\gamma}\int_{\frac{E_{A,\gamma}-\Delta_{A,\gamma}}{2\Gamma}}^{\frac{E_{A,\gamma}+\Delta_{A,\gamma}}{2\Gamma}}n(E)dE. \tag{5.39}$$

Similarly for pion production-

$$R_{p,\gamma}(\Gamma) = \sigma_{p,\gamma}\int_{\frac{E_{p,\gamma}-\Delta_{p,\gamma}}{2\Gamma}}^{\frac{E_{p,\gamma}+\Delta_{p,\gamma}}{2\Gamma}}n(E)dE. \tag{5.40}$$

Since $E_{A_{56},\gamma}$=18 MeV, and $\Delta_{A_{56},\gamma}$=8 MeV, and $E_{p,\gamma}$=310 MeV, and $\Delta_{p,\gamma}$=100 MeV, the approximate relation,

$$\begin{aligned} R_{A_{56},\gamma}(\Gamma) &\approx \frac{\sigma_{A_{56},\gamma}}{\sigma_{p,\gamma}}R_{p,\gamma}(15\Gamma) & (5.41)\\ &= 160R_{p,\gamma}(15\Gamma), & (5.42)\end{aligned}$$

(with $\sigma_{A_{56},\gamma}$=81 mb and $\sigma_{p,\gamma}$=0.5 mb)

This result has been compared for the three radiation fields considered in Fig. 5.12 below. For these plots, the photo-disintegration rates have been shifted according to the relation (5.42). As can be seen in these figures, the result gives very good agreement for all three radiation fields.

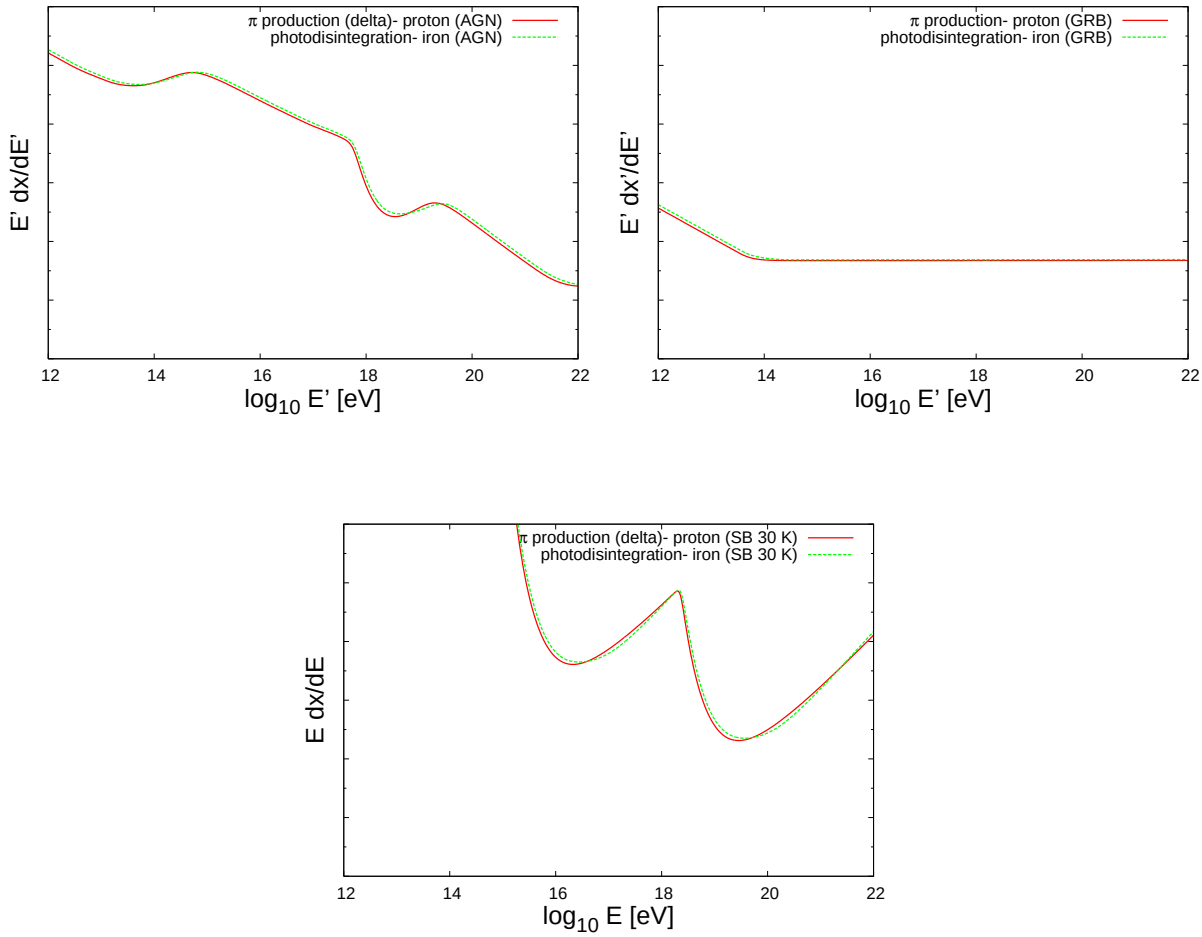

Figure 5.12: A comparison of the pion production (through the Δ resonance) and photo-disintegration rate in the AGN, GRB, and starburst radiation fields. The photo-disintegration rates have been modified to produce the pion production rates using equation (5.42), and compared with the actual pion production rate values.

5.7 Summary

Three models of possible CR source regions are described: AGN; GRBs; starburst galaxies. The radiation fields present in the regions and constraints on the kinematics from observational data are determined, and the calculation for the factor $f_\pi^{\max}$, which ultimately determines the amount of power output a source puts into neutrinos, is gone through for each of the cases. The values $f_\pi^{\max}$ arrived at indicate that both AGN and GRBs, should they be UHECR sources, may be expected to produce significant fluxes of high energy neutrinos (see Fig. 5.9). A justification for the ignoring of direct pion production by nuclei is given, showing that the

interaction rates for photo-disintegration are always dominant over this process for all relevant energies considered (see Fig. 5.10). An approximate relationship between the pion production and photo-disintegration rates is found, indicating that regions in which pion production is expected will also lead to complete disintegration of nuclei, and regions transparent to high energy nuclei, will not be producers of high energy neutrino fluxes.

Chapter 6

Conclusion

Chapter 2 looks into the disintegration of nuclei in the CMB and CIB radiations fields. Analysis of the photo-disintegration rates for the propagating nuclei focused on the parameterisation of the photo-disintegration cross-sections, with a comparison of the Gaussian type parameterisation previously used in this field with a new "Lorentzian" parameterisation which is found to give improved fits to the photo-disintegration data available. Also investigated was the consequence that the uncertainty in the CIB had on the interaction rates of both UHECR nuclei and protons, along with the subsequent uncertainty this leads to in the the calculated CR spectrum and composition arriving at Earth. The effects of weak intergalactic magnetic fields on the propagation of UHECR, for different compositions were investigated, with the subsequent arriving CR spectrum, for different strength fields, obtained.

Though the Lorentzian models, as stated previously (9), give notably better agreement with the photo-disintegration data available, the disagreement between the subsequent interaction rates of the two parameterisations is less notable, and the corresponding differences in the arriving CR spectrum at Earth even less so. Similarly, the variation in the models of the CIB considered lead to a few % difference in the CR spectrum observed at Earth for the case of CR Iron nuclei. The presence of weak nG intergalactic magnetic fields, with coherence lengths of the order of 1 Mpc, was found to lead to a flattening of the low energy end (near 10^{19} eV) of the CR spectrum where such fields have the largest effect.

Chapter 3 develops an analytic treatment of the disintegration of nuclei, building on the results found in Chapter 2, that the consideration of only a single decay route path, with

Gaussian type cross sections to describe the giant dipole resonance, was sufficient to adequately describe the decay of heavy nuclei to lighter nuclei as they propagate. With this simplification, a simple solution to the chain of differential equations, describing the photo-disintegration of nuclei, was found. A further improvement on the analytical model was achieved through a consideration of the full differential equation describing the states of the system, in which multi-nucleon loss from a nuclei is possible.

Reasonable agreement was found with the first attempt at an analytic solution, though increasing disagreement was found, between the Monte Carlo and analytic results, as the distribution functions of lighter and lighter nuclei were considered, as anticipated. The improvement on the analytic approach obtained through the use of effective decay lengths reduced this disagreement, providing a far better fit to the Monte Carlo results.

In Chapter 4, the production of cosmogenic neutrinos due to UHECR propagation through the CMB and CIB radiation fields have been considered. The interaction rates for UHE protons with these radiation fields were discussed, with the uncertainty in these rates and the CIB being highlighted (as earlier investigated in Chapter 2). This was further developed through a consideration of UHECR nuclei propagation, with the further uncertainties in the nuclei photon cross-sections being highlighted (as earlier investigated in Chapter 2). The calculation of the neutrino flux for both proton and nuclei CRs was carried out, with an explanation of the differences in the produced neutrino spectra produced by the propagation of different CR compositions. The dependence of the cosmogenic neutrino spectrum on the energy spectrum, for a specific CR composition, spectral energy index, and cutoff energy used was addressed.

The dependence of the cosmogenic neutrino spectrum on the CR composition found in this study, showing that proton UHECRs lead to a larger high energy ($\sim 10^{18}$eV) cosmogenic neutrino flux, and subsequently heavier nuclei producing smaller and smaller fluxes in this energy region. The cosmogenic neutrino flux produced through UHECR propagation was found to be highly sensitive, in particular, to the source's CR energy spectrum. A flatter spectrum and a higher energy cutoff giving the largest, pion generated, neutrino peak, and conversely a steeper spectrum with a lower energy cutoff giving the smallest peak.

Chapter 5 considers the possibility of CR energy loss within the source region for AGN,

GRB, and starburst regions. The radiation fields within such regions were considered, and the subsequent interaction rates for protons and nuclei with the radiation calculated. Simple kinematic models for the sources considered were outlined, allowing the approximate size of the source region to be determined, a result that plays a vital role in the determination of the neutrino flux. For the three source models considered, the degree of photo-disintegration undergone by Iron nuclei before leaving the source was calculated and the neutrino flux predominantly generated through proton interactions with the radiation field, was obtained for the case of Iron nuclei CR.

Both AGN and GRBs were found to have radiation fields sufficiently thick to p-γ interactions that a significant flux of neutrinos could be expected from the total cosmological population. In the case of AGN, Iron nuclei are found to be able to escape from the source for energies below 10^{19} eV. GRBs, however, are opaque to Iron nuclei, with total disintegration from the source region being expected. Contrary to both AGN and GRBs, Starburst regions are relatively transparent to the propagation of CR nuclei, with only a few nucleons being dissociated from an Iron nuclei at the highest energies. A comparison of the photo-dissociation and pion production rates reveals that sources with a radiation field strength sufficiently large to lead to complete disintegration of nuclei may produce a significant neutrino flux. Conversely, energy regions in which nuclei may escape before being photo-disintegrated are not producers of large neutrino fluxes.

Appendix A

A.1 Fermi Shock Acceleration (First Order)

Considering the case of a shock running through interstellar plasma, for the frame in which the upstream plasma is "stationary" (moves isotropically), the shock runs through the "stationary" plasma at velocity V, leaving behind it heated plasma of velocity $\frac{3}{4}V$ (for the case of a monatomic or ionised gas- see below).

A.1.1 Boundary Conditions at the Shock Front

At the shock front boundary, matter, momentum, and energy fluxes are all conserved (with velocities given in the rest frame of the shock),

$$\rho_1 V_1 = \rho_2 V_2 \tag{A.1}$$

$$p_1 + \rho_1 V_1^2 = p_2 + \rho_2 V_2^2 \tag{A.2}$$

$$\rho_1 V_1 w_1 + \frac{1}{2}\rho_1 V_1^3 = \rho_2 V_2 w_2 + \frac{1}{2}\rho_2 V_2^3, \tag{A.3}$$

where w_1 is the enthalpy per unit mass ($=\epsilon_m + \frac{p}{\rho}$, where ϵ_m is the internal energy per unit mass), for a perfect gas, w=$\frac{\gamma p}{(\gamma-1)\rho}$

- this comes from the definition of C_p and C_V, γ=C_p/C_V, for an ideal gas, γ=w/E=$(E+pV)/E$, giving E=$p/(\gamma$-1)ρ.

where γ is the ratio of the specific pressure to the specific volume (ie. $\frac{C_p}{C_V}$), p is the pressure, and ρ is the density.

So the three equations may be written,

$$\rho_1 V_1 = \rho_2 V_2 \tag{A.4}$$

$$p_1 + \rho_1 V_1^2 = p_2 + \rho_2 V_2^2 \tag{A.5}$$

$$\frac{\gamma}{(\gamma-1)} V_1 p_1 + \frac{1}{2}\rho_1 V_1^3 = \frac{\gamma}{(\gamma-1)} V_2 p_2 + \frac{1}{2}\rho_2 V_2^3. \tag{A.6}$$

From a rearrangement of the third equation and a substitution of the first,

$$\frac{\rho_1 V_1^2}{\rho_2} = \frac{2\gamma(p_1\rho_2 - p_2\rho_1)}{(\gamma-1)(\rho_1^2 - \rho_2^2)}. \tag{A.7}$$

Similarly, from a rearrangement of the second equation and a substitution of the first,

$$\frac{\rho_1 V_1^2}{\rho_2} = \frac{(p_2 - p_1)}{(\rho_2 - \rho_1)}. \tag{A.8}$$

Combining these two results,

$$2\gamma(p_1\rho_2 - p_2\rho_1) = (1-\gamma)(p_2 - p_1)(\rho_1 + \rho_2), \tag{A.9}$$

leading to the result,

$$\frac{\rho_2}{\rho_1} = \frac{(\gamma-1)p_1 + (\gamma+1)p_2}{(\gamma+1)p_1 + (\gamma-1)p_2}. \tag{A.10}$$

From this, if $p_2 \gg p_1$, then

$$\frac{\rho_2}{\rho_1} = \frac{(\gamma+1)}{(\gamma-1)}, \tag{A.11}$$

(the Mach number, M, is defined as $M{=}V/V_s$, where V_s is the velocity of sound in the plasma. $V_s{=}(\gamma \mathrm{p}/\rho)^{\frac{1}{2}}$, so $M{=}V(\rho/\gamma p)^{\frac{1}{2}}$.

From the substitution of equation A.1 into A.2, it is seen that,

$$\frac{p_2}{p_1} = (1 - \gamma M_1^2(\frac{\rho_1}{\rho_2} - 1)), \tag{A.12}$$

which from the result before gives,

$$\frac{p_2}{p_1} = (1 - \gamma M_1^2(\frac{(\gamma+1) + (\gamma-1)\frac{p_2}{p_1}}{(\gamma-1) + (\gamma+1)\frac{p_2}{p_1}} - 1)). \tag{A.13}$$

If $p_2 \gg p_1$, then

$$\frac{p_2}{p_1} \approx (1 - \gamma M_1^2(\frac{(\gamma-1)}{(\gamma+1)} - 1)) \tag{A.14}$$

$$\approx \frac{2\gamma M_1^2 + (\gamma+1)}{(\gamma-1)}. \tag{A.15}$$

For supersonic shocks, $M_1 \gg 1$, so,

$$\frac{p_2}{p_1} \approx \frac{2\gamma M_1^2}{(\gamma-1)}. \tag{A.16}$$

For a monatomic or ionised gas, $\gamma = \frac{5}{3}$, leading to $\frac{\rho_2}{\rho_1}$=4, which, from the mass conservation condition leads to $\frac{V_2}{V_1}$=$\frac{1}{4}$.

A.1.2 Particle Acceleration and Expected Energy Distribution

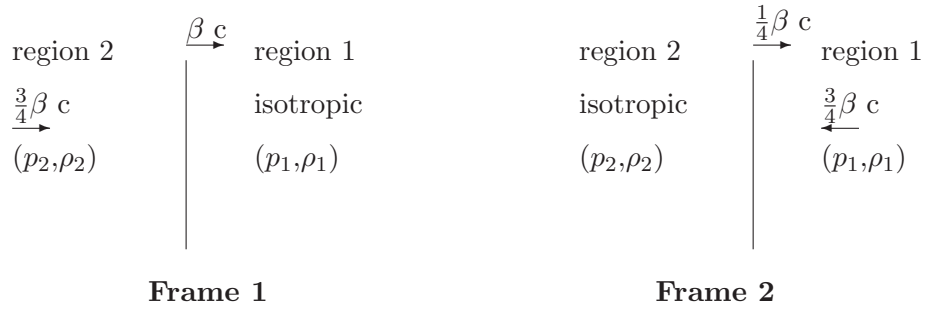

Figure A.1: A Diagram Showing the Shock Front in the 2 Frames of Reference

The ions in the plasma, on the compressed side of the shock have a thermal energies, a relic of the stellar life of the object previously, with temperatures $\sim 10^2$K ($\sim$0.1 eV), far less than the kinetic energy of the ions which are $\sim 5\times 10^3$eV. However, the ions in the shock post SN scatter off the magnetic field embedded in the plasma (flux freezing), since the mean free paths for collisions between ions in the plasma are much greater than the magnetic scattering lengths. Ions crossing the shock boundary, scattering off this magnetic field, become isotropised in the rest frame of the thermal plasma.

The injection of relativistic ions into the acceleration regime remains an unresolved problem for the acceleration mechanism.

Consider a relativistic ion of energy E in region 1 (which, when viewed such that the plasma moves isotropically, is viewed in frame 1), passing into region 2 (which, when viewed such that the plasma moves isotropically, is viewed in frame 2), which moves with velocity $\frac{3}{4}\beta c$, where c is the speed of light in a vacuum ($\beta \ll 1$, so $\gamma \sim 1$). The energy of the ion in rest frame 2, E', in terms of the quantities in rest frame 1, E and p, is,

$$E' = E\gamma(1 + \beta\cos\theta), \tag{A.17}$$

where θ is the angle the ion's momentum makes with the velocity vector of the Lorentz transformation, so the energy gained from the particle isotropising in region 1, to isotropising in region 2, is,

$$\frac{\Delta E}{E} \sim \beta, \tag{A.18}$$

(geometrical factor of $\frac{4}{3}$ comes in when you integrate over angles). The same result is obtained for crossings of the ions in the other direction (ie. from region 2 to region 1), since the a head on collsion is expected in this direction also (as shown in the diagram above), though particles are lost from the accelerator region for particles in region 2, since the shock moves away from the shocked plasma. When used along with the kinetic theory result that the flux of relativistic

ions goes as,

$$\frac{1}{4}Nc, \tag{A.19}$$

where N is the no. density of ions, the fraction of ions lost from the downstream region (the plasma's velocity from the shock, in the rest frame of the shock, being $\frac{1}{4}V$) during one crossing is,

$$\frac{\frac{1}{4}NV}{\frac{1}{4}Nc}, \tag{A.20}$$

so the fraction that remain in the accelerator per unit time are, $P \sim$ 1-β, which gives (using, ln(1+x)$\sim$x),

$$\ln P \sim -\beta. \tag{A.21}$$

If, for each collision, E'=$E\alpha$, and N'=NP, for n collisions, E'=$E(0)\alpha^n$, N'=$N(0)P^n$, so that,

$$\frac{\ln(E'/E(0))}{\ln(N'/N(0))} = \frac{\ln(\alpha)}{\ln(P)}. \tag{A.22}$$

Since, $\alpha \sim$1+β, $\ln(\alpha) \sim \beta$,

$$\frac{\ln(E'/E(0))}{\ln(N'/N(0))} \sim -1, \tag{A.23}$$

which leads to,

$$\frac{E'}{E(0)} \sim \frac{N(0)}{N'}, \tag{A.24}$$

so that,

$$\frac{dN}{dE} \sim E^{-2}. \tag{A.25}$$

For physical regions where this may occur- a similar process is known to occur in the bow shock of the Earth (with the solar wind meeting the magnetosphere) [Longair, volume 1], and there is now increasing evidence that such processes are accelerating hadrons in supernovae

remnants (SNRs) (89),where Radio and X-ray signals from synchrotron radiation, produced by the acceleration of electrons in magnetic fields, and Gamma-ray signals, from what is thought to be neutral pion decay, have been detected. However, from theoretical considerations, SNR may only accelerate CRs to at most $\sim Z{\times}10^{15}$eV, where Z is the charge of the CR, (54), which leaves the accelerating bodies of higher energy CRs (10^{17}eV) as a mystery.

Appendix B

The Monte Carlo technique allows particle interactions which are stochastic in nature, due to the large degree of inelasticity in them, to be implemented into the calculation of the expected resultant flux calculation from a distribution of sources, each with a particular flux.

The stochastic processes of relevance here are p γ interactions resulting in pion production and N γ collisions resulting in nucleon emission. In the following sections an outline of the Monte Carlo approach applied to proton and nuclei propagation through the background radiation field will be described.

The first part of the calculation requires the determination of the particle energy and distance (from Earth). The particle energy is selected with the use of the distribution function for the energy,

$$\frac{dN}{dE}(E) = E^{\alpha}\frac{dN}{dE}\bigg|_{E_{min}} E^{-\alpha}, \tag{B.1}$$

where E_{min} is the lowest energy particle considered, and α is the index describing the shape of the power law injection spectrum, and E is the particle energy. If E_{max} is the maximum energy particle considered, the energy of the particle may be chosen with a random number (random),

$$\int_{Emin}^{E} dE\frac{dN}{dE}(E) = random \times \int_{E_{min}}^{E_{max}} dE\frac{dN}{dE}. \tag{B.2}$$

Similarly, the value for the distance of the particle injected is selected from the source distri-

bution which is given by,

$$\frac{dN}{dV} \propto \begin{cases} (1+z)^3 & : z < 1.9 \\ (1+1.9)^3 & : 1.9 < z < 2.7 \\ (1+1.9)^3 e^{(2.7-z)/2.7} & : 2.7 < z < 8, \end{cases} \tag{B.3}$$

where z is the redshift of the source and V is the comoving volume being considered. However, since the volumes the particles are injected into are $\chi^2 c dt$, where χ is the comoving distance, c is the speed of light, and dt is a time interval (the source emits particles at a constant rate), and the number of particles from the source through unit area drops as $1/\chi^2$, the distribution of the sources with redshift is given by,

$$\frac{dN}{dz} = \frac{dN}{dV}\frac{dt}{dz}. \tag{B.4}$$

From the source distribution function, the redshift of the source emitting the particle in the Monte Carlo is selected with a random number (*random*), according to,

$$\int_0^z dz \frac{dN}{dz}(z) = random \times \int_0^{z_{max}} dz \frac{dN}{dz}, \tag{B.5}$$

where z_{max} is the maximum redshift at which particles are injected.

Once both the redshift and the energy of the particles have been selected, propagation commences.

B.1 Proton Propagation

For proton propagation, the pion interaction lengths, $L_{p\gamma}$, are those determined by equation (4.5), and the pair production energy loss rates are those determined by equation (4.2). It should be noted that these interaction lengths depend on redshift, since background photons in the past had higher energies and number densities. Through the propagation of the protons over distance steps of length, Δx, shorter than the energy loss lengths due to pair production

$(E\frac{dx}{dE})$, the condition for the proton interacting with a CMB or CIB photon is

$$L_{p\gamma} \times (-\log(random)) < \Delta x. \tag{B.6}$$

When pion production does occur, the decision as to the charge of the pion is selected through the relative sizes of the cross sections for the $\pi^+ n$ and $\pi^0 p$ final states, given in (13).

Following this, the inelasticity, K_p, of the process must also be decided. Above the threshold energy for single pion production, and below that for multiple pion production, from kinematic considerations the inelasticity of the process is,

$$K_p = \frac{1}{2}\frac{(m_\pi^2 + 2m_p E_n)}{(m_p^2 + 2m_p E_n)}, \tag{B.7}$$

where m_p is the mass of the proton, m_π is the mass of the pion, and E_n is the energy of the nucleon.

Above the threshold for multiple pion production, the inelasticity takes the parameterised form,

$$\log_{10} K_p = (0.4 \log_{10}\left(\frac{E_n}{\mathrm{eV}}\right) - 4.062), \tag{B.8}$$

up to a K_p of 0.9 where it plateaus.

Subsequent to the pion generation process, the fragmentation of the pion into 3 neutrinos and a positron results in the ν_μ taking about 20 %, and the $\bar{\nu}_\mu$ and the ν_e taking about 26 %, of the pion's energy.

B.2 Nuclei Propagation

During nuclei propagation, the stochastic process relevant is nucleon loss from the nucleus. Since this leads to the possibility of multi-nucleon loss, the cross-sections for all possible processes must be taken into account. As for the case of proton propagation, the nuclei are propagated over distance steps of Δx, defined to be much smaller than the pair production energy loss length.

During each step, the interaction lengths for each of the nucleon loss processes are compared.

Before comparison, however, their interaction lengths for are modified by a random number according to,

$$L_{N\gamma} \times (-\log(random)) \tag{B.9}$$

thus, the process with the shorted modified interaction length is chosen number nucleon process is chosen for the step.

Whether or not this process does occur is once again chosen with the requirement that the modified interaction length is shorted than the step length Δx.

When nucleon loss does occur, the change of the nuclei's energy is simply determined by the number of nucleons lost in the process, since each nucleon is assumed to have an equal fraction of the total nuclei's energy before nucleon loss occurs.

All particles (nuclei and protons) throughout their propagation lose energy continuously due electron/positron pair creation, along with the redshifting of their energies resulting from the expansion of the Universe.

Bibliography

[1] M. A. Lawrence, R. J. O. Reid and A. A. Watson, J. Phys. G **17**, 733 (1991).

[2] D. J. Bird *et al.*, Astrophys. J. **441**, 144 (1995).

[3] M. Takeda *et al.*, Phys. Rev. Lett. **81**, 1163 (1998) [arXiv:astro-ph/9807193].

[4] T. Abu-Zayyad *et al.* [High Resolution Fly's Eye Collaboration], Astropart. Phys. **23**, 157 (2005) [arXiv:astro-ph/0208301].

[5] The proton-photon cross section data used is found at: http://pdg.lbl.gov/∼sbl/gammap_total.dat

[6] G. Blumenthal, Phys. Rev. D **1**, 6 (1970).

[7] K. Greisen, Phys. Rev. Lett. **16**, 748 (1966).

[8] G. T. Zatsepin and V. A. Kuzmin, JETP Lett. **4**, 78 (1966) [Pisma Zh. Eksp. Teor. Fiz. **4**, 114 (1966)].

[9] E. Khan *et al.*, Astropart. Phys. **23** (2005) 191 [arXiv:astro-ph/0412109].

[10] J. L. Puget, F. W. Stecker and J. H. Bredekamp, Astrophys. J. **205**, 638 (1976).

[11] The neutron's life time used is found at: http://pdg.lbl.gov/2006/listings/s017.pdf

[12] A. Mucke, J. P. Rachen, R. Engel, R. J. Protheroe and T. Stanev, Publ. Astron. Soc. Austral. **16** (1999) 160 [arXiv:astro-ph/9808279].

[13] A. Mucke, R. Engel, J. P. Rachen, R. J. Protheroe and T. Stanev, Comput. Phys. Commun. **124** (2000) 290 [arXiv:astro-ph/9903478].

[14] T. Stanev, R. Engel, A. Mucke, R. J. Protheroe and J. P. Rachen, Phys. Rev. D **62** (2000) 093005 [arXiv:astro-ph/0003484].

[15] E. Waxman and J. N. Bahcall, Phys. Rev. D **59** (1999) 023002 [arXiv:hep-ph/9807282].

[16] R. Engel, D. Seckel and T. Stanev, Phys. Rev. D **64** (2001) 093010 [arXiv:astro-ph/0101216].

[17] M. A. Malkan and F. W. Stecker, Astrophys. J. **555** (2001) 641 [arXiv:astro-ph/0009500].

[18] X. Bertou, P. Billoir, O. Deligny, C. Lachaud and A. Letessier-Selvon, Astropart. Phys. **17** (2002) 183 [arXiv:astro-ph/0104452].

[19] A. Letessier-Selvon, Nucl. Phys. Proc. Suppl. **91** (2001) 473 [arXiv:astro-ph/0009416].

[20] P. Gorham, D. Saltzberg, A. Odian, D. Williams, D. Besson, G. Frichter and S. Tantawi, Nucl. Instrum. Meth. A **490** (2002) 476 [arXiv:hep-ex/0108027].

[21] J. F. Beacom, N. F. Bell, D. Hooper, S. Pakvasa and T. J. Weiler, Phys. Rev. D **68** (2003) 093005 [Erratum-ibid. D **72** (2005) 019901] [arXiv:hep-ph/0307025].

[22] E. Fermi, Phys. Rev. 75, 1169̆20131174 (1949)

[23] B. J. Boyle and R. J. Terlevich, 1998MNRAS.293L..49B

[24] P. C. Hewett, C. B. Foltz, and F. H. Chaffee, 1993ApJ...406L..43H

[25] F. W. Stecker, Phys. Rev. Lett. **21**, 1016, (1968)

[26] C. D. Dermer and A. Atoyan, arXiv:astro-ph/0606629.

[27] F. W. Stecker and M. H. Salamon, Astrophys. J. **512**, 521 (1992) [arXiv:astro-ph/9808110].

[28] F. W. Stecker, Phys. Rev. **180**, 1264 (1969).

[29] M. A. Malkan and F. W. Stecker, Astrophys. J. **555**, 641 (2001) [arXiv:astro-ph/0009500].

[30] M. A. Malkan and F. W. Stecker, Astrophys. J. **496**, 13 (1998) [arXiv:astro-ph/9710072].

[31] F. Aharonian et al, 2003A&A...403..523A.

[32] F. A. Aharonian *et al.*, Astron. Astrophys. **349**, 11 (1999).

[33] D. Horns, F. A. Aharonian and L. Costamante [HEGRA Collaboration], New Astron. Rev. **48**, 387 (2004).

[34] A. Franceshini et al, 2001A&A...378....1F

[35] M. G. Hauser and E. Dwek, arXiv:astro-ph/0105539.

[36] M. G. Hauser et al, 1998ApJ...508...25H

[37] B. Altieri et al, 1999A&A...343L..65A

[38] P. Madau and L. Pozzetti, 2000MNRAS.312L...9M

[39] R. A. Bernstein, Astro. Soc. Pac.

[40] J. P. Gardner et al, 2000ApJ...542L..79G

[41] T. Stanev, arXiv:astro-ph/0607515.

[42] The nuclei-photon cross section data used is found at: http://www-astro.ulb.ac.be

[43] G. Sigl, F. Miniati and T. Ensslin, Nucl. Phys. Proc. Suppl. **136**, 224 (2004) [arXiv:astro-ph/0409098];
G. Sigl, F. Miniati and T. A. Ensslin, Phys. Rev. D **70**, 043007 (2004) [arXiv:astro-ph/0401084].

[44] E. Armengaud, G. Sigl and F. Miniati, Phys. Rev. D **72** (2005) 043009.

[45] K. Dolag, D. Grasso, V. Springel and I. Tkachev, JETP Lett. **79**, 583 (2004) [Pisma Zh. Eksp. Teor. Fiz. **79**, 719 (2004)] [arXiv:astro-ph/0310902].

[46] K. Dolag, D. Grasso, V. Springel and I. Tkachev, JCAP **0501** (2005) 009.

[47] M. A. Duvernois and M. R. Thayer, 1996ApJ...465..982D

[48] V. Berezinsky, A. Gazizov and S. Grigorieva, arXiv:astro-ph/0302483.

[49] M. Boettcher, arXiv:astro-ph/9901165.

[50] R. D. Preece, M. S. Briggs, R. S. Mallozzi, G. N. Pendleton, W. S. Paciesas and D. L. Band, arXiv:astro-ph/9808184.

[51] D. Guetta, D. Hooper, J. Alvarez-Muniz, F. Halzen and E. Reuveni, Astropart. Phys. **20** (2004) 429 [arXiv:astro-ph/0302524].

[52] E. Waxman and J. N. Bahcall, Phys. Rev. Lett. **78** (1997) 2292 [arXiv:astro-ph/9701231].

[53] J.A. Simpson *et al.*, 1983ICRC...10..322S.

[54] P.O. Lagage; C.J. Cesarsky, 1983A&A...125..249L

[55] A.M. Hillas, 1984ARA&A..22..425H

[56] D. C. Ellison and E. Moebius, 1987ApJ...318..474E

[57] D. C. Ellison, E. Moebius, and G. Paschmann, 1990ApJ...352..376E

[58] V. Berezinsky, A. Z. Gazizov and S. I. Grigorieva, Phys. Lett. B **612**, 147 (2005) [arXiv:astro-ph/0502550].

[59] D. Allard, E. Parizot, A. V. Olinto, E. Khan and S. Goriely, arXiv:astro-ph/0508465.

[60] T. Antoni *et al.* [The KASCADE Collaboration], Astropart. Phys. **24**, 1 (2005) [arXiv:astro-ph/0505413].

[61] C. J. Cesarsky, 1980ARA&A..18..289C

[62] S. Torii *et al.*, Astrophys. J. **559** (2001) 973.

[63] M. A. DuVernois *et al.*, Astrophys. J. **559** (2001) 296.

[64] A. Letessier-Selvon [Pierre Auger Collaboration], arXiv:astro-ph/0507331.

[65] K. H. Kampert *et al.* [The KASCADE Collaboration], Nucl. Phys. Proc. Suppl. **136**, 273 (2004) [arXiv:astro-ph/0410559].

[66] J. W. Cronin, T. K. Gaisser, and S. P. Swordy Sci. Amer. **276**, January 44 (1997)

[67] M. Nagano *et al.*, J. Phys. G **10** (1984) 1295.

[68] D. R. Bergman [The HiRes Collaboration], Nucl. Phys. Proc. Suppl. **136**, 40 (2004) [arXiv:astro-ph/0407244].

[69] V. A. Derbina *et al.*, 2005ApJ...628L..41D

[70] R. U. Abbasi *et al.* [The High Resolution Fly's Eye Collaboration], Astrophys. J. **622**, 910 (2005) [arXiv:astro-ph/0407622].

[71] D. J. Bird *et al.* [HIRES Collaboration], Phys. Rev. Lett. **71** (1993) 3401.

[72] S. P. Knurenko *et al.*, Nucl. Phys. Proc. Suppl. **151** (2006) 92 [arXiv:astro-ph/0411483].

[73] A. A. Watson, arXiv:astro-ph/0312475.

[74] S. Ostapchenko, arXiv:hep-ph/0501093.

[89] F. Aharonian *et al.* [HESS Collaboration], Astron. Astrophys. **449** (2006) 223 [arXiv:astro-ph/0511678].

[76] D. Berge, http://www.ub.uni-heidelberg.de/archiv/6156

[77] L. O. Drury, J. P. Meyer and D. C. Ellison, arXiv:astro-ph/9905008.

[78] E. Zas, F. Halzen and T. Stanev, Phys. Rev. D **45** (1992) 362.

[79] P. W. Gorham, K. M. Liewer, C. J. Naudet, D. P. Saltzberg and D. R. Williams, arXiv:astro-ph/0102435.

[80] F. Halzen and D. Hooper, Rept. Prog. Phys. **65** (2002) 1025 [arXiv:astro-ph/0204527].

[81] J. R. Hoerandel, arXiv:astro-ph/0611387.

[82] D. Band *et al.*, Astrophys. J. **413** (1993) 281.

[83] D. Giannios and H. C. Spruit, arXiv:astro-ph/0611385.

[84] T. R. Greve, P. P. Papadopoulos, Y. Gao and S. J. E. Radford, arXiv:astro-ph/0610378.

[85] M. A. Dopita, AIP Conf. Proc. **761** (2005) 203 [arXiv:astro-ph/0502339].

[86] L. A. Anchordoqui, J. F. Beacom, H. Goldberg, S. Palomares-Ruiz and T. J. Weiler, arXiv:astro-ph/0611581.

[87] L. A. Anchordoqui, G. E. Romero and J. A. Combi, Phys. Rev. D **60** (1999) 103001 [arXiv:astro-ph/9903145].

[88] T. A. Thompson, E. Quataert, E. Waxman, N. Murray and C. L. Martin, Astrophys. J. **645** (2006) 186 [arXiv:astro-ph/0601626].

[89] F. Aharonian *et al.* [HESS Collaboration], Astron. Astrophys. **449** (2006) 223 [arXiv:astro-ph/0511678].

[90] L. N. Epele, S. Mollerach and E. Roulet, arXiv:astro-ph/9812130.

[91] F. Halzen, arXiv:astro-ph/9810368.

[92] T. Stanev, arXiv:astro-ph/0611633.

[93] http://f64.nsstc.nasa.gov/batse/grb/lightcurve/

[94] T. Gaisser and A. M. Hillas, Proceedings of the 15th ICRC (Institute for Nuclear Research and Nuclear Energy, Sofia, Bulgaria, 1977), Vol. 8, pg. 353.

[95] P. Sommers *et al.* [Pierre Auger Collaboration], arXiv:astro-ph/0507150.

[96] A. Etchegoyen [Pierre Auger Collaboration], Astrophys. Space Sci. **290** (2004) 379.

[100] F. Halzen, arXiv:astro-ph/0602132.

[101] E. Waxman, Astrophys. J. **452** (1995) L1 [arXiv:astro-ph/9508037].

[102] W. Heitler, The Quantum Theory of Radiation, Oxford (1954)

"The Auger Observatory in Argentina," Astrophys. Space Sci. **290** (2004) 379.

[100] F. Halzen, arXiv:astro-ph/0602132.

[101] E. Waxman, Astrophys. J. **452** (1995) L1 [arXiv:astro-ph/9508037].

[102] W. Heitler, The Quantum Theory of Radiation, Oxford (1954)

[103] S.Inoue, arXiv:astro-ph/0701835